

REAL-TIME, SELECTIVE DETECTION OF HEAVY METAL
IONS IN WATER USING 2D NANOMATERIALS-BASED FIELD-
EFFECT TRANSISTORS

by

Guihua Zhou

A Dissertation Submitted in
Partial Fulfillment of the
Requirements for the Degree of

Doctor of Philosophy
in Engineering

at

The University of Wisconsin-Milwaukee

December 2017

ABSTRACT

REAL-TIME, SELECTIVE DETECTION OF HEAVY METAL IONS IN WATER USING 2D NANOMATERIALS-BASED FIELD-EFFECT TRANSISTORS

by

Guihua Zhou

The University of Wisconsin-Milwaukee, 2017
Under the Supervision of Professor Junhong Chen

Excessive intake of heavy metals damages the central nervous system and causes brain and blood disorders in mammals. Heavy metal contamination is commonly associated with exposure to mercury, lead, arsenic, and cadmium (arsenic is a metalloid, but classified as a heavy metal). Traditional methods to detect heavy metal ions include graphite furnace atomic absorption spectroscopy (GFAAS), inductively-coupled plasma optical emission spectroscopy (ICP-OES), and inductively-coupled plasma mass spectroscopy (ICP-MS). Recently, many new methods have been proposed to detect heavy metal ions, including atomic absorption spectrometry, fluorescent sensors, colorimetric sensors, electrochemical sensors, X-ray absorption fine structure spectroscopy, ultrasensitive dynamic light scattering assays, and ion selective electrodes. Although significant progress has been made, there are still some critical issues to be addressed, e.g., lack of portability, the need for well-trained personnel, highly expensive and complex instruments, long response time (tens of minutes or even longer), and the possibility of introducing additional contamination. Therefore, it is highly desirable to develop a real-time, low-cost, portable, user-friendly analytical platform for rapid inline analysis of mercury, lead and other heavy metal ions.

This dissertation research aims to investigate field-effect transistor (FET) sensors based on two-dimensional (2D) nanomaterials with specific probe-functionalized gold (Au) nanoparticles (NPs). The fundamental mechanism of the FET platform is to use a 2D nanomaterial as the conducting channel to transport charge carriers (electrons or holes). Upon the capture of target analytes, the charge carrier concentration and/or mobility changes correspondingly with a signal of current change within the channel. As a result, the FET characteristic changes upon the introduction of the heavy metal ion solution, varies with the metal concentration, and takes only a few seconds to respond. Control experiments are performed to verify the selectivity of the 2D nanomaterial/Au NP hybrid sensor to specific targets. The rapid, selective, sensitive, and stable detection performance indicates the promise of 2D nanomaterial/Au NP hybrid sensors for heavy metal ion detection in an aqueous solution.

This research is accomplished through several steps: First, various heavy metal ion contaminants, their damage, and the conventional detection methods are reviewed; Second, the FET-based platform and its working mechanism are explored; Third, the understanding of various 2D nanomaterials, their unique properties pertinent to electronic sensing, and their selection to realize real-time, selective, and sensitive detection of heavy metal ions is carried out; Finally, improvement of stability, sensitivity and lifetime of FET sensors is investigated.

In this thesis work, sensitive and selective FET-based 2D nanomaterial/Au NP hybrid sensors for Pb^{2+} , Hg^{2+} , As(III) , and As(V) have been demonstrated. The 2D nanomaterials include reduced graphene oxide (rGO), molybdenum disulfide (MoS_2), and black phosphorus (BP). The hybrid structure consists of a nanomaterial film, homogeneously dispersed Au NPs, and specific probes. The detection is enabled by recording the electrical conductance of the

device through monitoring the change in the drain current of the 2D nanomaterial sheets. The platform offers a promising route for real-time (1-2 seconds), high-performance and low-cost detection of heavy metal ions. The lower detection limit can reach the order of $\mu\text{g/L}$ (parts-per-billion or ppb). The sensor also shows high selectivity against other co-existing metal ions.

To improve the sensitivity of the nanomaterial-based electronic sensor, theoretical analysis on the sensing mechanism has been carried out, together with experimental validation. Theoretical analysis indicates that sensitivity-related factors are semiconducting properties of nanomaterials (e.g., carrier mobility, band gap), number of probes, and adsorption capacity of Au NPs. Experimental results suggest that a higher sensitivity for sensors can be realized by forming hybrid structures with thinner 2D conducting materials with a larger band gap and a higher carrier mobility, increasing the areal density of anchoring sites on the sensor surface, and enhancing the adsorption of detection probes. Investigation into the stability of the nanomaterial-based electronic sensor includes the binding strength between the nanomaterial and electrodes, stability of the nanomaterials in ambient environment and water, the detachment of Au NPs, the lifetime and diffusion of probes, and the overall stability of the sensor platform. Subsequently, strategies to improve the stability of the nanomaterial-based FET sensor have been proposed. Finally, the FET sensor has been used for the accurate prediction of arsenic ions in lake water and integrated into a practical flowing water system for continuous detection of lead ions.

The rapid, selective, sensitive, and stable detection performance of the FET sensor for various heavy metal ions in water suggests a promising future for in-situ detection of contamination events. The thesis study provides a scientific foundation to engineer FET sensors

with enhanced performance. An attempt has been made to practically develop the FET platform into standalone sensors and to integrate the sensor into flowing water equipment for heavy metal ion detection. The thesis results thus contribute to the future application of FET sensors for monitoring water contamination and mitigating the public health risk.

©Copyright by Guihua Zhou, 2017
All Rights Reserved

To
my family,
my fiancé,
and especially my mom

TABLE OF CONTENTS

ABSTRACT.....	II
LIST OF FIGURES	X
LIST OF TABLES	XVII
LIST OF ABBREVIATIONS	XVIII
ACKNOWLEDGEMENTS	XXII
CHAPTER 1 INTRODUCTION AND LITERATURE SURVEY *	1
1.1 Heavy metal ion contamination and its damage.....	1
1.2 Conventional methods to detect heavy metals in water.....	5
1.3 Nanomaterial-based sensors for the detection of heavy metal ions in water.....	7
1.4 Objectives and outline of the dissertation research.....	19
CHAPTER 2 REAL-TIME, SELECTIVE DETECTION OF Pb^{2+} IN WATER USING A REDUCED GRAPHENE OXIDE/GOLD NANOPARTICLE FIELD-EFFECT TRANSISTOR*	21
2.1 Introduction.....	21
2.2 Experimental methods.....	22
2.3 Results and discussion	27
2.4 Summary and conclusion	35
CHAPTER 3 ULTRASENSITIVE MERCURY ION DETECTION USING DNA-FUNCTIONALIZED MOLYBDENUM DISULFIDE NANOSHEET/GOLD NANOPARTICLE HYBRID FIELD-EFFECT TRANSISTOR *	36
3.1 Introduction.....	36
3.2 Experimental methods.....	37
3.3 Results and discussion	40
3.4 Summary and conclusion	52
CHAPTER 4 REAL-TIME AND SENSITIVE ARSENIC ION DETECTION USING BLACK PHOSPHORUS/AU NP/DTT HYBRID STRUCTURE *	54
4.1 Introduction.....	54
4.2 Experimental methods.....	54
4.3 Results and discussion	56
4.4 Arsenic analysis in lake water samples	64
4.5 Summary and conclusion	67

CHAPTER 5 SENSITIVITY IMPROVEMENT OF THE FET SENSOR BASED ON 2D NANOMATERIALS.....	68
5.1 Introduction.....	68
5.2 Sensing mechanism analysis	69
5.3 Channel material investigation.....	75
5.4 Effect of Au NP density	79
5.5 Effect of probe coverage.....	83
5.6 Summary and conclusion	85
CHAPTER 6 STABILITY STUDY OF THE FET SENSOR BASED ON 2D NANOMATERIALS.....	87
6.1 Introduction.....	87
6.2 Channel material stability investigation	87
6.3 Anchoring sites -Au NPs stability investigation	93
6.4 Probe stability investigation.....	94
6.5 Flowing water test	99
6.6 Summary and conclusion	104
CHAPTER 7 CONCLUSIONS AND OUTLOOK	106
7.1 Conclusions.....	106
7.2 Outlook	109
REFERENCES.....	113
CURRICULUM VITAE.....	126

LIST OF FIGURES

Figure 1.1 The schematic of the FET platform.....	10
Figure 1.2 (a) The hexagonal structure model of graphene; (b) the oxygen functional groups on graphene sheet.	12
Figure 1.3 (a) Atomic structure of monolayer MoS ₂ of 6.5 Å thick. ¹ (b) Atomic structure of black phosphorus of 5 Å thick.	15
Figure 1.4 Bandgap energies of several layered materials used for nanoelectronics. The range of values for each material can be achieved through a variety of means. For example, it is expected that variations in an applied perpendicular electric field, film thickness or strain could modify the bandgap value. hBN, hexagonal boron nitride.....	16
Figure 2.1 Schematic diagram of the rGO/GSH-Au NP hybrid sensor fabrication process: (a) a layer of AET coating on the bare interdigitated electrode surface, (b) self-assembly of GO monolayer sheets on the AET-modified electrodes, which is followed by the thermal reduction of GO to rGO, (c) the assembly of Au NPs onto the rGO film, (d) GSH-modification of Au NPs on the rGO sheet surface to form specific recognition groups to detect Pb ²⁺ ion.....	23
Figure 2.2 (a and b) SEM images of rGO sheets spanning across the interdigitated electrodes, showing transparency to the electron beam, (c) SEM image of the rGO sheet decorated with Au NPs of 2 nm thick, (d and e) AFM (tapping mode) height image and profile of rGO with the dashed line indicating the scanning trace, (f) Raman spectrum of the rGO.....	25
Figure 2.3 (a) I _{ds} -V _{gs} (V _{ds} =5 V, V _{gs} = -40 V~40 V, step = 0.2 V) (b) I _{ds} -V _{ds} (V _{ds} = -2.1 V~2.1 V, step = 0.1 V) characteristics of an rGO/GSH-Au NP hybrid sensor exposed to water (black)	

and 10 μM Pb^{2+} solution (red) and (c) real-time detection ($V_{\text{ds}} = 0.1 \text{ V}$) of Pb^{2+} in water with the rGO/GSH-Au NP hybrid sensor. Lower detection limit: 10 nM (0.002 mg/L).....29

Figure 2.4 (a) $I_{\text{ds}}-V_{\text{gs}}$ ($V_{\text{ds}} = 5 \text{ V}$, $V_{\text{gs}} = -40 \text{ V} \sim 40 \text{ V}$, step = 0.2 V) (b) $I_{\text{ds}}-V_{\text{ds}}$ ($V_{\text{ds}} = -2.1 \text{ V} \sim 2.1 \text{ V}$, step = 0.1 V) characteristics of various devices, (c) I_{ds} versus time ($V_{\text{ds}} = 0.1 \text{ V}$) (dynamic responses) of rGO-based sensing platforms: rGO (black), rGO/Au (red), rGO/GSH-Au NP (blue), and (d) the sensitivity trendline of the rGO/GSH-Au NP hybrid sensor to Pb ions ranging from 10 nM to 10 μM : $y = 1.5534\ln(x) - 1.8727$, $R^2 = 0.9985$30

Figure 2.5 Dynamic responses ($V_{\text{ds}} = 0.36 \text{ mV}$) of the rGO/GSH-Au NP hybrid sensor to common metal ions: Na^+ , Ca^{2+} , Fe^{3+}32

Figure 2.6 (a) Dynamic responses ($V_{\text{ds}} = 0.1 \text{ V}$) to varying concentrations of heavy metal ions and (b) relative current change of an rGO/GSH-Au NP hybrid sensor in response to various heavy metal ions: Ag^+ , As(V) , Cd^{2+} , Cu^{2+} , Hg^{2+} , Pb^{2+} , Zn^{2+} , and a mixed solution of the six ions (10 μM for total).....33

Figure 3.1 MoS_2 membrane preparation and transfer process. (a-b), MoS_2 film was prepared by filtering a diluted MoS_2 suspension through a mixed cellulose ester membrane with 25 nm pores. (c-d), the MoS_2 film was delaminated and transferred onto the Si/SiO₂ substrate.....39

Figure 3.2 (a) Schematic diagram for the fabrication process of the $\text{MoS}_2/\text{DNA-Au}$ NPs hybrid structure. (b) The FET sensor platform based on the hybrid structure. The formation of T-(Hg^{2+})-T chelates, through reactions between Hg^{2+} and the thymidine of the DNA molecules on the Au NPs, leading to the change in the MoS_2 electrical conductivity as a sensor signal...40

Figure 3.3 (a) TEM, (b) high resolution TEM (HRTEM), (c) AFM images, and (d) cross-sectional height profile of the exfoliated MoS_2 nanosheets, (e) RR spectrum of the

exfoliated/thermally treated MoS₂ nanosheets, (f) SEM image of the prepared 2H-MoS₂ film.

Insert: SEM image of the prepared MoS₂ film decorated with Au NPs..... 42

Figure 3.4 (a) $I_{ds}-V_{gs}$ ($V_{ds}= -40\text{ V}\sim 40\text{ V}$, step = 0.5 V) characteristics of the MoS₂/DNA-Au NPs hybrid sensor, in air at room temperature, immediately after the thermal annealing without exposure to much oxygen. (b) Room-temperature transfer characteristics of the FET sensor in air with the bias voltage V_{ds} . of 0.1 V ($V_{gs}= -40\text{ V}\sim 40\text{ V}$, step = 0.5 V). Here, the sensor had been exposed to air for over 12 hours before the FET measurement. Inset: $I_{ds}-V_{ds}$ curve acquired for a V_{gs} value of 0 V.....43

Figure 3.5 Schematics of band alignment between the MoS₂ film and the Au electrode before and after contact.....44

Figure 3.6 (a) Evolution of the $I_{ds}-V_{ds}$ characteristics during the MoS₂/DNA-Au NPs hybrid sensor fabrication process ($V_{ds}= -2.1\text{ V}\sim 2.1\text{ V}$, step = 0.1 V) at room temperature. (b) Real-time detections of Hg²⁺ (nM) in water ($V_{ds}= 0.1\text{ V}$) with platforms of MoS₂/DNA-Au NPs (black, solid), MoS₂-Au NPs (purple, dash), MoS₂ (blue, short dash), respectively.....45

Figure 3.7 Real-time detection ($V_{ds}= 0.1\text{ V}$) of Hg²⁺ in water, with concentrations ranging from 100 pM to 10 μM, using blank Au electrode.48

Figure 3.8 (a) Real-time detection of Hg²⁺ in water using the MoS₂/DNA-Au NPs hybrid sensor ($V_{ds}= 0.1\text{ V}$) with a lower detection limit of 0.1 nM (0.02 μg/L). (b) Sensitivity variation and exponential fitting of sensitivity using Eq. (3.1) as a function of Hg²⁺ concentration for the MoS₂/DNA-Au NPs hybrid sensor. (c) Real-time detection of various interfering ions in water with the MoS₂/DNA-Au NPs hybrid sensor. ($V_{ds}= 0.1\text{ V}$) (d) Relative current change of an

MoS₂/DNA-Au NP hybrid sensor in response to various heavy metal ions: As(V), Ca²⁺, Cd²⁺, Cu²⁺, Fe³⁺, Hg²⁺, Mg²⁺, Na⁺, Pb²⁺ and Zn²⁺ (1 nM).....49

Figure 3.9 Repeatability of the MoS₂/DNA-Au NPs hybrid sensor, confirmed by similar dynamic responses of three different sensors to Hg²⁺, with concentrations ranging from 1 pM to 100 nM.....51

Figure 3.10 Real-time detection ($V_{ds} = 0.1$ V) of Hg²⁺ in real water samples (provided by our industrial partner) with concentrations ranging from 0.5 nM to 250 nM using the MoS₂/DNA-Au NPs hybrid sensor.....51

Figure 3.11 Reusability of the MoS₂/DNA-Au NPs hybrid sensor, suggesting no significant degradation in the sensitivity was observed in dynamic responses of the same sensor to Hg²⁺ for three continuous uses after washing.....52

Figure 4.1 (a) Mechanical exfoliation of the BP film using the “Scotch tape” method. (b) The exfoliated BP film was transferred onto the Au electrodes.....55

Figure 4.2 Schematic of the BP/Au NPs/DTT sensing platform for the As ion detection. (b) The reaction between the DTT and As (III) ion in the detection process.....57

Figure 4.3 SEM images of (a) bulk BP with the layered structure, (b) an exfoliated BP flake electrically bridging the interdigitated Au electrodes. (c) AFM image of exfoliated BP flakes and, inset: the height profile across the flakes. (d) HRTEM image of a BP film, demonstrating the typical BP lattice spacing. (e) TEM image and (f) SAED pattern of the BP film.....58

Figure 4.4 Electronic characteristics and real-time sensing performance of the FET sensor platform (a) I_{ds} - V_{gs} curve with the bias voltage V_{gs} ranging from -40 to 40 V ($V_{ds} = 0.1$ V). (b) I_{ds} - V_{ds} curve with the $V_{ds} = -1V \sim 1V$ ($V_{gs} = 0$ V). (c) Real-time detection of As (III) in water

($V_{ds} = 0.1 \text{ V}$, $V_{gs} = 0 \text{ V}$) with the BP/Au NPs/DTT platform, for concentrations ranging from 1 nM to 1 μM59

Figure 4.5 (a) Real-time detection of neutral (pH= 7) As (III) solutions in water ($V_{ds} = 0.1 \text{ V}$, $V_{gs} = 0 \text{ V}$) with the BP/Au NPs/DTT platform, for concentrations ranging from 1 nM to 1 μM . (b) Real-time detection of As (V) in water ($V_{ds} = 0.1 \text{ V}$, $V_{gs} = 0 \text{ V}$) with the BP/Au NPs/DTT platform, for concentrations ranging from 0.1 nM to 1 μM . Insert: the schematic of DTT reducing As (V) to As (III).....62

Figure 4.6 (a) I_{ds} - V_{gs} curve with the gate voltage V_{gs} ranging from -10 V to 10 V. (b) I_{ds} - V_{ds} curve with the $V_{ds} = -1 \text{ V} \sim 1 \text{ V}$. (c) The I_{ds} vs. time ($V_{ds} = 0.1 \text{ V}$) (dynamic responses) of BP FET-based sensing platforms: the prepared BP film (black), BP/Au NPs (blue), BP/Au NPs/ DTT (red) in air.....64

Figure 4.7 Sensitivity to As in water and (a) the logarithmic fitting curve, (b) the linear fitting curve of sensitivity as a function of As concentration for the BP/Au NPs/DTT hybrid sensor.....65

Figure 4.8 Selectivity: real-time detection of As as well as other ions (10 nM), including Ag^+ , Ca^{2+} , Cd^{2+} , Cu^{2+} , Fe^{3+} , Hg^{2+} , Mg^{2+} , Na^+ , Pb^{2+} , Zn^{2+} (a) in initial states (b) with 1:1 molar ratio of EDTA added, phosphate ions (H_2PO_4^-), and humic acid in water with the BP/Au NPs/DTT hybrid sensor ($V_{ds} = 0.1 \text{ V}$, $V_{gs} = 0 \text{ V}$).....66

Figure 4.9 The I_{ds} change introduced by EDTA (100 nM) to the BP/Au NPs/DTT platform ($V_{ds} = 0.1 \text{ V}$, $V_{gs} = 0 \text{ V}$).....67

Figure 5.1 (a) Schematic of the FET sensing platform and (b) its equivalent Randles circuit...70

Figure 5.2 Channel resistance change mechanism after introducing Pb^{2+} ions to rGO/AuNPs/GSH platform: (a) Charge transfer vs. (b) Gating effect.....72

Figure 5.3 Schematic of introducing gating effect to the channel and the contact region: electrons are directly induced in the channel region, but positive voltage is applied to the contact regions.....72

Figure 5.4 EIS spectra of the Randles circuit for the response of the rGO/Au NPs/GSH platform to Pb^{2+} ions of various concentrations73

Figure 5.5 (a-b) SEM and (c-d) TEM images of rGO/ Al_2O_3 structure indicate the good uniformity of Al_2O_3 film coated on the surface of rGO75

Figure 5.6 (a) Schematic of the rGO/ Al_2O_3 /Au NPs/GSH platform and (b) its sensing performance of before and after applying Al_2O_3 passivation layer.....76

Figure 5.7 Sensitivity as a function of Hg^{2+} concentration for the MoS_2 /DNA-Au NPs hybrid sensor with different MoS_2 film thicknesses.....78

Figure 5.8 Real-time detection ($V_{ds}= 0.1$ V) of Hg^{2+} in water, with concentrations ranging from 100 pM to 10 μ M, using the rGO/DNA-Au NPs hybrid sensor. The rGO/DNA-Au NPs hybrid structure sensor was prepared with a similar method used in our previous study.....79

Figure 5.9 The morphology of Au NPs under different sputtering parameter settings.....82

Figure 5.10 Prepared 1.5cm *1.5 cm silicon wafers submersed in saturated 1 mL GSH solution (50uM).....83

Figure 5.11 Correlation between (a) Au NPs size, (b) particle number and (c) areal density to GSH adsorption.....83

Figure 5.12 Dynamics and kinetics of thiol coating on Au: from approaching to adsorption...84

Figure 6.1 Schematic of the BP/Al ₂ O ₃ /Au NPs/DTT platform.....	91
Figure 6.2 SEM images of the Au electrodes with (a) newly prepared rGO flake bridging the electrodes and (b) the same rGO flake stored in DI water for one month	93
Figure 6.3 The stability of rGO/Au NP-GSH sensor stored in water.	94
Figure 6.4 SEM images of the sensing surface with sputter-coated Au NPs stored in water for various times as labeled	95
Figure 6.5 The plot of GSH detached from the Au NPs in ultrapure water.	97
Figure 6.6 The calibration curve for GSH concentration and the interpolation calculation....	99
Figure 6.7 (a) The flowing water system, (b) the 3 ports valve that controls the switch between metal ions and DI water, and (c) the sensor imbedded test-cell is integrated in the flowing tube. Insert: the sensor chip. (d) The bypass system.....	101
Figure 6.8 The dynamic sensing performance of the rGO/Al ₂ O ₃ /Au NPs/GSH sensor to Pb ²⁺ ions of various concentrations 200 ppb, 400 ppb, 2 ppm and DI water in the flow system.....	102
Figure 6.9 Schematic of Pb ²⁺ ion adsorption (a) in the static water, and (b) in the flowing water system.....	103

LIST OF TABLES

Table 1.1 Types of heavy metal and their effect on human health with their permissible limits.....	1
Table 1.2 2D nanomaterial-based FET sensors and their application in aqueous sensing.....	17
Table 2.1 The lower detection limit achieved by different methods measuring lead ions in water.....	34
Table 3.1 Comparison of LOD and calibrated range among different methods for Hg ²⁺ detection	46
Table 4.1 Comparison of arsenic ion detection with different methods.....	62
Table 4.2 Real water sample test with the BP/Au NPs/DTT sensor.....	68
Table 5.1 EIS analysis result for the response of the rGO/Au NPs/GSH platform to Pb ²⁺ ions.....	74
Table 5.2 Parameter settings for the Au NP sputtering.....	82
Table 5.3 Au NPs - GSH coverage ratio tested by ICP-MS.....	86
Table 6.1 rGO resistance change in different ambient environments.....	90
Table 6.2 Resistance tracking of MoS ₂ based sensors stored in argon.....	91
Table 6.3 Resistance tracking of BP based sensors stored in argon.....	92

LIST OF ABBREVIATIONS

ΔC_{ch}	channel capacitance change
$\Delta C_{\text{contact}}$	contact capacitance change
ΔG	conductance change
ΔR_{ch}	channel material change
$\Delta R_{\text{contact}}$	contact resistance change
1D	one-dimensional
2D	two-dimensional
AAS	atomic absorption spectroscopy
AET	cysteamine
AFM	atomic force microscopy
ALD	atomic layer deposition
As	arsenic
As(III), AsO_3^{3-}	arsenite
As(V), AsO_4^{3-}	arsenate
ASV	anodic stripping voltammetry
Au	gold
BP	black phosphorus
Cd	cadmium
Cu	copper
Cr	chromium
CVD	chemical vapor deposition

CNT	carbon nanotube
DFT	density functional theory
DI	deionized
DPASV	differential pulse anodic stripping voltammetry
DTT	dithiothreitol
EDTA	ethylenediaminetetraacetic acid
EDX	energy dispersive X-ray analysis
EIS	electrochemical impedance spectroscopy
ELISA	enzyme-linked immunosorbent assay
EPA	environmental protection agency
FET	field-effect transistor
FRET	fluorescence resonance energy transfer
FTIR	Fourier-transform infrared spectroscopy
G_0	initial conductance
GFAAS	graphite furnace atomic absorption spectroscopy
GO	graphene oxide
GSH	l-glutathione
hBN	hexagonal boron nitride
Hg	mercury
HPLC	high performance liquid chromatography
HRTEM	high-resolution transmission electron microscopy
ICP-OES	inductively coupled plasma optical emission spectroscopy

ICP-MS	inductively coupled plasma mass spectroscopy
IDT	integrated DNA technologies
IUPAC	international union of pure and applied chemistry
LOD	limit of detection
LSV	linear sweep voltammetry
M	mol/L
MCL	maximum contaminant level
MOs	molecular orbitals
MoS ₂	molybdenum disulfide
NAA-RFs	nanoporous anodic alumina rugate filters
Ni	nickle
NPs	nanoparticles
NSET	nanometal surface energy transfer
Pb	lead
PBS	phosphate buffer solution
ppb	parts-per-billion
ppq	parts-per-quadrillion
PVD	physical vapor deposition
QDs	quantum dots
R ₀	system resistance
RfS	reflection spectroscopy
rGO	reduced graphene oxide

RR	resonance Raman
SAED	selected area electron diffraction
SAM	self-assembly monolayer
SEM	scanning electron microscopy
SPR	surface plasmon resonance
SWASV	square wave anodic stripping voltammetry
TBC	thermal boundary conductance
TEM	transmission electron microscopy
TMD	transition metal dichalcogenides
V_{ds}	source–drain voltage
WHO	world health organization
Zn	zinc

ACKNOWLEDGEMENTS

First, I would like to thank my supervisor, Prof. Junhong Chen, for his insightful and patient guidance during my Ph.D. study. He gives me huge support not only in my research, but also in my life. I also thank my family, my fiancé and all the members in my lab who gave me support during my Ph.D. program. Particularly, I am very grateful to Dr. Jingbo Chang for providing me with the sensor electrodes and to Dr. Haihui Pu for laying down the theoretical framework that helped me better understand the sensing platform.

Also, I thank Dr. Heather A. Owen for technical support with SEM analyses at the University of Wisconsin-Milwaukee (UWM) Electron Microscope Laboratory, Dr. Steven E. Hardcastle for technical support with XRD, XPS, and Raman analyses, Mr. Patrick Anderson for the technical support in the operation of ICP-MS at UWM School of Freshwater Sciences.

Financially, this work was supported by the U.S. National Science Foundation through the NSF Industry/University Cooperative Research Center on Water Equipment & Policy led by the University of Wisconsin-Milwaukee and Marquette University (IIP-0968887), NSF fundamental research grant (IIP-1128158), NSF Partnership for Innovation (PFI) grant (IIP-1434059) and the UWM Water Accelerator grant. The SEM imaging and EDS were conducted at the Electron Microscope Laboratory of UWM. TEM analyses were conducted in the UWM HRTEM Laboratory. XRD and RAMAN analyses were conducted in the Advanced Analysis Facility (AAF) of UWM. The e-beam lithography and sensor electrode fabrication were performed by Dr. Jingbo Chang at the Global Water Center, Milwaukee and the Center for Nanoscale Materials of Argonne National Laboratory, which is supported by the U.S. Department of Energy, Office of Science, Office of Basic Energy Sciences, under Contract no.

DE-AC02-06CH11357. ICP-MS test was conducted at the School of Freshwater Science of UWM.

CHAPTER 1 INTRODUCTION AND LITERATURE SURVEY *1

1.1 Heavy metal ion contamination and its damage

There is no clear definition of heavy metal that is globally accepted; however, in most cases, density is the defining factor for heavy metals. A metal with a density larger than 5 g/cm³ is classified as a heavy metal.² These metals can cause environmental pollution and generate threats to human health. The types of heavy metals, their effect on human health, and their permissible limits (defined by Environmental Protection Agency, EPA) are summarized in Table 1.1.³⁻⁴

Table 1.1 Types of heavy metals and their effect on human health with their permissible limits.

Pollutants	Major Sources	Effect on human health	Permissible level (mg/L)
Arsenic	Pesticides, fungicides, metal smelters	Bronchitis, dermatitis, poisoning	0.01
Lead	Paint, pesticide, smoking, automobile emission, mining, burning of coal	Mental retardation in children, development delay, fatal infant encephalopathy, congenital paralysis, sensor neural deafness and, acute or chronic damage to the nervous system, epilepticus, liver, kidney, gastrointestinal damage	0.015

*1 Part of this chapter has been published.

Cadmium	Welding, electroplating, pesticide fertilizer, Cd and Ni batteries, nuclear fission plant	Renal dysfunction, Lung disease, Lung cancer, Bone defects (Osteomalacia, Osteoporosis), increased blood pressure, kidney damage, bronchitis, gastrointestinal disorder, bone marrow, cancer	0.005
Manganese	Welding, fuel addition, ferromanganese production	Inhalation or contact causes damage to central nervous system	0.05
Mercury	Pesticides, batteries, paper industries	Tremors, gingivitis, minor psychological changes, acrodynia characterized by pink hands and feet, spontaneous abortion, damage to nervous system, protoplasm Poisoning	0.002
Zinc	Refineries, brass manufacture, metal Plating, plumbing	Zinc fumes have corrosive effect on skin, cause damage to nervous membrane	5
Chromium	Mines, mineral sources	Damage to the nervous system, fatigue, irritability	0.1
Copper	Mining, pesticide production, chemical industry, metal piping	Anemia, liver and kidney damage, stomach and intestinal irritation	1.3

Heavy metal contamination is mainly associated with exposure to mercury (Hg), lead (Pb), arsenic (As), cadmium (Cd), copper (Cu), chromium (Cr), nickel (Ni) and zinc (Zn) (arsenic is a metalloid, but classified to be a heavy metal),⁵ which pose severe risks to human health. It is widely known that mercury is highly toxic: it can cause fatal illnesses, such as cyanosis syndrome, minamata disease, nephrotic syndrome and pulmonary edema, due to the

accumulation in the body.⁶ It can damage the nervous and gastrointestinal systems and even result in kidney and respiratory failure.⁷ Many regulations have been developed to control the use of Hg ions. However, it is still widely used in many domestic and industrial applications, for example, pesticides, architecture, cosmetics, thermometers, mining and power plants, etc. As a result, they will lead to the high temperature coal combustion, chlorine alkali processing for the power plant, waste incineration of the mercury related products. Besides these human-related mercury sources, another source is natural source, including natural mercury deposits, leaking from volcanoes eruption and volatilization from the ocean.⁸ All these mercury sources will introduce the mercury to the atmosphere and/or water sources. Once the water is contaminated, the fish will also be polluted. Therefore, the life safety of human, especially for young children, infants and fetus, will be challenged either through drinking the contaminated water or eating the polluted fishes.

Besides mercury, lead is another widely known heavy metal that poses significant threats to human health. Recently, there have been numerous reports on lead causing water contamination, which leaches from water piping systems to drinking water and tap water.⁹⁻¹⁰ The most frequently reported lead contamination is the lead ions' pollution from the lead soldered brass or chrome-plated brass faucets and fixtures, since the lead contained pipes or fixtures will be corroded by water that has high acidity or low mineral content. Afterwards, significant amounts of lead can enter into the water, especially hot water.¹¹ And lead pipes, fixtures and solder are more likely to exist in homes built before 1986. Lead contamination has become a health threat, especially for young children and infants. Lead poisoning had been recorded throughout history, since ancient China, ancient Rome, and ancient Greece. Excessive

lead damages the central nervous system and causes brain and blood disorders in mammals.¹² Lead has the ability to form complexes with ligands of biological matters that contain nitrogen, sulfur, and oxygen, because of the covalent interaction between filled ligand orbitals (e.g., O 2p) and the Pb^{2+} 6s, therefore, empty 6p orbitals can create bonding and antibonding molecular orbitals (MOs).¹³ Further, the complex leads to changes in the molecular structure of proteins, breaking of hydrogen bonds, and inhibition of enzymes.

Arsenic, the 20th most abundant mineral in the earth's crust and 12th most common mineral in the human body, is widely distributed in nature in various states. Generally, it exists in organic and/or inorganic -3, +3 and +5 oxidation states.¹⁴ The most common arsenic species in water include arsenate (As(V), AsO_4^{3-}) and arsenite (As(III), AsO_3^{3-}). Under oxidizing conditions, arsenate is the dominating form and its protonation state is a strong function of pH. At neutral pH, $H_2AsO_4^-$ and $HAsO_4^{2-}$ co-exist. The toxicity of As is notorious; the ancient history of China recorded the toxicity of trioxide arsenic (they call it 'Pishuang'), and inorganic arsenic species are more toxic than organic ones.¹⁵ The sources of Arsenic contamination include agriculture, mining and natural release. The direct application of arsenic in the form of pesticides or wood preservatives has historically been a major source of arsenic to soils.¹⁶ Besides agriculture, in the mining process, arsenic runoff from contaminated sites and would impact the freshwaters and associated ecosystems. Furthermore, the natural release of arsenic from geologic materials will flow into ground water, which has become a threat to drinking water supplies around the world.¹⁷ Drinking water with arsenic will cause various diseases, including hyperkeratosis on the palm or feet, fatigue, cancer of the bladder, and genotoxic and mutagenic effects.¹⁸ This is because proteins with sulfur-containing groups can react with

As(III) to form products that will cause biological body malfunction.¹⁹ To manage the arsenic poisoning problem, detection is crucial.

1.2 Conventional methods to detect heavy metals in water

Water plays an important role in the world economy: it functions as a key element of food and energy production, as a solvent for a wide variety of chemical substances, and facilitates industrial cooling, transportation, and effluent discharge. Heavy metals, e.g., lead, cadmium, mercury, and semi-metals, e.g., arsenic, are widely present in water systems.²⁰ Traditional methods to detect heavy metal ions in water include atomic absorption spectroscopy (AAS)²¹ that uses the absorption of optical radiation (light) by free atoms in the gaseous state for the quantitative determination of chemical elements. AAS can be used to determine over 70 different elements in a solution or directly in solid samples used in pharmacology, biophysics and toxicology research. Another traditional method is inductively coupled plasma mass spectrometry (ICP-MS), in which the sample is ionized with inductively coupled plasma and then a mass spectrometer is used to separate and quantify those ions. ICP-MS is capable of detecting metals and several non-metals at concentrations as low as one part in 10^{15} (parts per quadrillion, ppq).²² Recently, other sensors have also been developed to detect mercury ions to protect human beings from drinking or eating mercury ions. These methods are colorimetric analysis,²³⁻²⁵ electrochemical methods,²⁶⁻²⁹ fluorescence spectroscopy,³⁰ X-ray absorption fine structure spectroscopy³¹ and ultrasensitive dynamic light scattering assays.³²

Colorimetric sensors have been extensively studied for heavy metal sensing.³³⁻³⁴ Sener et al. developed a robust, gold nanoparticles (Au NPs)-based colorimetric sensor array that was

capable of discriminating seven metal ions (Hg^{2+} , Cd^{2+} , Fe^{3+} , Pb^{2+} , Al^{3+} , Cu^{2+} , and Cr^{3+}) simultaneously with excellent selectivity.³⁵ Such colorimetric assay was based on metal ion induced aggregation of Au NPs in the presence of different chemicals, resulting in different chelate formation capability of metal ions. Fluorescence detection of heavy metal ions is another important method for monitoring water quality.³⁶⁻³⁷ In this type of sensor, artificial receptors that exhibit changes in their fluorescence properties upon binding to heavy metal ions are recognized as powerful detection tools due to their high sensitivity and selectivity. In particular, quantum dots (QDs)³⁸ can generate narrow, size-tunable, and symmetric emission spectra, which makes them excellent donors for fluorescence resonance energy transfer (FRET) or nanometal surface energy transfer (NSET) sensor³⁸ and offers significant advantages over organic dyes as optical labels for chemo/biosensing.³⁹⁻⁴⁰ Electrochemical method (e.g., anodic stripping voltammetry, ASV) is a promising and elegant technique for detecting trace levels of toxic heavy metal ions due to its high sensitivity, selectivity, and short detection time, and it can detect multiple heavy metals simultaneously.⁴¹⁻⁴² It usually consists of three steps for heavy metal ion detection: cleaning step, metal deposition step, and detection step (stripping/oxidizing the metal). Compared with the linear sweep voltammetry (LSV) technique, the ASV technique with linear scans or modulations (differential pulse ASV/DPASV and square wave ASV/SWASV) has higher sensitivity.⁴²

Although significant progress has been made with these methods, there are still some critical issues to be addressed, for example, lack of portability, the need for well-trained personnel, highly expensive and complex instruments, long response time (tens of minutes, or even longer), and the possibility of introducing additional contamination. Accordingly,

exploring sensitive, rapid real-time, low-cost, portable, user-friendly, analytical methods for precise monitoring of metal ions in drinking water is urgently needed.

1.3 Nanomaterial-based sensors for the detection of heavy metal ions in water

Nanomaterials have been widely studied in optical, electronic and electrochemical sensors for detection of water contaminants due to their unique structures and excellent optical/electrical/catalytic properties. The nanomaterial-based sensors show great promise in water contaminant detection, and their performance outperforms the conventional sensors/technologies in various aspects, e.g., high sensitivity, fast response, and simple operation.

Optical sensor. It is well known that the optical response of spherical Au NPs exhibits a single absorption band attributed to the collective dipole oscillation (surface plasma resonance).⁴³ Au NPs were used as the typical agent in this type of sensors due to their tunable optical and electronic properties that are controlled by the surface-plasmon resonance through size control of NPs and their aggregation state in the solution. For example, smaller individual NPs appear ruby red while larger particles or aggregates of smaller particles have a purple to deep blue color. For sensor operation, once a specific analyte is introduced, uncontrolled aggregation will start due to binding and subsequently leads to change in the solution color, which is either due to small changes in refractive index of the surrounding medium or the changes in inter-NP interactions during binding of targeted analytes. Fluorescent sensors based on 2D nanomaterials, e.g., graphene nanosheets, have received increasing attention for the detection of heavy metal ions in recent years. The excellent biocompatibility, chemical

inertness and lower cytotoxicity of graphene nanosheets suggest them as a promising candidate for the detection of metal ions. For example, the use of graphene oxide (GO) for charge transfer-based fluorescent sensor was reported by Wu et al.⁴⁴

Electrochemical sensor. In addition to optical sensors, nanomaterial-based electrochemical sensors were also used for rapid detection of heavy metal ions. This type of sensor utilizes the electrocatalytic activity of the working electrode in a redox system for analyte detection (oxidation peak location for selectivity and reaction current for sensitivity). The performance of electrochemical sensors depends on the electrode materials. Due to their small size, large accessible surface area, and high catalytic activity, nanomaterials were intensively studied as electrode materials in electrochemical sensors. Among all methods for heavy metal ion detection, the electrochemical method (e.g., ASV) is a promising and elegant technique for detecting trace levels of toxic heavy metal ions due to its high sensitivity, selectivity, and short detection time, and it can detect multiple heavy metals simultaneously.⁴⁵ With nanoparticles, nanofibers, carbon nanotubes (CNTs), graphene, titanate nanosheets, and nanocomposites, non-toxic electrodes have been widely studied in heavy metal ion detection. The nanomaterial-based electrodes have a high efficiency in pre-concentration and deposition of metal ions and show high catalytic activity in stripping tests. Due to their high conductivity and large specific surface area, graphene and graphene-based composites have been used in electrochemical systems for heavy metal ion detection. Combining the high adsorption capacity of γ -AlOOH with the high conductivity of graphene, an electrochemical platform for the simultaneous detection of Cd^{2+} and Pb^{2+} ions was reported using the SWASV technique.⁴⁶

Electronic sensor. Besides the application in electrochemical methods, nanomaterials have also brought great opportunities in water contaminant detection owing to their unique electronic properties. In the past decade, various electronic sensors, e.g., field-effect transistor (FET) sensors, have been developed based on nanowires, carbon nanotubes, graphene, and MoS₂ nanosheets. Due to their high carrier mobility and high sensitivity to electronic perturbations, nanomaterial-based FET sensors usually show a high sensitivity and a rapid response to water contaminants. These unique features allow for the rapid detection of water contaminants to address limitations of conventional sensing technologies. FET sensors detect the presence of water contaminants (e.g., heavy metal ions and bacteria) based on the conductivity change of the semiconducting material (sensing channel) in the transistor when the contaminants attach to the sensing material surface. Since the amplitude of conductivity change usually depends on the contaminant concentration, the FET sensors could also quantitatively measure the contaminants in water.

The FET, as its name suggests, is a device that uses an electric field to control the conductivity of the charge carriers (holes or electrons) of the channel material.⁴⁷ FETs can be majority-charge-carrier devices, in which the current is carried predominantly by majority carriers, or minority-charge-carrier devices, in which the current is mainly due to a flow of minority carriers. As shown in Figure 1.1, the device consists of an active channel through which charge carriers, electrons or holes, flow from the source to the drain. Source and drain terminal conductors are connected to the semiconductor through ohmic contacts. The conductivity of the channel is a function of the potential applied across the gate and source terminals. FET contains a semiconductor layer formed by specific nanomaterial, therefore, it

could be used as an electronic sensor to stimulate and/or monitor chemical and electronic activities.

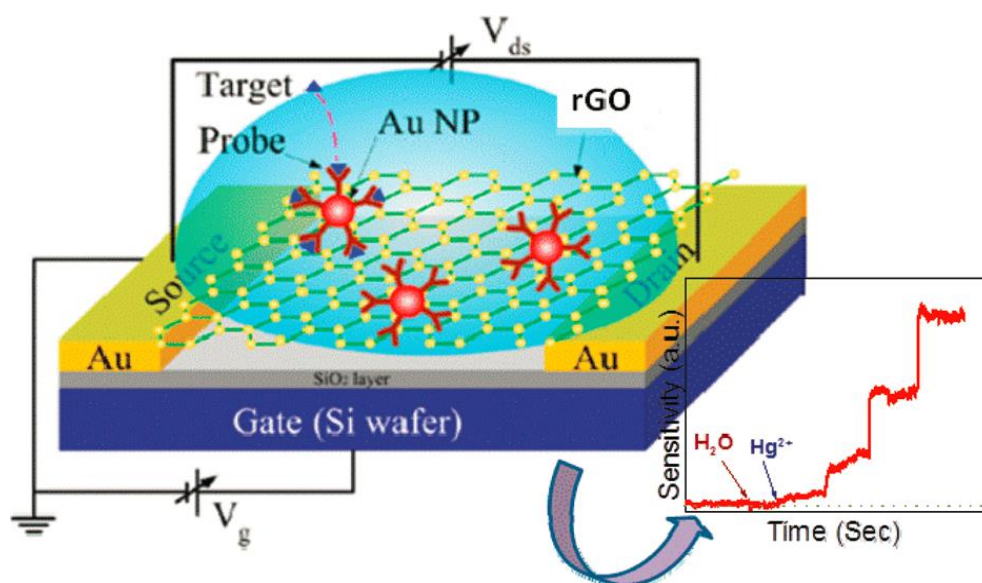


Figure 1.1 The schematic of the FET platform.

FET sensors based on nanomaterials, such as nanowires, nanotubes, and NPs, are emerging as a powerful sensing platform for the detection of chemical/biological species due to their various attractive features, including ultra-sensitivity, label-free, and real-time response⁴⁸⁻⁵² comparable with or better than those of conventional techniques (e.g., enzyme-linked immunosorbent assay/ELISA).⁵³ FET sensors are capable of label-free detection of heavy metals by using the interaction between the analyte and the semiconductor.⁵⁴ One and two dimensional (1D and 2D) semiconducting nanomaterials, such as a single-walled CNT or graphene, are especially attractive for FET sensors because they have very high surface-to-volume ratios and charge mobility, leading to high sensitivity.⁵⁵ Nanomaterials used as semiconducting channel materials usually require surface modification for the specific detection of chemicals,⁵⁶ which will degrade their electronic properties by generating defects through chemical or physical adsorption, resulting in the degradation of device performance

and instability.

Two basic sensing mechanisms for FET sensors are the electron transfer between the analyte and the semiconductor channel material and the gating effect. With charged ions adsorbed to the platform, it will induce electron transfer between the ions and the channel material, altering the carrier (i.e., holes or electrons) concentration in the channel film, and further introduce a current change between source and drain electrodes. Meanwhile, the charged ions adsorbed on the sensor surface would generate an electric field, which repels or attracts the carriers in the channel material and leads to the current change between source and drain electrodes.

For sensor applications, several indicators are crucial for their performance, including sensitivity, stability and selectivity. Sensitivity of a sensor is defined as the change in output of the sensor per unit change in the parameter being measured. Stability is another way of stating drift, that is, the extent to which a given input consistently results in the same output. Lifetime of a sensor is most commonly defined as the time when the first sensor failure occurs. While other definitions exist, there has not been any consensus on which quantitative lifetime definition is most useful. Selectivity refers to the specificity of the sensor to a given target, that is, the heavy metal ion. However, aiming at the sensitive detection of heavy metal ions, most sensors are for one time use only with a relatively short lifetime. As reported previously, this type of hybrid sensor has great potential for reuse if a proper method can be identified to detach target ions from the probes.⁵⁷ For practical applications of the nanomaterial/Au NP hybrid sensor, it is necessary to further investigate the reusability and the stability.

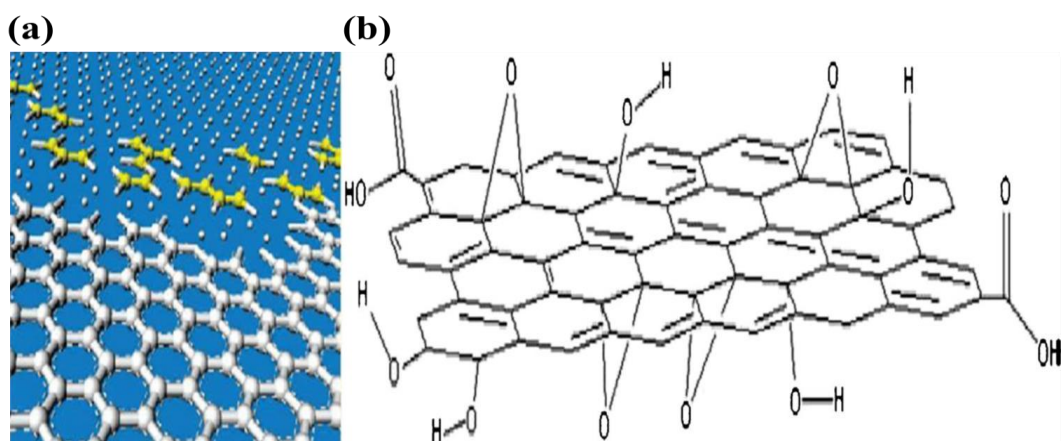


Figure 1.2 (a) The hexagonal structure model of graphene; (b) the oxygen functional groups on graphene sheet.⁵⁸

In principle, a FET sensor works by transducing and monitoring the adsorbates-induced perturbations into the conductance change in the channel materials, typically in terms of the source-drain current. The channel material with high surface to volume ratio is favored generally since it implies higher adsorption site density available, and it has been reported that semiconducting materials outperform the metallic ones in sensing.⁵⁹ Consequently, 2D semiconducting materials are promising candidates for sensing applications. As a model of 2D nanomaterials, graphene-based materials have been widely reported for electronic devices.⁶⁰ Recently graphene-based sensing platforms have been reported for the detection of various analytes.^{51, 61} Before that, graphene has drawn considerable scientific attention since its initial production through mechanical exfoliation by Novoselov and his co-workers in 2004,⁶² which led to the 2010 Nobel Prize in Physics.⁶³ Pristine graphene, GO and reduced graphene oxide (rGO) are all members of the ‘graphene family’. Graphene consists of 2D carbon atoms arranged in a regular hexagonal pattern similar to graphite, but it is a single layer of graphite, as shown in Figure 1.2(a). Graphene is relatively light, a 1 m² sheet weighs only 0.77 mg.⁶⁴ The International Union of Pure and Applied Chemistry (IUPAC) defines graphene as ‘a single

carbon layer of the graphite structure, describing its nature by analogy to a polycyclic aromatic hydrocarbon of quasi infinite size'.⁶⁵ Graphite is a naturally occurring mineral that is already used abundantly and poses no threat to the environment. It was named by Abraham Gottlob Werner in 1789 from the Ancient Greek, 'to draw/write', for its use in pencils, where it is commonly called 'lead' (not to be confused with the metallic element lead).⁶⁶ GOs are layered, oxygenated graphene sheets that contain oxygen functional groups, such as epoxides, carboxyls, hydroxyls, and alcohols, on their basal planes and edges (Figure 1.2(b)). Chemical analysis shows that the carbon to oxygen ratio is approximately 3:1.⁶⁷ Traditionally, GO is seen as a precursor to large-scale graphene synthesis.⁶⁸ GO can be reduced to almost graphene by chemical reduction,⁶⁹ electro-reduction,⁷⁰ thermal annealing,⁷¹ flash reduction,⁷² and enzymatic reduction,⁷³ and some possible applications of GO have recently been reported.^{64, 74} After reduction, GO transforms into rGO with some residual oxygen and structural defects, yielding high electrical conductivity comparable to that of doped conductive polymers, about 36 times higher than that of Si and about 100 times higher than that of GaAs.⁷⁵

Graphene exhibits many outstanding and unique properties. The zero band gap within the structure enables its ultrahigh electron mobility ($200,000 \text{ cm}^2 \text{ V}^{-1} \text{ s}^{-1}$), which is much higher than that of CNTs.⁷⁶ It has ultrahigh capacitance,⁷⁷ excellent thermal conductivity ($\approx 4,000 \text{ W m}^{-1} \text{ K}^{-1}$),⁷⁸ outstanding electrical conductivity ($3,189 \text{ S cm}^{-1}$)⁷⁹ with the monolayer graphene devices showing the half-integer quantum Hall effect,⁸⁰ mechanical strength,⁸¹ an extremely high surface-to-volume ratio ($2,600 \text{ m}^2 \text{ g}^{-1}$) and the possibility of atomically clean graphene sheets on lattice symmetry structure-free graphene.⁸¹ Besides these excellent properties, the exceptionally low electronic noise of graphene also enables the sensitive detection of various

analytes using graphene.⁸² GO naturally has functional groups (mainly carboxyl and hydroxyl groups) for the immobilization of target materials. In particular, rGO materials offer relatively high charge mobility, large detection area, relatively low 1/f noise, and tunable ambipolar field-effect characteristics.⁸³ The high electron mobility⁵¹ makes graphene highly sensitive to the external environment, which enables its potential applications for gas sensors, biosensors and heavy metal ion sensors.

However, the lack of a band gap in graphene significantly limits its application in transistor devices because it cannot reach a low off-state current.⁸⁴ In addition to graphene, molybdenum disulfide (MoS₂), which is a transition metal dichalcogenide, has been attracting increasing attention. MoS₂ film is only a single atomic layer thick, in which the molybdenum atoms are sandwiched between layers of sulfur atoms by covalent bonds, as shown in Figure 1.3 (a). The interaction between adjacent S-Mo-S layers is van der Waals force. In contrast to graphene with no band gap, MoS₂ is a semiconductor with a direct band gap of 1.8 eV for a single layer. MoS₂ FETs with the high on-off current ratio of $\sim 10^8$, high mobility ($200 \text{ cm}^2 \text{V}^{-1} \text{ s}^{-1}$) and good performance have also been recently reported. MoS₂ has been used in electronic devices and circuits based on FETs, because of its robust mechanical semiconducting properties, and it has gain significant attention for its future application in electronic circuits requiring low stand-by power. These excellent electrical properties, high flexibility and good transparency enables the application of MoS₂ to be flexible electronics. Furthermore, the development in the synthesis of 2D materials improves the possibility of the mass production, great mount integration of 2D electronic materials.⁸⁵⁻⁸⁷ Many methods have been developed to synthesize MoS₂, such as exfoliation of bulk MoS₂ via Li intercalation,⁸⁸ scotch tape based micromechanical

exfoliation,⁸⁹⁻⁹¹ liquid exfoliation,⁹² chemical vapor deposition (CVD),⁹³⁻⁹⁴ physical vapor deposition,⁹⁵ and thermolysis of single precursor containing Mo and S.⁹⁶

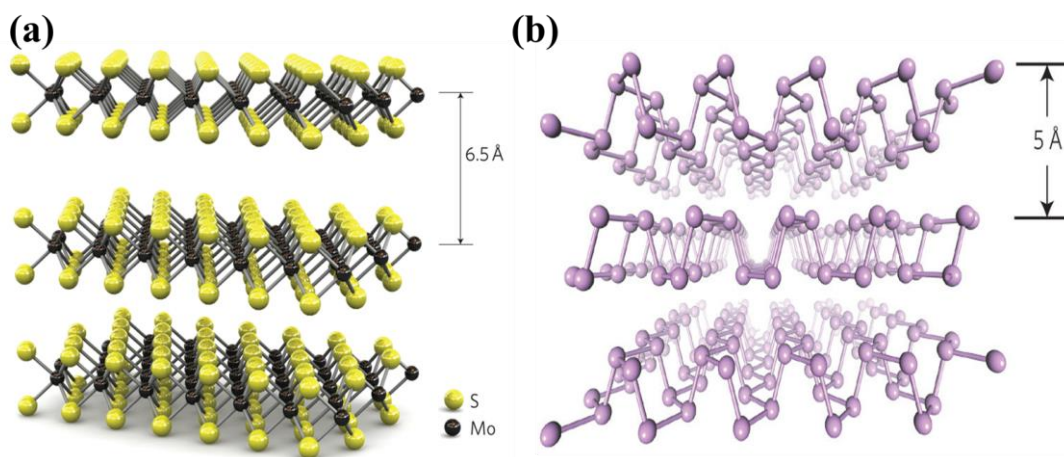


Figure 1.3 (a) Atomic structure of monolayer MoS₂ of 6.5 Å thick.¹ (b) Atomic structure of black phosphorus of 5 Å thick.⁹⁷

Black phosphorous (BP) is a layered material with atomic layers stacked onto each other through van der Waals force, as shown in Figure 1.3(b). In each single layer, phosphorus atom is covalently bonded with three adjacent atoms to form a puckered honeycomb structure. With the similar structure to graphite, it could also be micromechanically exfoliated into ultrathin nanosheets from the bulk BP crystal. Currently, mechanical exfoliation, liquid exfoliation, CVD methods and sonochemical synthesis have been reported for layered BP synthesis.⁹⁷⁻⁹⁸ BP nanosheet is a p-type semiconductor and has thickness-dependent and tunable band gaps ranging from 0.3 eV for bulk BP to 2 eV for monolayer BP nanosheet (phosphorene).⁹⁹⁻¹⁰¹ It covers the gap of band gaps between graphene and 2D Transition metal dichalcogenides (TMDs), as shown in Figure 1.4. Few-layer BP nanosheets based FET shows both excellent carrier mobility (up to 1,000 cm²V⁻¹s⁻¹) and high on/off current ratio ($\sim 10^5$)¹⁰¹ with well-

developed current saturation in the transfer characteristics at room temperature. Thus, BP also has great potential in the FET sensor applications.¹⁰¹⁻¹⁰³ Cui and Pu et al. designed ultrahigh sensitivity sensing performance based on phosphorene for the sensing of NO₂ detection at the parts per billion (ppb) level in dry air.¹⁰² Its main disadvantage is the poor air stability under ambient condition.¹⁰⁴ But researchers have identified the application of encapsulation or passivation layer would help BP maintain its good electronic properties and enable its stable performance in different applications under ambient condition.¹⁰⁵

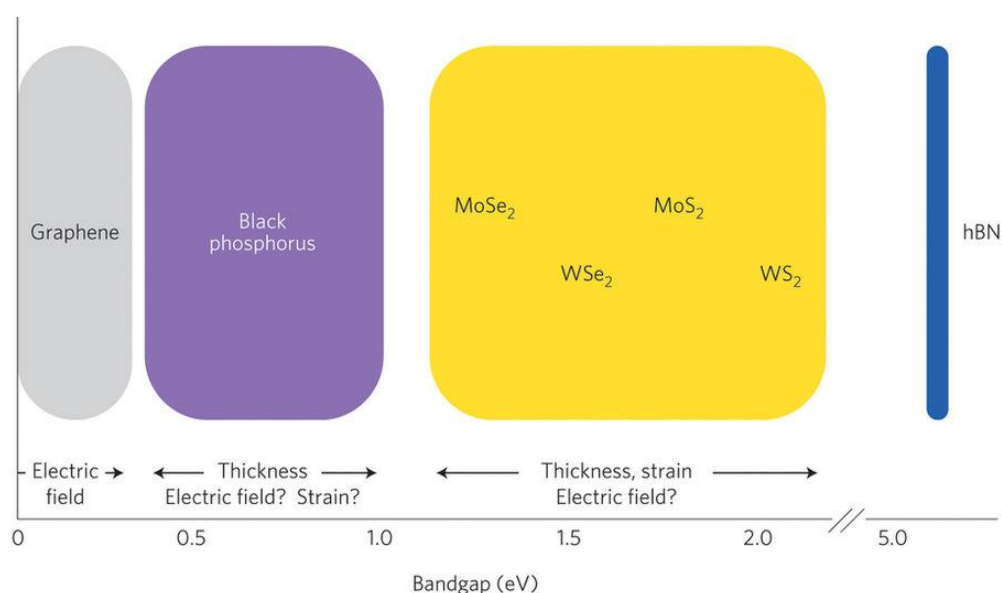


Figure 1.4 Bandgap energies of several layered materials used for nanoelectronics. The range of values for each material can be achieved through a variety of means. For example, it is expected that variations in an applied perpendicular electric field, film thickness or strain could modify the bandgap value. hBN, hexagonal boron nitride.¹⁰⁶

Attributed to their outstanding properties (i.e., intrinsic ultrahigh carrier mobility, high surface-to-volume ratio), rGO, MoS₂ and BP have been widely demonstrated for analyte detection, including metal ions, bacteria, proteins, and DNAs in aqueous environment. Table 1.2 summarizes their performance in terms of rapid response and lower detection limit (M is

mol/L). The theoretical analysis in Section 5.2 suggests a lower limit of detection (LOD) and a higher sensitivity could be achieved through making films with a larger band gap, a higher carrier mobility, and a smaller film thickness. Among the three materials, MoS₂ and BP have a tunable band gap, as shown in Figure 1.4. The band gap of rGO could be tuned through the degree of reduction. BP is challenged by its poor stability in ambient environment due to oxidation; however, it could be potentially addressed through applying a passivation layer or encapsulation to prevent BP from exposure to O₂, thereby improving the sensor stability.

Table 1.2 2D nanomaterial-based FET sensors and their application in aqueous sensing.

Channel material	Key sensing structure	Target	LOD	Advantages	Disadvantages	Ref
mono-layer rGO	rGO/AuNPs/GSH	Pb ²⁺	10 nM	quick response, good selectivity		52
mono-layer rGO	rGO/TGA/Au NP	Hg ²⁺	25 nM	quick response, good selectivity		107
mono-layer rGO	rGO/ferritin/FE T	HPO ₄ ²⁻	26 nM	quick response, good selectivity		108
mono and multilayer graphene	DNAzyme-AuNP-graphene	Pb ²⁺	20 pM	high selectivity, extreme sensitive	long response time (20 minutes)	109
multilayer - rGO	MT-II functionalized	Hg ²⁺ & Cd ²⁺	1 nM, 1 nM	rapidly, sensitive	lack of selectivity	55
large-sized graphene film	anti-E. coli antibody functionalized	<i>E.coli</i>	10 cfu/mL	fast, label-free		110
multilayer MoS ₂	MoS ₂ /AuNPs/DNA	Hg ²⁺	0.1 nM	higher sensitivity than rGO		48
multilayer MoS ₂ flakes	MoS ₂ /ionophore	AsO ₂ ⁻	0.1ppb/0.93nM	the sensitivity superior to that of graphene.		111
four-layer MoS ₂	MoS ₂ /HfO ₂ /biotin	streptavidin	100 fM	73-times higher sensitivity comparing to graphene		112

multilayer MoS ₂	MoS ₂ /HfO ₂ /anti-PSA antibody	PSA	375 fM	low detection limit		113
mono-layer MoS ₂	MoS ₂ /wsMOR	DAMGO	3 nM	wafer-scale, high-yield fabrication		114
multilayer MoS ₂	MoS ₂ /DNA	DNA	10 fM	good selectivity		115
multilayer BP	BP/AuNPs/DTT	As (V) & As(III)	1 nM		easy to be oxidize, encapsulation is needed	116
multilayer BP	BP/Al ₂ O ₃ /anti-IgG	IgG	0.065 nM	enhanced stability and sensitivity, no responses to avidin		117
multiplayer BP (12 nm)	BP/lead ionophore	Pb ²⁺	1 ppb/5 nM	ionophore encapsulated makes it air-stable, high selectivity		118
thick BP nanoflake (26 um)	/	humidity	10% RH	three months' stability to ambient condition (25 °C and 25 ± 12% RH)	exposure to high-humidity levels for 72 h degrades & oxidizes the BP	119

It is important to note that other nanomaterials, such as nanoporous and mesoporous materials, were also widely studied for heavy metal ion detection.¹²⁰⁻¹²¹ The nanoporous materials offer an alternative means of immobilizing small molecules. Santos et al. developed an innovative portable and cost-competitive sensing system that combines chemically-modified nanoporous anodic alumina rugate filters (NAA-RFs) for sensing Hg²⁺ ions in environmental water by measuring shifts in the reflection peak position of reflection spectroscopy (RfS).¹²¹

1.4 Objectives and outline of the dissertation research

As reviewed in the above sections, the 2D nanomaterials-based FET device fabricated on a silicon platform can be used in a label-free manner to rapidly detect various metal ions in solutions with a high sensitivity and a low detection limit. The overall objective of the dissertation research is to explore and understand 2D nanomaterials-based FET sensors for water sensing applications. To achieve this objective, the thesis research is organized as follows.

Firstly, in Chapters 2-4, various 2D nanomaterials are explored based on their unique properties for the demonstration of sensitive, selective electronic sensors for toxic heavy metal ions, e.g., mercury, lead and arsenic. These metal ions are notably toxic, harmful to the environment and human health. Specific probes are selected to realize the selective detection of target ions in the presence of other interfering metal ions. During the cumulative addition of metal ions to specific sensor platform, the drain current versus time is monitored. Since the current change depends on the contaminant concentration, the FET sensors can quantitatively measure the contaminants in water. To this end, the simple fabrication method and excellent sensing performance of the hybrid structure are used for the accurate prediction of arsenic ions in lake water (Chapter 4).

Secondly, sensing mechanisms of the FET platform are deeply investigated in Chapter 5. Based on the dynamic response of the sensors to various metal ions, mechanisms of the FET platform are investigated by examining the adsorption of target metal ions and the competition between the charge transfer effect and the gating effect. Further exploration is carried out through theoretical analyses and AC impedance spectroscopy, revealing that gating effect dominates over charge transfer in the sensing platform.

The remaining part of Chapter 5 and Chapter 6 investigate the sensitivity and stability improvement of the FET sensor, respectively. To improve the sensitivity, a few factors related to the channel material are addressed, such as the on/off current ratio, the band gap and the sensor film thickness. Other factors include the areal density of anchoring sites on the sensor surface and the adsorption of detecting probes. Further investigation into the sensitivity improvement is carried out through theoretical analyses and experimental validation. To improve the stability of the nanomaterial-based electronic sensor, the stability of electrodes, the bonding between the nanomaterials and the electrodes, the stability of nanomaterials in different environments, the detachment of Au NPs, and the lifetime and diffusion of probes are investigated. A passivation layer is proposed and used to protect the channel material from oxidation, thereby enhancing the sensor stability. An attempt has been made to practically integrate the FET sensor into flowing water equipment for inline heavy metal ion detection.

The conclusions and future research directions are summarized in Chapter 7.

CHAPTER 2 REAL-TIME, SELECTIVE DETECTION OF Pb^{2+} IN WATER USING A REDUCED GRAPHENE OXIDE/GOLD NANOPARTICLE FIELD-EFFECT TRANSISTOR*²

2.1 Introduction

Lead poisoning has been documented since ancient Rome, ancient Greece, and ancient China. Recently, there have been numerous reports on the leaching problem of lead from water piping systems to drinking water,¹²² which has become a health threat, especially for young children and infants. Excessive lead damages the central nervous system and causes brain and blood disorders in mammals.¹² In this chapter, rGO, with its outstanding electronic properties, has been utilized as the semiconducting channel material to fabricate the rGO/GSH-Au NP hybrid sensor for the rapid, sensitive and selective detection of lead ions in water. In section 2.2, the device fabrication process is introduced in detail, within which rGO is fabricated through a self-assembly method. An l-glutathione reduced is employed as the capturing probe for the label-free detection of Pb^{2+} ions. Various techniques, including scanning electron microscopy (SEM), atomic force microscopy (AFM) and Raman spectroscopy, are used to characterize the morphology of the platform, the thickness and the structure of rGO film, respectively. In Section 2.3, by monitoring the electrical characteristics of the FET device, the performance of the sensor is measured and investigated. We discuss the performance of detecting Pb^{2+} ions in water, in terms of the lower detection limit and the response time. And a

*² This chapter has been published.

group of control experiments are carried out to investigate the selectivity of the rGO/GSH-Au NP sensor to Pb^{2+} ions.

2.2 Experimental methods

2.2.1 Material:

Purified natural graphite was purchased from SP-1. Bay Carbon, MI. KMnO_4 , NaNO_3 , H_2SO_4 , l-glutathione (GSH), alpha-ethyl-tryptamine (AET) and the blocking buffer (0.1% Tween 20) were all purchased from Sigma-Aldrich. Au NPs were sputtered with an RF (60Hz) Emitech K550x sputter coater apparatus using an Au target. Ag^+ , As(V) , Cd^{2+} , Cu^{2+} , Hg^{2+} , Zn^{2+} and Pb^{2+} solutions were prepared by adding chloride salts in deionized (DI) water (Cellgro). The assay of Pb^{2+} in experiment samples was characterized using the ICP-MS method.

GO was synthesized using the modified Hummer's method¹²³. First, the purified natural graphite was oxidized through treatment with KMnO_4 and NaNO_3 in concentrated H_2SO_4 .¹²⁴ Due to the presence of its inherent oxygen-containing functional groups, graphite oxide has excellent water solubility, strong hydrophilicity, and a facile surface-functionalization feature; thus, it can be fully exfoliated in water to form GO. Then, the GO dispersion was centrifuged to remove possible agglomeration materials. Finally, with the assistance of ultra-sonication, individual GO sheets were obtained from the stable suspension.¹²⁵

2.2.2 Device Fabrication:

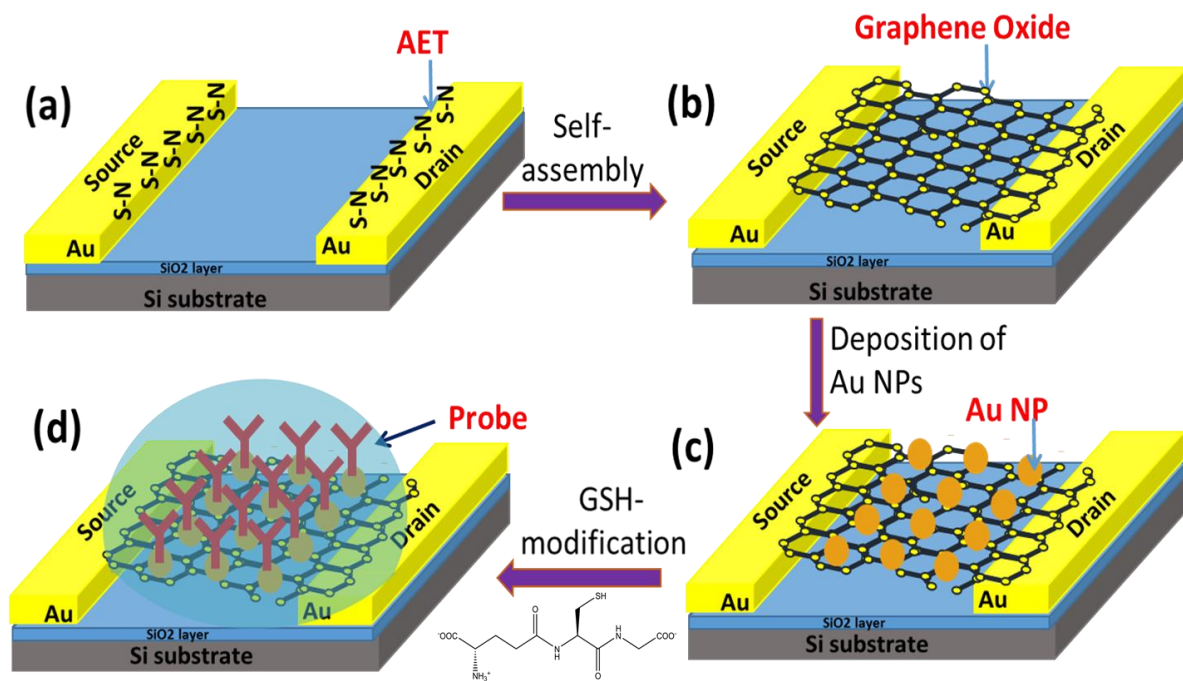


Figure 2.1 Schematic diagram of the rGO/GSH-Au NP hybrid sensor fabrication process: (a) a layer of AET coating on the bare interdigitated electrode surface; (b) self-assembly of GO monolayer sheets on the AET-modified electrodes, which is followed by the thermal reduction of GO to rGO; (c) the assembly of Au NPs onto the rGO film; (d) GSH-modification of Au NPs on the rGO sheet surface to form specific recognition groups to detect Pb^{2+} ion.

To guarantee the electronic stability of the device, we used an electrostatic self-assembly method to control the uniformity of the GO film. In this method, an amino-terminated Au electrode was employed to anchor the GO. Figure 2.1 (a) and (b) illustrate the chemical anchoring procedure of a monolayer AET film. The electrode was immersed in an AET (1 mg/mL) solution for 10 min to adsorb a monolayer of AET onto the electrodes, as shown in Figure 2.1(a). When immersing the electrode in the GO solution, GO sheets self-assembled onto the electrode, as illustrated in Figure 2.1(b). One droplet of the GO suspension was pipetted onto the electrode and dried at room temperature ($\sim 25\text{ }^{\circ}\text{C}$). Single GO layer was attached onto the electrode, and excessive GO was removed with the assistance of sonication. Thermal reduction was conducted in a tube furnace (Lindberg Blue, TF55035A-1) by heating

the device for 1h at 400 °C. After the thermal heating, samples were spontaneously cooled to room temperature. Several cycles of washing and drying were carried out. Figure 2.1(c) and (d) show the deposition of Au NPs onto the rGO surface and the functionalization of Au NPs with GSH probes.¹²⁶ Here we deposited Au NPs for 2s using an RF (60Hz) Emitech K550x sputter coater apparatus using an Au target (99.999% purity), at an Ar pressure of 0.03 mbar and a working current of 10 mA. A uniform Au NP film of 2 nm thick resulted, as shown in Figure 2.1(c). GSH is an organic compound which was chosen to be the probe for the specific detection of lead ions. The Au NPs were functionalized with GSH groups by immersing the device in a 10 mM GSH solution at 25 °C for 1h. Then the sensor was rinsed with DI water for several times to remove extra GSH and dried with a stream of nitrogen gas. A self-assembly monolayer of GSH was formed on the gold surface, as shown in Figure 2.1(d). Finally, the device was incubated with a blocking buffer for 2h at room temperature and washed with the DI water. A three-terminal FET device was employed to measure the device transport characteristics. The drain current (I_{ds}) was measured as a function of the gate voltage (V_{gs}) and a function of the drain voltage (V_{ds}), with the gate bias varying from -40 to +40 V.

2.2.3 Measurement:

Electrical and transport measurements were performed on rGO/GSH-Au NP hybrid structure sensors using a Keithley 4200 semiconductor characterization system, with a back-gate applied to the FET device at room temperature. By measuring the change in the electrical characteristics of the device, we achieved the electrical detection of the target agent that was bound to the probes. The electrical conductance of the device was recorded by monitoring the change in the drain current (I_{ds}) for a fixed source–drain voltage (V_{ds}) when the device was

exposed to different concentrations of target solutions. To further confirm the sensor repeatability, the detection process was repeated using 3–4 sensors, which showed similar sensing responses.

2.2.4 Characterization:

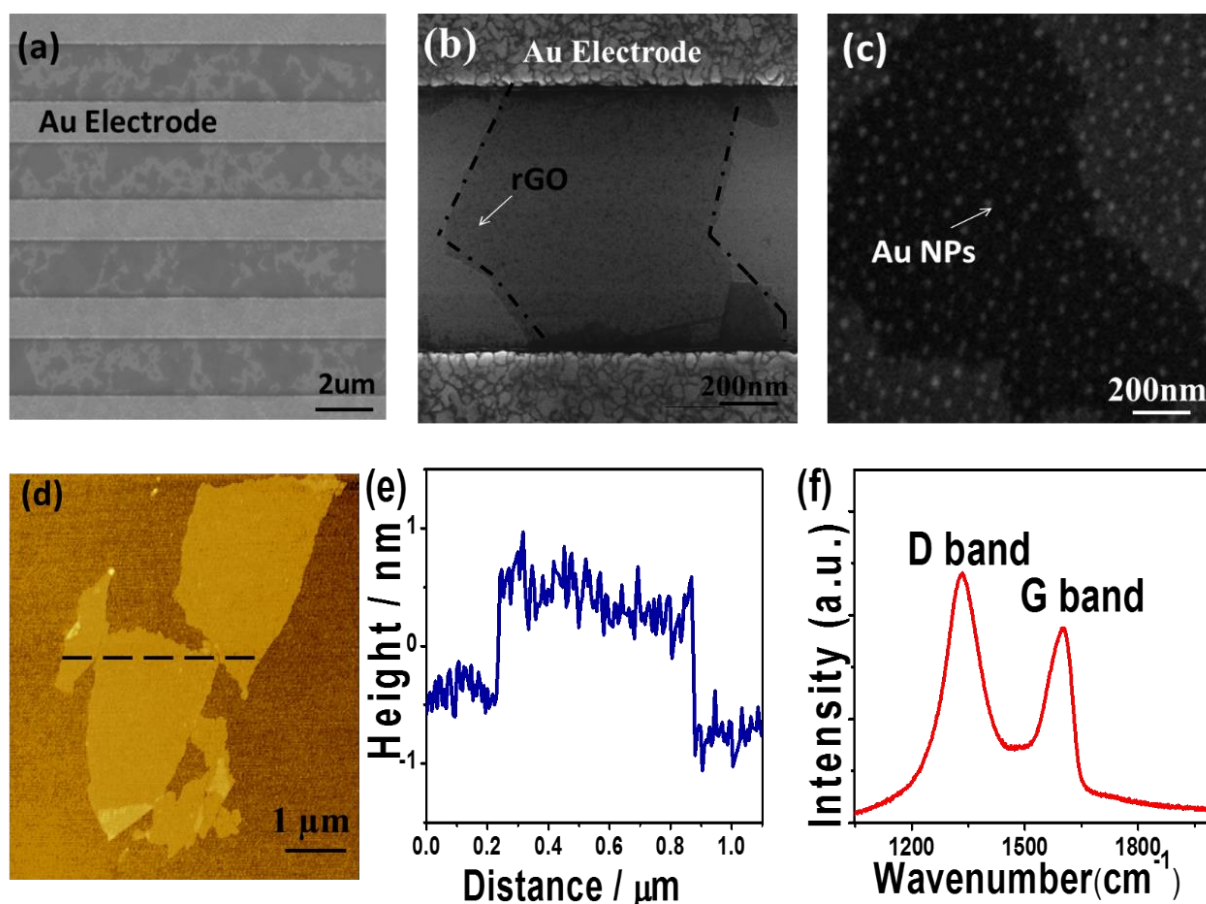


Figure 2.2 (a) and (b) SEM images of rGO sheets spanning across the interdigitated electrodes, showing transparency to the electron beam; (c) SEM image of the rGO sheet decorated with Au NPs of 2 nm thick; (d) and (e) AFM (tapping mode) height image and profile of rGO with the dashed line indicating the scanning trace; (f) Raman spectrum of the rGO.

The morphology of the rGO sheets was characterized by a Hitachi S4800 field-emission SEM at a 2-kV acceleration voltage. Figure 2.2(a) shows the SEM image of a transparent rGO sheet spanning across a pair of Au interdigitated electrodes. The Au interdigitated electrodes are about 2 mm long and 50 nm thick, with both finger-width and inter-finger spacing that

separates the source and drain terminals around 2 μm . The width of and the gap between the electrodes are balanced between the size of synthesized GO flake and the technology limitation of microelectronic fabrication. The electrodes were fabricated using a photolithographic process on a highly doped Si wafer with an upper layer of dry-formed SiO_2 (thickness of 200 nm). Here the Au electrodes bond with the SiO_2 surface through a “metallic glue” -- Ti thin film, which has a stronger bonding force to SiO_2 and works as an adhesion layer to Au electrodes.¹²⁷ Normally, GO is electrically insulating with a resistance on the order of tens of $\text{G}\Omega$. The high resistance results from the abundant saturated sp^3 bonds and high density of electronegative oxygen atoms bonded to carbon atoms. SEM imaging was periodically conducted, which suggested the reliable immobilization of rGO sheets on the electrodes. Lateral dimensions of rGO typically ranged from several hundred nanometers to several micrometers, as shown in Figure 2.2(b). When the Au NPs were sputtered, isolated Au NPs uniformly distributed on the surface of the rGO sheet without any aggregation, as shown in Figure 2.2(c). It was the physical adsorption between Au NPs and rGO that retained the Au NPs on the rGO surface even after several cycles of rinsing in deionized water and drying. Figure 2.2(d) and 2.2(e) are an AFM image and a height profile of rGO, by scanning from bare silicon substrate surface to rGO. The film thickness was estimated as ~ 1 nm, corresponding with the typical thickness of a single-layer graphene oxide sheet (~ 0.8 nm),¹²⁸ which suggested that the GO film in our sample was monolayer. Raman spectrum for the rGO in Figure 2.2(f) shows that the D band is higher than the G band, indicating the abundance of defects in the rGO.¹²⁹

2.3 Results and discussion

AET adsorbed onto the Au electrode surface through the strong affinity of sulfur in the thiol functional groups.¹³⁰ On one hand, the electrostatic adsorption between functional groups (e.g., carboxylic acid) on the GO surface and amino groups of the AET¹³¹ enabled the first GO layer to strongly adhere to AET. On the other hand, because of the weak binding between additional layers and the first layer next to the electrode, excessive GO layers were removed through sonication.

Thermal annealing was conducted to remove residue solvents, reduce the GO sheets, improve the contact, and reduce the junction barrier between the Au electrode and GO sheets. Argon at a flow rate of 0.6 liter per minute is necessary to create an anaerobic atmosphere and to reduce oxygen-containing groups. Hence the Au electrodes and rGO sheets work as the conducting channel for the sensor device. The conductance of the rGO was dependent on annealing temperature, annealing time, and annealing gaseous environment.¹³² After the self-assembly of rGO, we need to create anchoring sites for immobilizing probes. Here Au NPs were chosen because their excellent functionalization can be used to improve the sensor performance.¹³³ The pre-existing abundance of thiolate groups on Au NPs allowed the incorporation of a wide range of molecules onto the surface of the GO sensor.¹³⁴

In the present study, GSH links with Au NPs through -SH linkage.¹³⁵ The transmission electron microscopy (TEM) imaging and UV-visible spectroscopy¹³⁶ of GSH- modified Au NPs have been reported. As shown in Figure 2.1(d), GSH molecule has two free -COOH groups and one -NH₂ group, which provide a hydrophilic interface and a handle for functionalization with metal ions.¹³⁷ The complexation between GSH and Pb²⁺ in an aqueous solution has

previously been studied by ^{13}C and ^1H NMR methods within a pH range 5.4–12.0.¹³⁸ A blocking buffer was employed to shield the interaction between the rGO and Pb^{2+} , as anions of rGO would have electrostatic interactions with Pb^{2+} , affecting the specific interaction between Pb^{2+} and GSH.

The sensor was exposed to DI water with $10\ \mu\text{M}$ Pb^{2+} , and Pb^{2+} affected the conductivity of the rGO/GSH-Au NP hybrid sensor. The channel conductance changed sensitively due to the electron donating and withdrawing effect of target ions. In this FET device, a positive gate voltage leads to a depletion layer by repelling the positively charged holes away from the gate-insulator/semiconductor interface, thus producing a carrier-free region of immobile and negatively charged acceptor ions. Here, Au NPs work as the gate in the FET device.¹³⁹ Due to the effective electronic transfer between the rGO and Au NPs, the adsorption of target ions onto probes may lead to a carrier concentration change in rGO. As shown in Figure 2.3(a), the Dirac point of the sensor shifted $\sim -10\ \text{V}$ because of the immobilization of Pb^{2+} ions. The negative shift of the Dirac point can be attributed to the field effect of positive Pb^{2+} on the graphene channel. In the p-channel depletion-mode FET device, once the metal ions bond to the hybrid sensor, the positive electrical field of the Pb^{2+} will force the holes away from the gate-insulator/semiconductor interface, leading to a difference in the charge carrier concentration within rGO sheets, a decrease of the hole concentration in the rGO sheet, and the formation of a depletion layer,¹⁴⁰ which consequently causes the reduction of the electrical conductivity of the rGO channel in the rGO-FET device. Therefore, compared with water, the exposure to Pb^{2+} reduced the electrical conductance through the hole-transport branch of the graphene device.

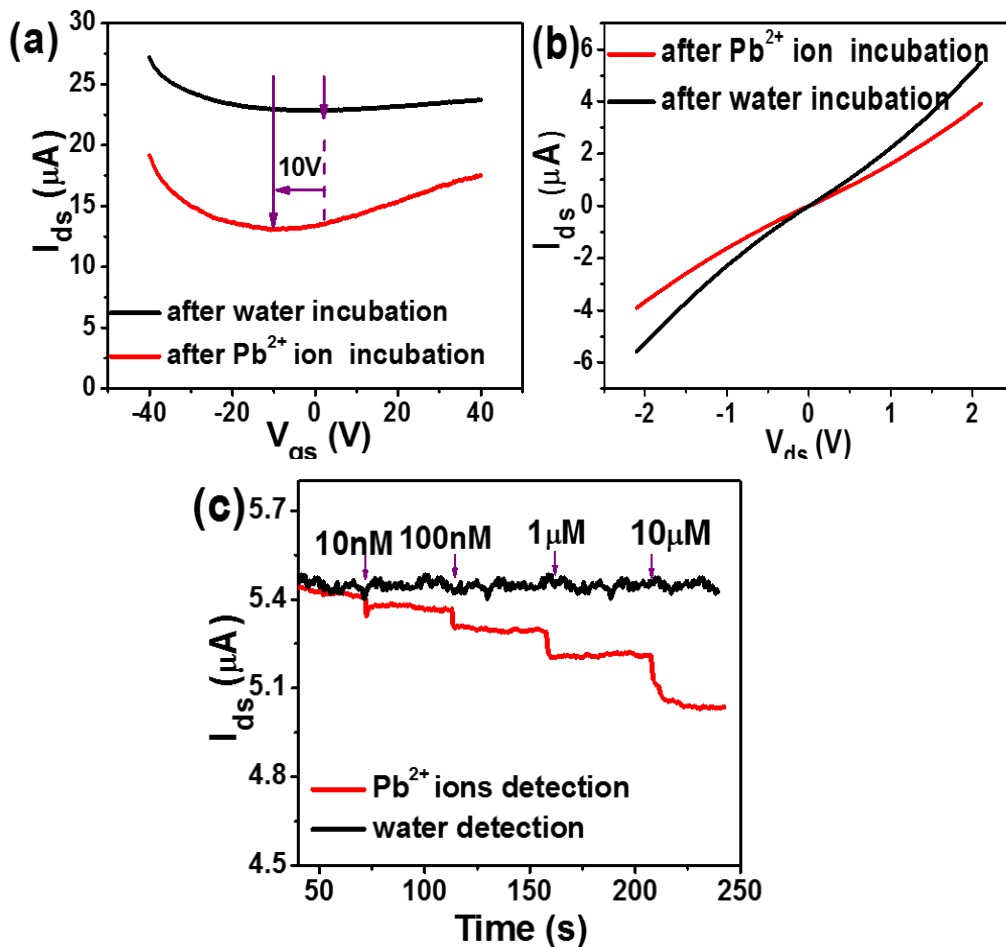


Figure 2.3 (a) I_{ds} - V_{gs} ($V_{ds} = 5$ V, $V_{gs} = -40$ V~40 V, step = 0.2 V), (b) I_{ds} - V_{ds} ($V_{ds} = -2.1$ V~2.1 V, step = 0.1 V) characteristics of an rGO/GSH-Au NP hybrid sensor exposed to water (black) and 10 μ M Pb^{2+} solution (red) and (c) real-time detection ($V_{ds} = 0.1$ V) of Pb^{2+} in water with the rGO/GSH-Au NP hybrid sensor. Lower detection limit: 10 nM (0.002 mg/L).

Figure 2.3(c) shows the dynamic response of the rGO/GSH-Au NP hybrid sensor as a function of Pb^{2+} concentration ranging from 10 nM to 10 μ M. During the cumulative addition of Pb^{2+} to the sensor, the drain current versus time was monitored. The sensor responded within a few seconds to the Pb^{2+} due to the diffusion of ions from the liquid drop on the top of the device to the contact area. This is much faster than conventional fluorescence sensors, which take minutes or even hour.^{129, 141-142} With the cumulative addition of the Pb^{2+} solution, the conductance of the device decreased gradually, and the rate of the decrease, or percentage

change, was in direct proportion to the concentration of Pb^{2+} . The lower detection limit is 10 nM, defined as the concentration corresponding with a signal-to-noise ratio of approximately 3^{143} . And it is 5 times lower than the maximum contaminant level (MCL) for Pb^{2+} ions in drinking water defined by the World Health Organization (WHO).¹⁴⁴

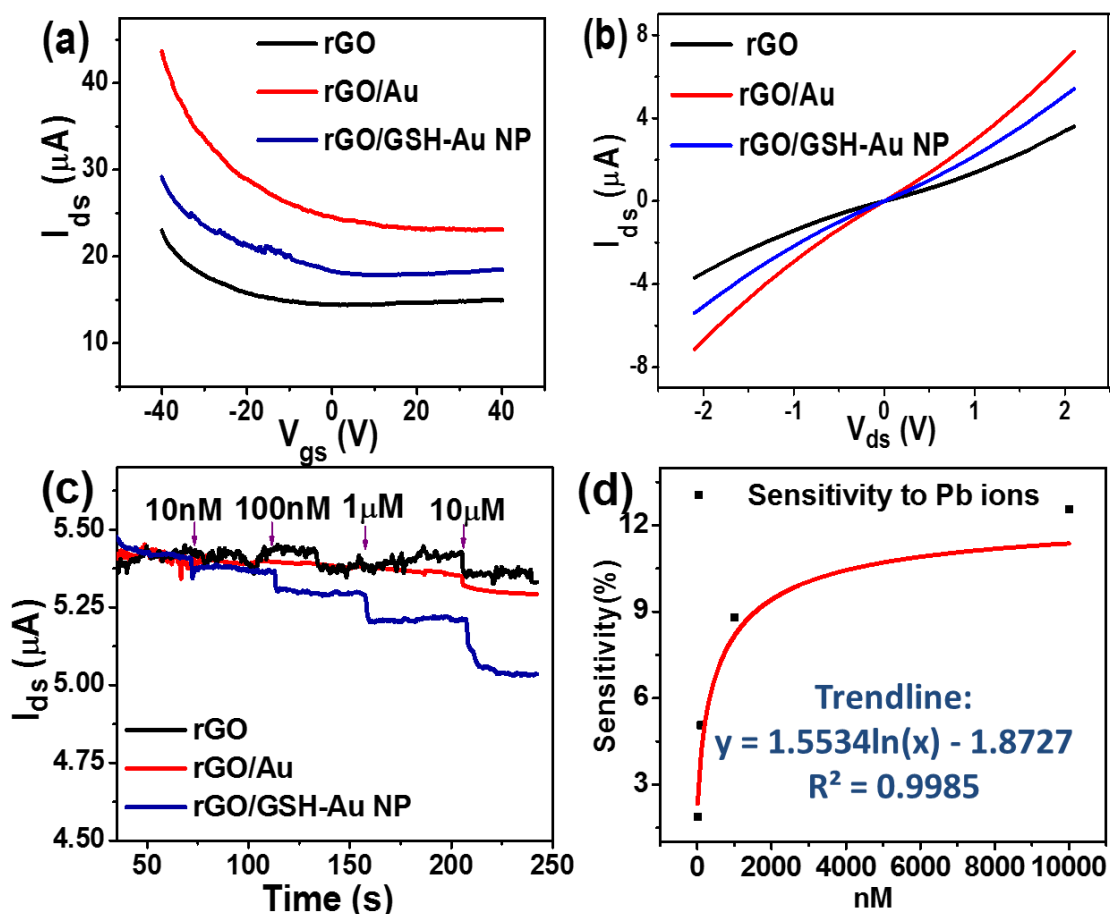


Figure 2.4 (a) I_{ds} - V_{gs} ($V_{ds} = 5$ V, $V_{gs} = -40$ V~40 V, step = 0.2 V), (b) I_{ds} - V_{ds} ($V_{ds} = -2.1$ V~2.1 V, step = 0.1 V) characteristics of various devices, (c) I_{ds} versus time ($V_{ds} = 0.1$ V) (dynamic responses) of rGO-based sensing platforms: rGO (black), rGO/Au (red), rGO/GSH-Au NP (blue), and (d) the sensitivity trendline of the rGO/GSH-Au NP hybrid sensor to Pb ions ranging from 10 nM to 10 μM : $y = 1.5534\ln(x) - 1.8727$, $R^2 = 0.9985$.

We designed a control experiment to investigate the function of Au NPs and GSH probes in the hybrid sensing platform. As shown in Figure 2.4, three types of sensors were fabricated. The first was the bare rGO device without decorating any Au NPs or GSH-functionalized Au

NPs. Figure 2.4(c) shows that the device did not respond to Pb^{2+} ions, implying that there was no significant binding between rGO and Pb^{2+} . The second sensor was fabricated with rGO and Au NPs without the functionalization of GSH probes. As Figure 2.4(c) shows, the rGO Au-NPs hybrid device was insensitive to the presence of Pb^{2+} . In the third device, rGO film was modified with GSH-functionalized Au NPs, which was highly sensitive to the addition of Pb^{2+} .

In Figure 2.4(a) and 2.4(b), the typical electrical characteristics, $I_{\text{ds}}-V_{\text{gs}}$ and $I_{\text{ds}}-V_{\text{ds}}$ curves of these three types of sensors are presented. The deposition of Au NPs enhanced the drain current of the rGO film, which could be attributed to two competing factors. On one hand, comparing the work function of Au NPs (5.1–5.47 eV) and rGO (4.4–4.65 eV),¹⁴⁵ electrons would transfer from the rGO to the Au NPs, increasing the density of holes in the rGO film and thereby increasing the drain current. The other factor is that when Au NPs are sputtered onto the rGO film, they enlarged the scattering center across the film, hence reduced the mobility of the holes of the film and leading to a decrease in the drain current. According to the increased drain current, it can be inferred that the electron transfer mechanism dominated in this case. However, the assembly of negatively charged GSH molecules onto Au NPs weakened the drain current enhancement that was introduced by the deposition of Au NPs, possibly because GSH was negatively charged and negative charges would transfer from GSH to rGO. Overall, the drain current of the rGO/GSH-Au NP hybrid sensor increased compared with the GO device. Compared with the pure rGO film sensing platform and the sensor fabricated with an rGO film and Au NPs, the assembly of a stable GSH-functionalized Au NP structure onto an rGO-based platform could achieve excellent Pb^{2+} detection, according to the electrical characteristics and the dynamic response (Figure 2.4(c)).

To explore the specificity of the GSH probe to Pb^{2+} , we monitored the dynamic response of the hybrid sensor to several mineral elements that are necessary for human health.¹⁴⁶ As Figure 2.5 shows, the sensor response to Na^+ and Ca^{2+} is rather weak. However, when exposed to Fe^{3+} , the sensor conductivity showed some changes, which may result from the strong affinity of Fe^{3+} to carboxylic groups on rGO.¹⁴⁷ However, the interference of Fe^{3+} is obvious only when its concentration exceeds $1\ \mu\text{M}$, suggesting that rGO/GSH-Au NP hybrid sensor is still selective to Pb^{2+} , with the Fe^{3+} at a concentration lower than $1\ \mu\text{M}$.

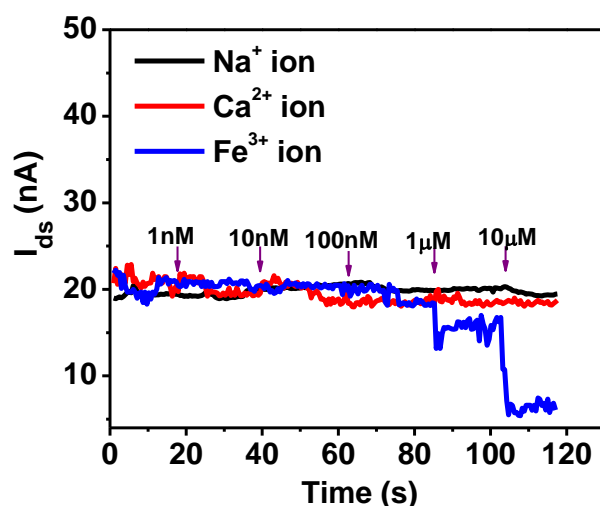


Figure 2.5 Dynamic responses ($V_{ds} = 0.36\text{mV}$) of the rGO/GSH-Au NP hybrid sensor to common metal ions: Na^+ , Ca^{2+} , Fe^{3+} .

To further confirm the specificity, we also investigated the behavior of the hybrid sensor when it was exposed to a variety of common heavy metal ions: Ag^+ , As(V) , Cd^{2+} , Cu^{2+} , Hg^{2+} , Pb^{2+} , Zn^{2+} , and mixed solution of these six kinds of ions ($10\ \mu\text{M}$). The I_{ds} characteristics and relative current changes are presented in Figure 2.6(a) and (b). Compared with the significant responses of Pb^{2+} and the ion mixture, the responses of the hybrid sensor to Ag^+ , As(V) , Cd^{2+} , Cu^{2+} , Hg^{2+} and Zn^{2+} ions were much weaker, due to the fact that amidogen, thiol and carbonyl groups of GSH favor binding with Pb^{2+} . The increasing relative change can be attributed to the

decreasing hole concentration in the rGO sheet.¹⁴⁰ As suggested by the previous work, the positively charged holes are forced away from the gate-insulator/semiconductor interface by the positive electrical field of the Pb^{2+} , and the hole concentration in the rGO sheet decreases. As a result, a depletion layer is created, leading to the conductance change in the rGO-FET device.

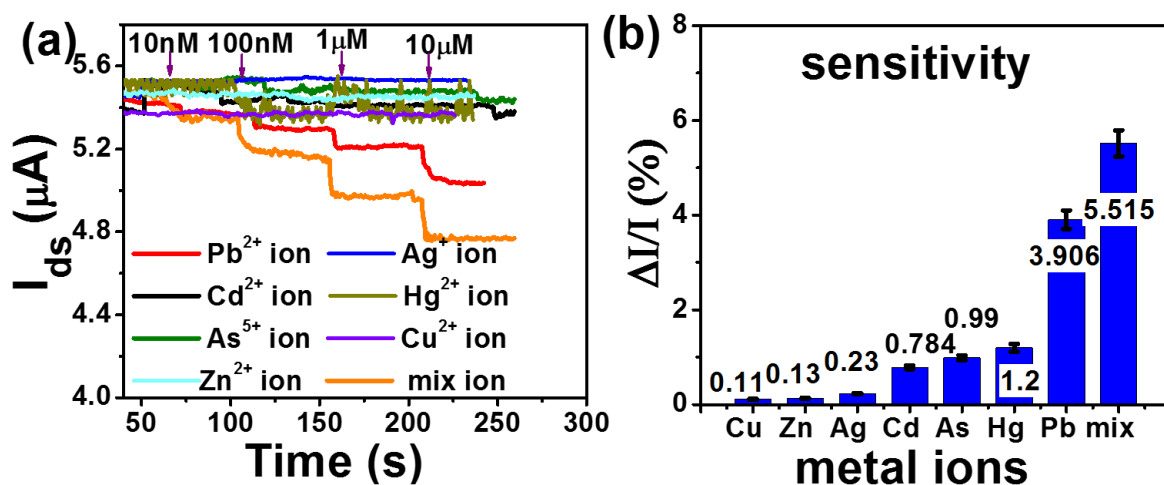


Figure 2.6 (a) Dynamic responses ($V_{ds} = 0.1$ V) to varying concentrations of heavy metal ions and (b) relative current change of an rGO/GSH-Au NP hybrid sensor in response to various heavy metal ions: Ag^+ , As(V) , Cd^{2+} , Cu^{2+} , Hg^{2+} , Pb^{2+} , Zn^{2+} , and a mixed solution of the six ions (10 μM for total).

With the development of advanced biochemical, electrochemical, physical detection technologies, various methods have been created for the detection of Pb^{2+} , with significant progress being made in the lower detection limit. For example, the colorimetric sensor of GSH-functionalized Au NPs had a lower detection limit of 100 nM¹³⁷, and catalytic beacon-based fluorescent sensor with functional DNAzyme had a lower detection limit of 10 nM.¹⁴⁸ In the fluorescent method, the lower detection limit of the GO/aptamer QD sensor was 0.09 nM.¹⁴³ An electrochemical SnO_2/rGO sensor based on FET had a lower detection limit of 0.184 nM,¹⁴⁹

the lower detection limit of an electrochemical sensor with nafion-graphene reached 0.003 nM.¹⁵⁰ A rGO-FET sensor got the detection limit of 0.02 nM.¹⁰⁹ These achievements are listed in Table 2.1. However, besides the lower detection limit, response time and portability need to be addressed. Compared with other sensors, our graphene-based FET sensor can provide the detection result in a few seconds instead of tens of minutes or even longer, which makes the real-time detection feasible. At present, we are aiming at the sensitive detection of target ions, and the sensor is for one-time use only. The sensing device can be reused for 3 times with the rinse of acidic buffer (pH=2.8), and no significant degradation in the sensitivity was observed. As reported previously, this type of hybrid sensors has great potential for reuse if a proper method can be identified to detach target ions from the probes.^{51,151} For real applications of the rGO/GSH-Au NP hybrid sensor, it is necessary to further investigate the reusability and the stability.

Table 2.1 The lower detection limit achieved by different methods measuring lead ions in water.

Methods	Structure & Materials	Lower Detection Limit (nM)
Colorimetric sensor	GSH-Au NPs	100 ^{137, 152}
Fluorescent sensor	DNAzyme	10 ¹⁴⁸
	GO/aptamer QD	0.09 ¹⁴³
Electrochemical sensor	SnO ₂ /rGO	0.184 ¹⁴⁹
	Nafion-graphene	0.003 ^{150, 153}
Electronic sensor	rGO-FET	0.02 ¹⁰⁹
	rGO/GSH-Au NP	10

2.4 Summary and conclusion

In summary, a real-time, sensitive, specific, user-friendly, portable, and low-cost sensor, using an rGO/GSH-Au NP hybrid structure, has been developed for the detection of Pb^{2+} . The detection is enabled by recording the electrical conductance of the device through monitoring the change in the drain current of the rGO sheets decorated with GSH functionalized Au-NPs. The monolayer GO sheets were selectively deposited onto the electrodes by a self-assembly method and were thermally annealed to enhance their contact with the Au electrode. The experimental results show that Pb^{2+} can be detected quickly (1–2 s) and sensitively with a lower detection limit of 10 nM. The sensor is also selective against other metal ions. The platform offers a promising route for real-time, high performance, and low-cost detection of various chemicals and bacteria in an aqueous environment.

CHAPTER 3 ULTRASENSITIVE MERCURY ION DETECTION USING DNA-FUNCTIONALIZED MOLYBDENUM DISULFIDE NANOSHEET/GOLD NANOPARTICLE HYBRID FIELD-EFFECT TRANSISTOR *³

3.1 Introduction

Mercury, one of the most harmful pollutants in water, has a significant negative impact on human health. The MoS₂ nanosheet, due to its unique electronic properties, is a promising candidate for high performance sensing materials. Here, we report an MoS₂/DNA-Au NPs hybrid FET sensor for the ultrasensitive detection of Hg²⁺ ions in an aqueous environment. In section 3.2, the device fabrication is introduced; MoS₂ flakes are prepared as a thin film with a filtration method and then transferred on the sensor substrate. Specific DNA is used in the hybrid structure as the capturing probe for the Hg²⁺ ion detection. In Section 3.3, AFM and Resonance Raman (RR) spectroscopy are used to characterize the thickness and the phase of the prepared MoS₂ film, respectively. Sensing performance of the MoS₂/DNA-Au NPs to Hg²⁺ is discussed. Exponential fitting of sensitivity as a function of Hg²⁺ concentration for the hybrid sensor suggests that the high sensitivity for future sensors can be realized by enhancing the electronic properties of conducting channel materials and coating with the maximum number of probes.

*³This chapter has been published.

3.2 Experimental methods

3.2.1 Materials

MoS₂ nanosheets were synthesized by a lithium ion exfoliation method at room temperature, primarily due to its capability to control the nanosheet thickness and its potential for low-cost industrial applications,^{88, 154-156} compared with the mechanical exfoliation method.^{91, 157-159} Here the MoS₂ powder was intercalated by Li ions and then sonicated in water. Next, MoS₂ crystals were immersed in a butyllithium solution for 7 days in a flask filled with argon gas. The Li_xMoS₂ was retrieved by centrifugation and washed with hexane to remove excess lithium and organic residues. Exfoliation was achieved immediately after this by ultrasonically dispersing Li_xMoS₂ in water for 1 h. Later, MoS₂ film was prepared by filtering a diluted suspension (0.2 mg mL⁻¹) through a mixed cellulose ester membrane with 25 nm pores. The MoS₂ film was delaminated and transferred onto the SiO₂ substrate, as shown in Figure 3.1.

All metal ion solutions, including As(V), Ca²⁺, Cd²⁺, Cu²⁺, Hg²⁺, Fe³⁺, Mg²⁺, Na⁺, Pb²⁺ and Zn²⁺, were prepared by adding chloride salts (Sigma-Aldrich) in DI water (Cellgro). MoS₂ powder (particle size: <2 μm) was purchased from Sigma-Aldrich. DNA (5'-SH-TCA TGT TTG TTT GTT GGC CCCCCT TCT TTC TTA-3') was purchased from Integrated DNA Technologies (IDT). Phosphate buffer solution (PBS) (pH=7.4, ×1) (Fisher BioReagents) was used as the solvent for the DNA. Au NPs were obtained through sputtering with an RF (60 Hz) Emitech K550x sputter coater apparatus using an Au target. The assay of Hg²⁺ in experimental samples was characterized using an ICP method. The ICP analysis result was 20% higher than the prepared concentration of the experimental samples (the pH of experimental samples ranges

from 7.74 to 6.40, with the concentration of sample increasing from 0.1 nM to 10 μ M, respectively).

3.2.2 Device Fabrication:

The sensor electrode was fabricated on a Si/SiO₂ chip with a similar method used in our previous studies.¹⁶⁰⁻¹⁶² The interdigitated Au electrodes have a finger width and spacing of 2 μ m. To bridge the interdigitated electrode gaps, the MoS₂ dispersion was filtered to form a film, as shown in Figure 3.1, and then delaminated and transferred onto the active electrode area through a physical contact. Thermal annealing was used to enhance the contact and carried out in a tube furnace (Lindberg Blue, TF55035A-1). In the process, Au electrodes with the attached MoS₂ film and the Si substrate were heated for 1 h at 250 °C in an Ar and H₂ flow (0.4 L/min and 0.1 L/min). After heating, samples were cooled down to room temperature. Au NPs were deposited onto the surface of the MoS₂ film using an RF (60 Hz) Emitech K550x Sputter coater apparatus with an Au target (99.999% purity) at an Ar pressure of 0.03 mbar. Au NPs of 2 nm were sputtered and attached on the MoS₂ film. Then, 10 μ L of 100 μ M DNA solution in \times 1 PBS was injected onto the active area of the device, and incubated for 60 min at room temperature. Finally, the device was briefly rinsed with DI water to eliminate the surplus DNA and dried with airflow.

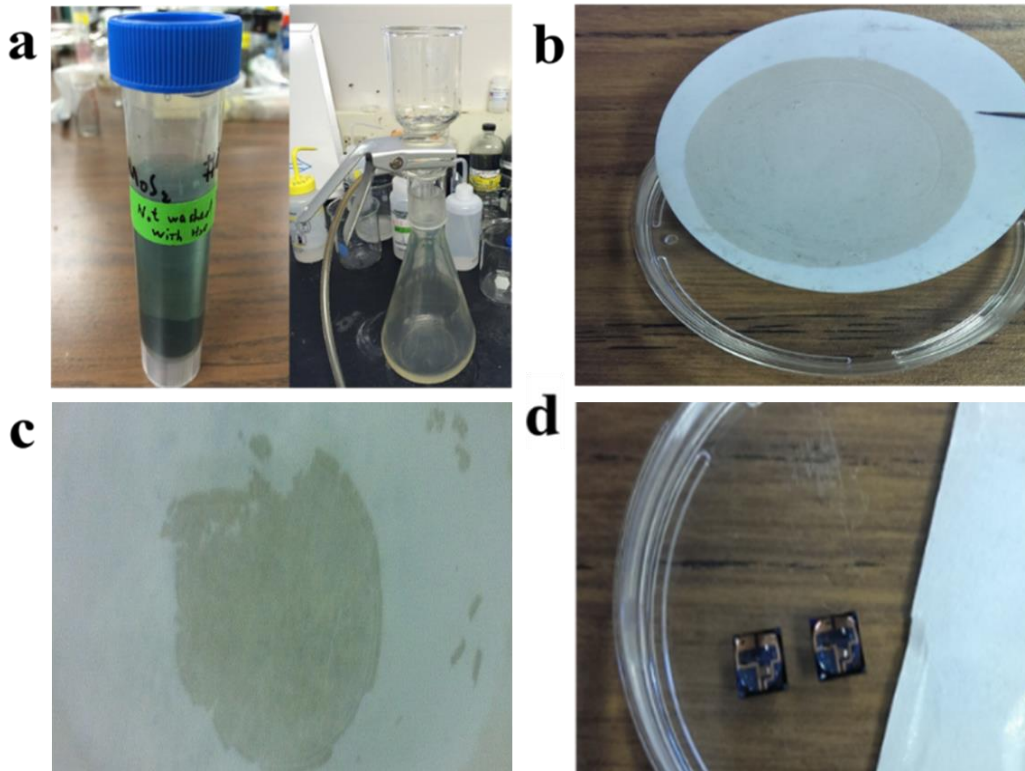


Figure 3.1 MoS₂ membrane preparation and transfer process. (a-b), MoS₂ film was prepared by filtering a diluted MoS₂ suspension through a mixed cellulose ester membrane with 25 nm pores. (c-d), the MoS₂ film was delaminated and transferred onto the Si/SiO₂ substrate.

3.2.3 Characterization:

A Hitachi S4800 field-emission SEM was used to characterize the morphology of the MoS₂ film at a 5-kV acceleration voltage. Raman spectrum, using a Raman spectrometer (Renishaw 1000B) with 633 nm laser excitation, was used to investigate the phase of the pure MoS₂ nanosheet. Meanwhile, the average MoS₂ film thicknesses were measured with AFM (Park Systems, NX10). The nanostructure of the synthesized MoS₂ nanosheet was characterized by TEM and HRTEM (Hitachi H-9000-NAR).

3.2.4 Sensing test:

A Keithley 4200 semiconductor characterization system was employed to investigate the electrical characteristics and sensing performance of the FET device at room temperature. The

transistor measurement on the sensor was carried out by measuring the drain current (I_{ds}) as a function of the gate voltage (V_g) (-40 V to +40 V) with a fixed source-drain voltage ($V_{ds}=0.1V$). The sensing signal of the device was recorded by monitoring the electrical current of the MoS₂/DNA-Au NPs hybrid sensor. Specifically, a fixed source-drain voltage ($V_{ds}=0.1V$) was used and the I_{ds} was recorded when the device was exposed to various concentrations of different ion solutions.

3.3 Results and discussion

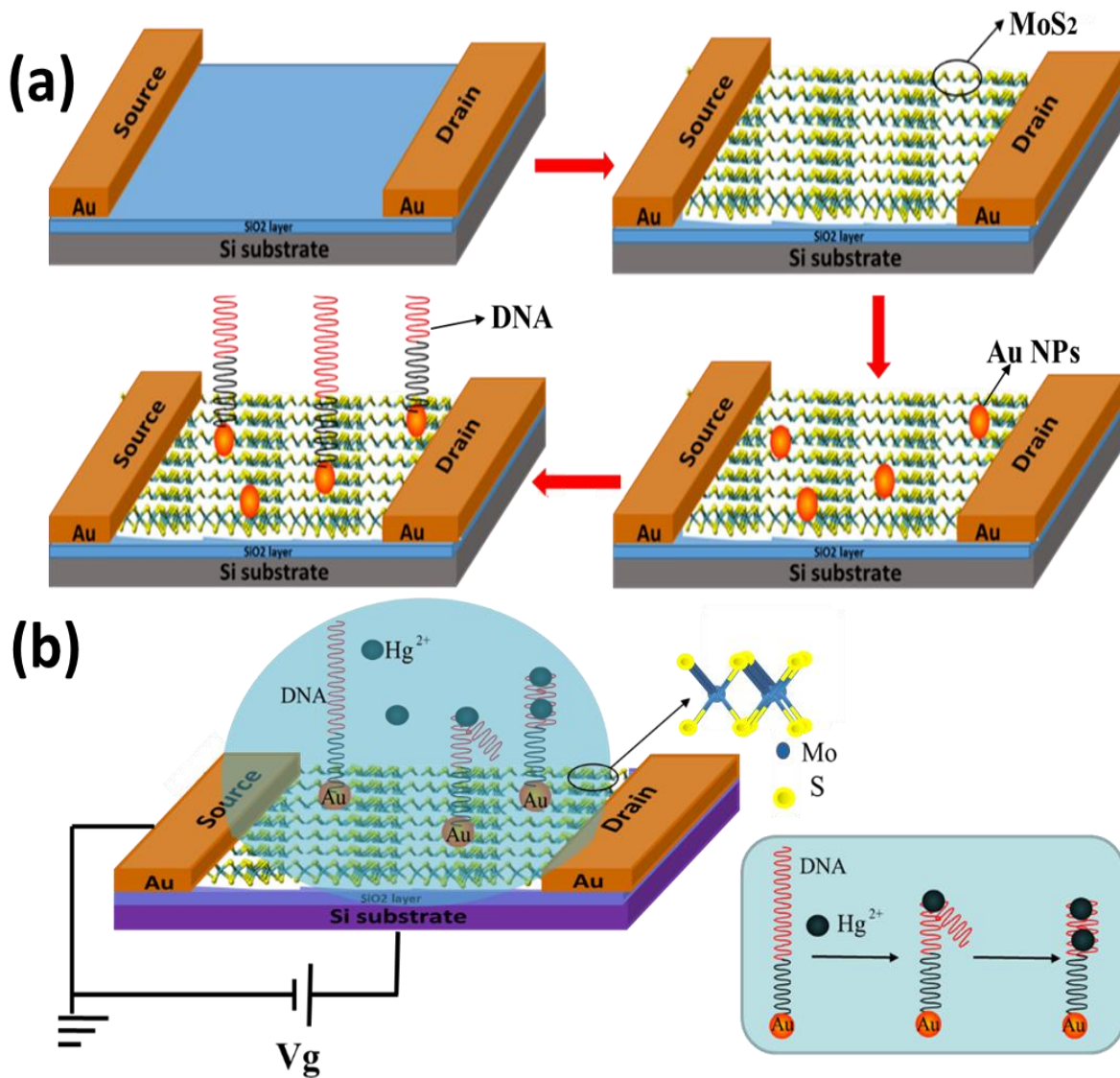


Figure 3.2 (a) Schematic diagram for the fabrication process of the MoS₂/DNA-Au NPs hybrid structure. (b) The FET sensor platform based on the hybrid structure. The formation of T-(Hg²⁺)-T chelates, through reactions between Hg²⁺ and the thymidine of the DNA molecules on the Au NPs, leading to the change in the MoS₂ electrical conductivity as a sensor signal.

Figure 3.2 (a) shows the fabrication process of our FET sensors. First, Au electrodes were patterned onto a Si substrate with a 200-nm SiO₂ top layer using a photolithographic technique. Later, the MoS₂ film was formed by filtration and transferred onto the Au electrodes, followed by thermal annealing. Then Au NPs were sputtered on the MoS₂ film, and afterward, the DNA molecules were decorated onto Au NPs by immersing the device in a DNA solution for 24 hours. The sensing signal was recorded by monitoring the electrical conductivity change of the MoS₂/DNA-Au NPs hybrid sensor. Figure 3.2 (b) schematically reveals the formation of T-(Hg²⁺)-T chelates between Hg²⁺ and the thymidine of the DNA molecules on the Au NPs, leading to the change in the MoS₂ electrical conductivity as a sensor signal. Here, every DNA strand (5'-SH-TCA TGT TTG TTT GTT GGC CCCCCT TCT TTC TTA-3') has multiple pairs of T-T on it and every T-T pair has the potential for bonding with one Hg²⁺ ion.

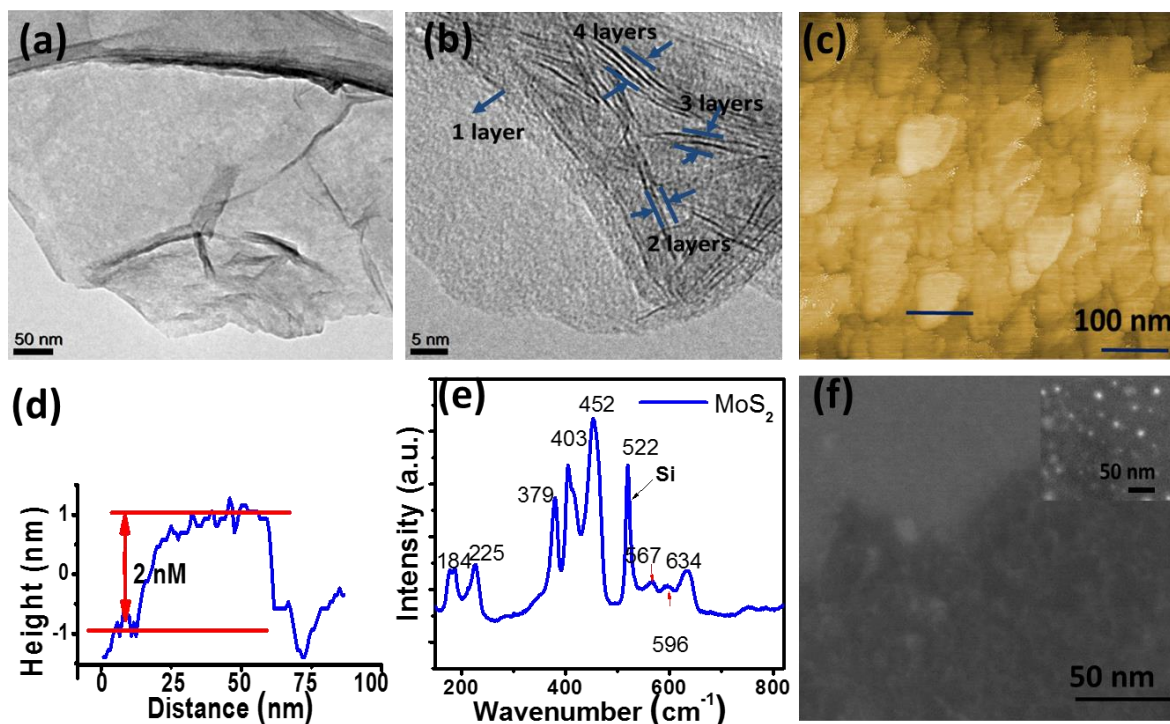


Figure 3.3 (a) TEM, (b) high resolution TEM (HRTEM), (c) AFM images, and (d) cross-sectional height profile of the exfoliated MoS₂ nanosheets, (e) RR spectrum of the exfoliated/thermally treated MoS₂ nanosheets, (f) SEM image of the prepared 2H-MoS₂ film. Insert: SEM image of the prepared MoS₂ film decorated with Au NPs.

Figure 3.3(a) shows a TEM image of an exfoliated flake suspended on a lacey carbon TEM grid, from which the exfoliated MoS₂ sheet displays laminar HRTEM image in Figure 3.3(b) clearly indicates that the exfoliated MoS₂ sheets are overlapping with each other over the entire thin flake with the layer number ranging from 1 to 4. The AFM image in Figure 3.3(c) and the height profile in Figure 3.3(d) further suggest that the thickness of the MoS₂ nanosheet is ~2 nm. Since the exfoliation by lithium intercalation results in metastable metallic (1T) phased MoS₂ (with octahedral coordination of Mo atoms) in the exfoliated individual layer,¹⁶³ the thermal annealing was conducted at 250 °C for 1 h in Ar to restore the MoS₂ from 1T phase to the thermodynamically stable semiconducting (2H) phase (with trigonal prismatic coordination of S-Mo-S atoms) by an intercalation-assisted phase transformation. As a result, the

corresponding RR spectrum of the as-fabricated/treated MoS₂ sheet in Figure 3.3(e) displays several peaks, consistent with those of the 2H-MoS₂ reported by previous studies.⁸⁸ Figure 3.3(f) and its inset show the SEM images of the prepared 2H-MoS₂ film before and after the decoration of Au NPs, respectively. The 2H-MoS₂ film (~ 10 nm) was prepared with exfoliated MoS₂ nanosheets as a source material using a previously discussed filtering method.

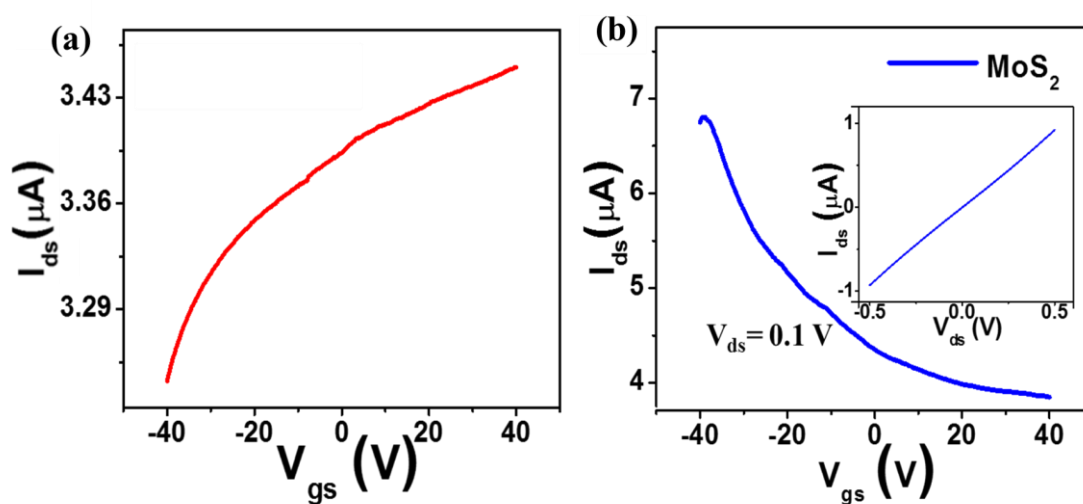


Figure 3.4 (a) I_{ds} - V_{gs} ($V_{ds} = -40$ V~40 V, step = 0.5 V) characteristics of the MoS₂/DNA-Au NPs hybrid sensor, in air at room temperature, immediately after the thermal annealing without exposure to much oxygen. (b) Room-temperature transfer characteristics of the FET sensor in air with the bias voltage V_{ds} of 0.1 V ($V_{gs} = -40$ V~40 V, step = 0.5 V). Here, the sensor had been exposed to air for over 12 hours before the FET measurement. Inset: I_{ds} - V_{ds} curve acquired for a V_{gs} value of 0 V.

The FET transfer characteristics in Figure 3.4(b) clearly indicate that the MoS₂ film in our device is p-type. Note that the p-type nature of MoS₂ in our device is opposite to the most published n-type MoS₂ grown by CVD or produced by mechanical exfoliation.⁸⁸ This is also confirmed in Figure 3.4(a) that the as-synthesized MoS₂ was n-type semiconductor. However, it was converted to p-type semiconductor when exposed to the oxygen-containing atmosphere, as oxygen molecules adsorbed onto defects or sulfur sites on the top layer of the MoS₂ film

work as p-type dopants for the MoS₂ surface by trapping electrons. The linear relationship of the I-V curve in the inset of Figure 3.4 (b) suggests an Ohmic contact between the MoS₂ film and the Au electrodes.¹⁶⁴ This can be expected because the work function of the MoS₂ film (5.23 eV) is smaller than that of Au electrode (5.26 eV)¹⁶⁵ and the band edges would be upwards bent upon contact as indicated in Figure 3.5.

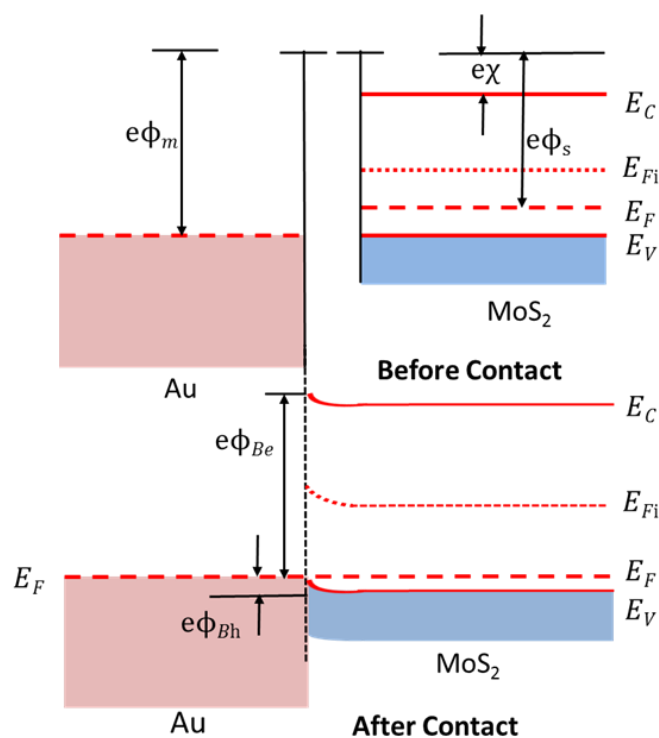


Figure 3.5 Schematics of band alignment between the MoS₂ film and the Au electrode before and after contact.

For the sensing test, we fabricated three types of sensors: the bare MoS₂ film, the MoS₂ film decorated with Au-NPs only, and the MoS₂ film decorated with the DNA probe modified Au-NPs. The Au NPs here were used as anchoring sites to immobilize probes,¹⁶⁶ because thiolate groups of the molecules can easily attach to the Au NPs, which allows the incorporation of a wide range of molecules onto Au NP surfaces.¹³⁴ Figure 3.6(a) shows the output characteristics (the I_{ds}-V_{ds} curves) of these three types of sensors. A decreased drain current

was observed after the deposition of Au NPs on the MoS₂ film. Because of the work function difference between the Au NPs (3.6 eV in air for D=8 nm)¹⁶⁷ and the MoS₂ film (~5.23 eV after annealing),¹⁶⁸ electron transfer occurs from the Au NPs to the MoS₂ film, leading to a decreased concentration of holes in the MoS₂ film and thus the decreased conductivity. After the assembly of negatively charged DNA molecules (as the phosphate groups in the DNA backbone carry negatively-charged oxygen) onto Au NPs, the drain current further decreases, likely because the DNA was negatively charged and electrons transfer from DNA to Au NPs and then from Au NPs to MoS₂, resulting in a decreased hole concentration in the MoS₂ film.

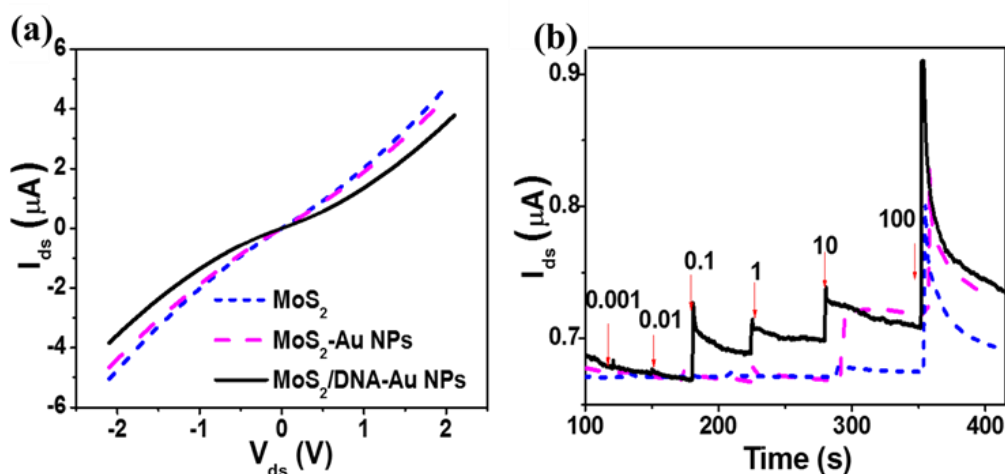


Figure 3.6 (a) Evolution of the I_{ds} - V_{ds} characteristics during the MoS₂/DNA-Au NPs hybrid sensor fabrication process ($V_{ds} = -2.1$ V~2.1 V, step = 0.1 V) at room temperature. (b) Real-time detections of Hg²⁺ (nM) in water ($V_{ds} = 0.1$ V) with platforms of MoS₂/DNA-Au NPs (black, solid), MoS₂-Au NPs (purple, dash), MoS₂ (blue, short dash), respectively.

Figure 3.6(b) presents the dynamic responses of our as-fabricated devices by monitoring the drain current versus time during a cumulative addition of Hg²⁺ solution to the sensor. We can see that the MoS₂/DNA-Au NPs hybrid structure is sensitive to Hg²⁺ with the detection

limit lowered to 0.1 nM (defined as the concentration corresponding with a signal-to-noise ratio of approximately 3¹⁶⁹). This is two orders of magnitude lower than the MCL of Hg²⁺ (9.9 nM) in drinking water defined by the EPA,⁴ and is superior to most of detection limits reported for standard/current methods as summarized in Table 3.1. For example, the Hg²⁺ detection limit is 0.25 nM from the cold vapor ICP-MS method,¹⁷⁰ while it is down to 0.0299 nM by the graphene/Au NPs-based electrochemical sensors.¹⁷¹ For the FET sensors, the detection limit is tremendously improved from 25 nM of the rGO/TGA-Au NPs hybrid structure-based sensor¹⁶¹ to 0.03 nM¹⁷² for the few-layer MoS₂-based sensor.

Table 3.1 Comparison of LOD and calibrated range among different methods for Hg²⁺ detection.

Methods	Standard techniques			Electrochemical sensors		FET sensors		
	Ion-selective PVC-ME ¹⁷³	Reversed-phase-LC ¹⁷⁴	Cold vapour ICP-MS method ¹⁷⁰	Au-NP-G ¹⁷¹	SnO ₂ /rGO NCs ¹⁷⁵	MoS ₂ ¹⁷²	rGO/TGA-Au NP ¹⁶¹	This work
LOD (nM)	1,000	100	0.025	0.0299	0.279	0.03	25	0.1
Calibrated range (nM)	1.8×10 ³ -1.0×10 ⁸	1.0×10 ² -5.0×10 ⁴	0.25-5	0.04-0.25&0.5-3.0×10 ²	4.0×10 ² -1.2×10 ³	/	/	0.1-10

* The MCL of Hg²⁺ is 9.97 nM.

The great improvement of the selectivity after the DNA probe decoration on the Au surface suggests that the DNA probe plays an important role in the high selectivity of our sensor.¹⁷² This is mainly due to the strong interaction between the Hg²⁺ and the single-stranded Hg²⁺ dependent DNA probes immobilized on the Au surface through Au-S bonds,¹⁷⁶ since DNA binds with Hg²⁺ by virtue of a series of thymine-thymine mismatches upon exposure to Hg²⁺,

as illustrated in Figure 3.1(b). As the metal ions bind to the DNA probes, the accumulation of the positively-charged Hg^{2+} will cause electron transfer from MoS_2 to Au NPs, resulting in a p-doping effect to MoS_2 and thus an increase of hole concentration in the MoS_2 film.¹⁴⁰ Eventually, exposure to Hg^{2+} leads to an increase of electrical conductivity in the p-type MoS_2 channel. Without specific probe, however, the signals from other metal ions in the water sample would generate nontrivial interference. Therefore, adopting specific probe is required for the highly sensitive, selective detection of Hg^{2+} . Note that the current increase might also be partially due to the higher electrical conductivity of metal ion solutions at high concentrations, especially for the bare MoS_2 film. Controlled experiments have thus been performed on a blank substrate (Figure 3.7) to study such effect quantitatively. The source-drain current changes in a blank substrate when exposed to Hg^{2+} solutions (from 0.1 nM to 100 nM) were 0.1- 0.3 nA, correspondingly. However, the current change in the $\text{MoS}_2/\text{DNA-Au}$ NPs hybrid sensor was 0.07 -0.1 μA . Thus, this remarkable current increase indeed arises from the interaction between the $\text{MoS}_2/\text{DNA-Au}$ NPs hybrid sensor and Hg^{2+} instead of the ionic conductivity introduced by Hg^{2+} . As shown in Figure 3.6(b), the pure MoS_2 film has no response to Hg^{2+} until its concentration reaches 10 nM, and a similar response was observed after Au NPs deposition, implying that there is no significant binding between MoS_2 (Au NPs) and low concentration Hg^{2+} . When the Hg^{2+} reaches a high concentration (10 nM or higher), the non-specific binding between MoS_2 , MoS_2/Au NPs and Hg^{2+} leads to an increase in the electrical conductivity. The exposure of MoS_2/Au NPs platform to high concentration Hg^{2+} results in a big conductivity increase. This can be attributed to the fact that the high concentration Hg^{2+} ions connect the gold nanoparticles (isolated but very close to each other) on the MoS_2 film.

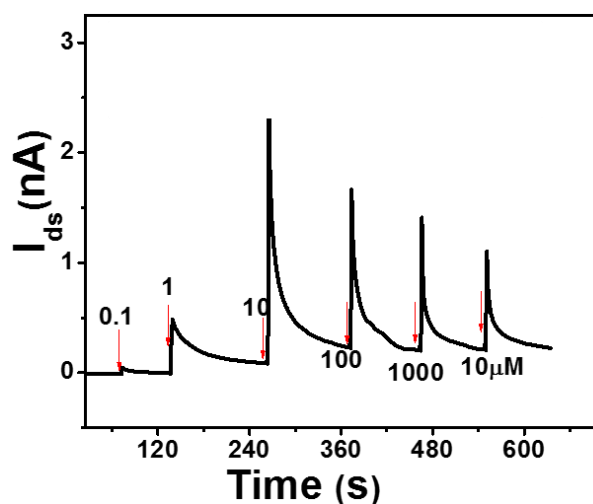


Figure 3.7 Real-time detection ($V_{ds}=0.1$ V) of Hg^{2+} in water, with concentrations ranging from 100 pM to 10 μ M, using blank Au electrode.

We now turn to explore the kinetics and the relationship between the sensitivity and the ion concentration in our device. Figure 3.8(a) shows the dynamic response of the $MoS_2/DNA-Au$ NPs hybrid sensor for lower Hg^{2+} concentrations ranging from 0.05 to 2.76 nM (here, the applied V_{ds} was 0.1 V). We can see that no noticeable change occurs upon the addition of DI water and lower concentrations of Hg^{2+} than 0.1 nM. Therefore, compared with the DI water, the increase in the electrical conductance of the MoS_2 FET device indeed results from its exposure to Hg^{2+} . Practically, the current begins to increase only after the ions in the liquid drop diffuse from the top of the device into the active area. The dynamic responses in Figure 3.8(a) indicate that our sensor responded to the Hg^{2+} within a few seconds and this response rate is much faster than the conventional atomic fluorescence ones, which take minutes or even longer, to have the dispersed Hg^{2+} fully trapped by the instrument to enable detection.^{160, 177}

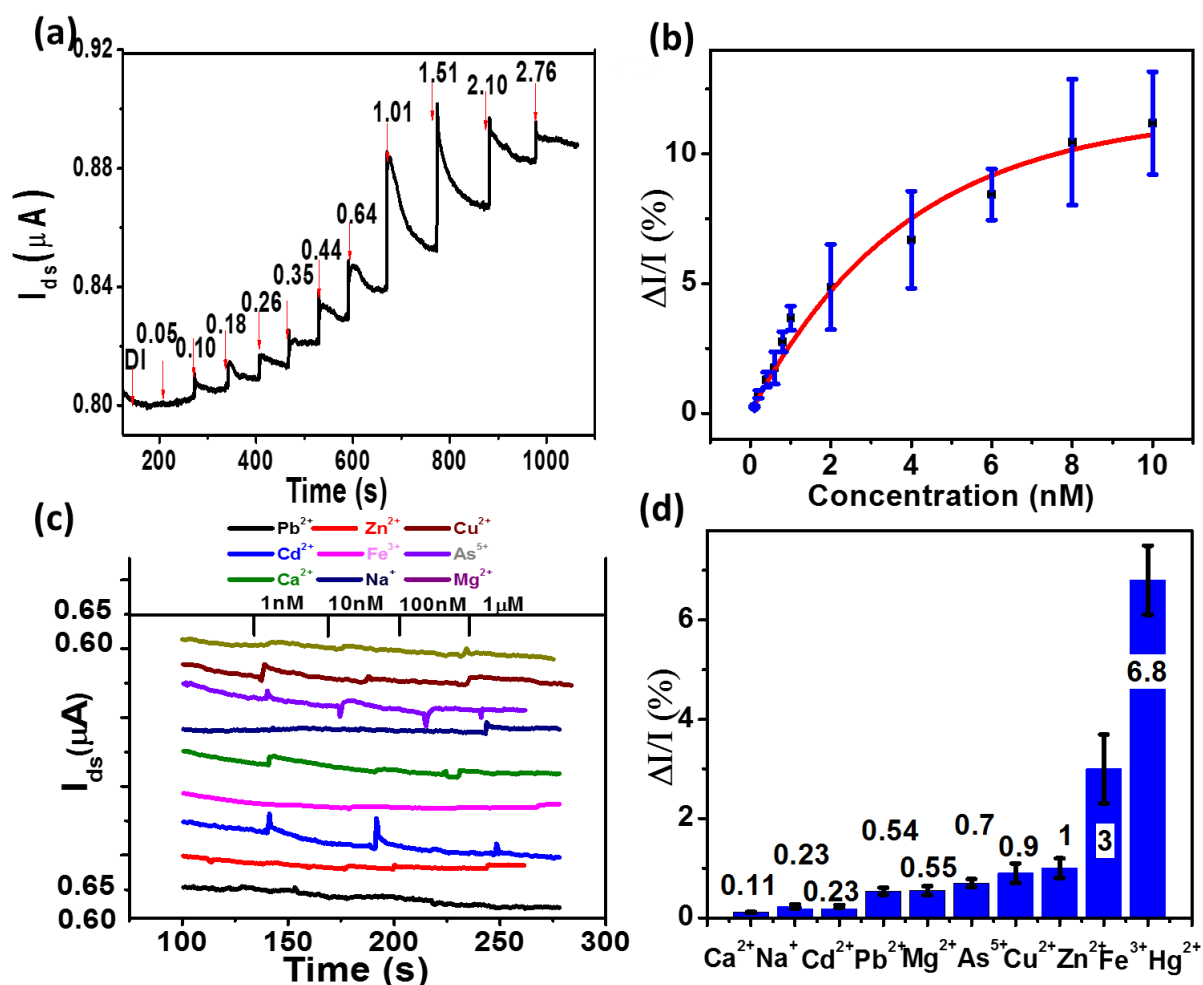


Figure 3.8 (a) Real-time detection of Hg^{2+} in water using the $\text{MoS}_2/\text{DNA-Au NPs}$ hybrid sensor ($V_{ds}=0.1\text{ V}$) with a lower detection limit of 0.1 nM ($0.02\text{ }\mu\text{g/L}$). (b) Sensitivity variation and exponential fitting of sensitivity using Eq. (3.1) as a function of Hg^{2+} concentration for the $\text{MoS}_2/\text{DNA-Au NPs}$ hybrid sensor. (c) Real-time detection of various interfering ions in water with the $\text{MoS}_2/\text{DNA-Au NPs}$ hybrid sensor. ($V_{ds}=0.1\text{ V}$) (d) Relative current change of an $\text{MoS}_2/\text{DNA-Au NP}$ hybrid sensor in response to various heavy metal ions: As(V) , Ca^{2+} , Cd^{2+} , Cu^{2+} , Fe^{3+} , Hg^{2+} , Mg^{2+} , Na^+ , Pb^{2+} and Zn^{2+} (1 nM).

In principle, the conductance of our $\text{MoS}_2/\text{DNA-Au NPs}$ sensor increases gradually with the cumulative addition of the Hg^{2+} solution. The rate of increase in the conductance or source-drain current) is dependent on the Hg^{2+} concentration. Moreover, this rate should gradually decrease to zero (or the sensitivity should gradually increase and eventually saturate) as the

Hg^{2+} concentration increases, because the attracting sites in the DNA probes become fewer and fewer. The relationship between the sensitivity and the Hg^{2+} concentration can be described as

$$S = A[1 - \exp(-Bx)], \quad (3.1)$$

in which A and B are the fitting parameters, and x is the ion concentration. For our $\text{MoS}_2/\text{DNA-Au}$ NPs hybrid sensor shown in Figure 3.8(b), A and B are fitted to be 11.6 and 0.26/nM, respectively. Note that A and B are intrinsic to the conducting channel materials and DNA probes. And the magnitude of the sensitivity (A) is dictated by the properties of conducting channel materials (it will be discussed in Section 5.3), while its rate of increase (B) is determined by the type of DNA probe and its concentration. Eqn. (3.1) thus suggests that the high sensitivity for future sensors can be realized by enhancing properties of conducting channel materials and coated with the maximum number of specific DNA probes.

To determine the selectivity of our hybrid sensor, the detection of nine other metal ions was also carried out, such as As(V) , Ca^{2+} , Cd^{2+} , Cu^{2+} , Fe^{3+} , Mg^{2+} , Na^+ , Pb^{2+} and Zn^{2+} . Figure 3.8(c) presents the dynamic responses towards these ions with several selected concentrations (1 nM, 10 nM, 100 nM, 1 μM), while the sensitivities of the $\text{MoS}_2/\text{DNA-Au}$ NPs hybrid sensor at the concentration of 1 nM are plotted in Figure 3.8(d). We can see that Cd^{2+} , Fe^{3+} and Pb^{2+} could lead to the current increases at the concentration of 100 nM, 100 nM and 1 μM due to the increased hole concentration in the MoS_2 film, respectively, but the sensitivities are much smaller compared with the significant responses to Hg^{2+} . However, the hybrid sensor did not show obvious responses to As(V) , Ca^{2+} , Cu^{2+} , Mg^{2+} , Na^+ and Zn^{2+} . These results indicate the high selectivity of the hybrid structure to Hg^{2+} . To verify the stability and repeatability of our

sensor devices, each sensing operation was repeated 3 times, with concentrations ranging from 1 pM to 100 nM, and they showed similar responses, as indicated in Figure 3.9.

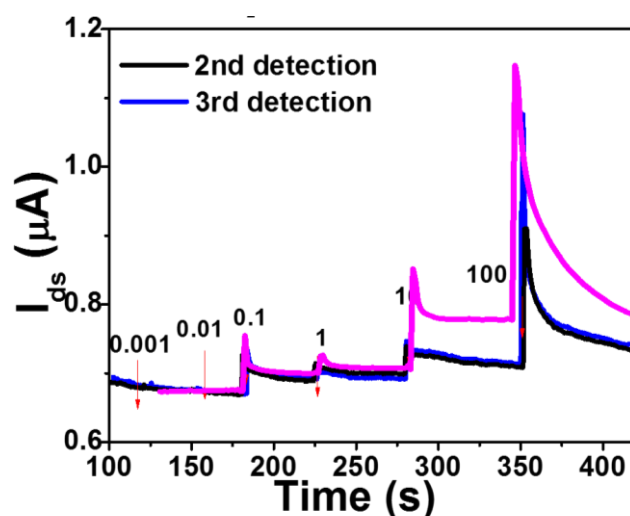


Figure 3.9 Repeatability of the MoS₂/DNA-Au NPs hybrid sensor, confirmed by similar dynamic responses of three different sensors to Hg²⁺, with concentrations ranging from 1 pM to 100 nM.

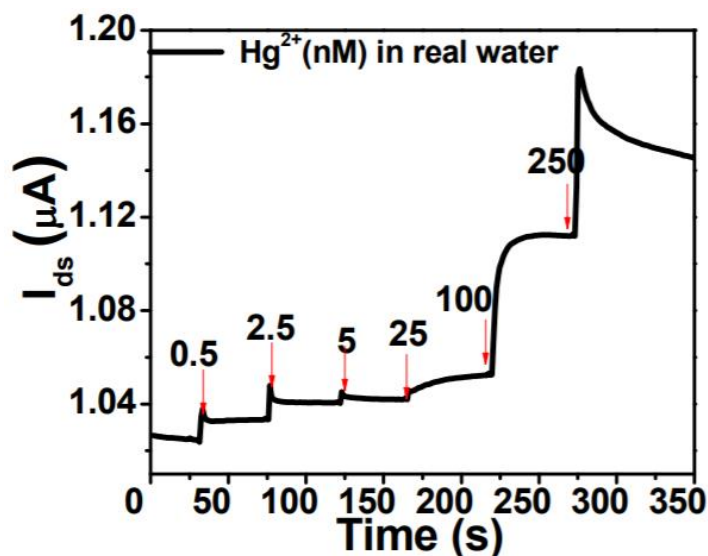


Figure 3.10 Real-time detection ($V_{ds}=0.1$ V) of Hg²⁺ in real water samples (provided by our industrial partner) with concentrations ranging from 0.5 nM to 250 nM using the MoS₂/DNA-Au NPs hybrid sensor.

We also investigated its sensing performance for Hg²⁺ in real water samples that were provided by our industrial partner. The result is shown in Figure 3.10; the dynamic signal

introduced by the Hg^{2+} in water with concentrations ranging from 0.5 nM to 250 nM clearly suggests the rapid and sensitive detection for Hg^{2+} . At present, the sensor is for one-time use only, but great potential for reuse has been indicated in experiments with proper methods to detach target ions from the probes.^{160, 151} In our experiments, the sensing device can be reused for 3 times by rinsing the device with acidic buffer (pH = 2.8), and no significant degradation in the sensitivity was observed (degradation is shown in Figure 3.11). However, to extend the $\text{MoS}_2/\text{DNA-Au NPs}$ hybrid sensor into practical reusable applications, further work is needed.

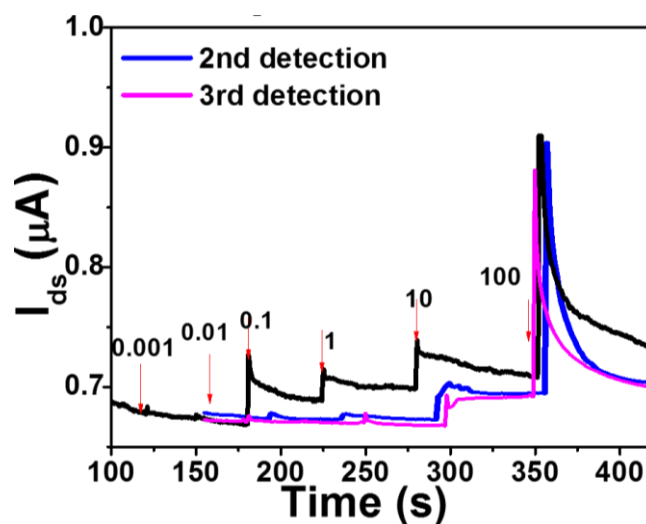


Figure 3.11 Reusability of the $\text{MoS}_2/\text{DNA-Au NPs}$ hybrid sensor, suggesting no significant degradation in the sensitivity was observed in dynamic responses of the same sensor to Hg^{2+} for three continuous uses after washing.

3.4 Summary and conclusion

In summary, we demonstrated a sensitive and selective $\text{MoS}_2/\text{DNA-Au NPs}$ hybrid structure-based FET sensor for Hg^{2+} detection. In the hybrid structure, the MoS_2 thin film acts as the conducting channel with the homogeneously dispersed Au NPs as anchoring sites for DNA probes specific to detection of Hg^{2+} . The detection is enabled by monitoring the change

of the source-drain current in the FET device as a function of Hg^{2+} concentration. Our sensor offers a promising route for the real-time (1–2 s), high-performance, and low-cost detection of Hg^{2+} . The detection limit can reach down to the concentration of 0.1 nM. Meanwhile, the sensor also shows high selectivity against many other metal ions. Overall, the simple fabrication procedure and the excellent sensing performance of the $\text{MoS}_2/\text{DNA-Au}$ NPs hybrid structure makes it a promising for real-time detection of Hg^{2+} in an aqueous environment.

CHAPTER 4 REAL-TIME AND SENSITIVE ARSENIC ION DETECTION USING BLACK PHOSPHORUS/AU NP/DTT HYBRID STRUCTURE *4

4.1 Introduction

BP nanosheet, due to its unique structure and excellent electronic properties, becomes a promising candidate for high-performance sensing material in an FET sensor. Arsenic is one of the most abundant mineral in the earth. The toxicity of As is notorious and drinking water with arsenic can lead to various diseases. Here, we report an FET sensor using hybrid structure of BP and dithiothreitol (DTT)-functionalized Au NPs for the detection of As in water. In Section 4.2, we will discuss the BP thin film preparation through the mechanical exfoliation method. Section 4.3 demonstrates the outstanding performance of the as-fabricated BP/Au NPs/DTT sensor. A logarithmic curve and a linear curve are used to fit the sensitivity as functions of As ions concentration for the BP/Au NPs/DTT hybrid sensor, respectively, and the fitting curve is used for the prediction of As ion concentration in lake water, as discussed in Section 4.4.

4.2 Experimental methods

4.2.1 Sensor fabrication and characterization:

The interdigitated Au electrodes (spacing of 2 μm) were thermally deposited on the SiO_2 (thickness of 300 nm)/Si (thickness of 500 μm) substrate using a laser direct writing method.

*4This chapter has been published.

The BP film was exfoliated from the commercial bulk BP (purchased from HQ Graphene) using the “Scotch tape” method, as shown in Figure 4.1 (a). Then the exfoliated BP film was transferred onto the Au electrodes as in Figure 4.1 (b), bridging the gap between the two electrodes. To enhance the contact quality between the BP film and Au electrodes, the sensor was thermally annealed at 250 °C in Argon atmosphere for 30 mins. And Au NPs were sputter coated on the BP film. SEM (Hitachi S4800) was used to characterize the morphology of the BP film at a 2-kV acceleration voltage, while AFM (Park Systems, NX10) was employed to identify the thickness of the exfoliated BP film. TEM and HRTEM (Hitachi H-9000-NAR) were used to characterize the nanostructure of the prepared BP nanosheet. Afterwards, Au NPs were sputter coated with an RF Emitech K550x using an Au target.

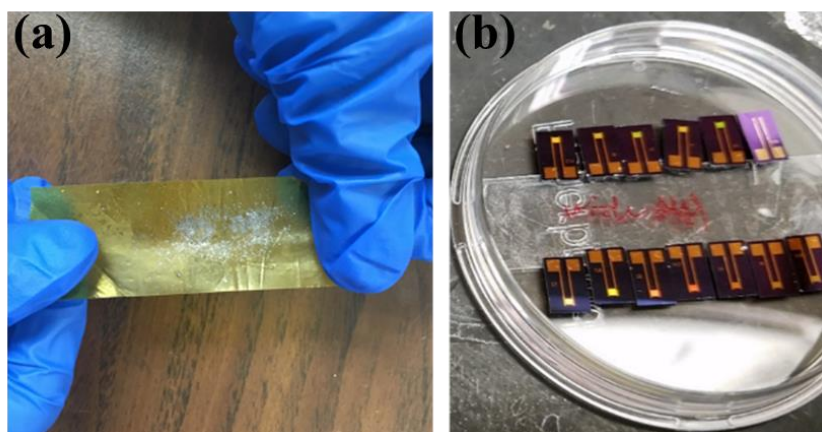


Figure 4.1 (a) Mechanical exfoliation of the BP film using the “Scotch tape” method. (b) The exfoliated BP film was transferred onto the Au electrodes.

4.2.2 Sensing test:

All sensing tests were performed under the ambient condition. A Keithley 4200 semiconductor characterization system was used to characterize the sensor platform. The electrical conductance of the sensor was recorded by monitoring the change in the drain current (I_{ds}) for a fixed source–drain voltage (V_{ds}) when the sensor was exposed to different

concentrations of target solutions. Between the source and drain electrodes, a constant voltage (0.1 V) was applied to the sensor and the electrical conductance difference was monitored and recorded. In the control experiments of selectivity, Ag^+ , Ca^{2+} , Cd^{2+} , Cu^{2+} , Fe^{3+} , Hg^{2+} , Mg^{2+} , Na^+ , Pb^{2+} and Zn^{2+} solutions were prepared with corresponding metal chloride salts in ultrapure water, and phosphate ion solutions were prepared with NaH_2PO_4 . Ethylenediaminetetraacetic acid (EDTA) was added as chelating agent for diminishing the reactivity of metal cations, especially Mn^{2+} .¹⁴ As (V) solutions were prepared with NaH_2AsO_4 . All the salts, EDTA and humic acid were purchased from Sigma Aldrich. The As (III) solutions were prepared by diluting Arsenic +3 ICP standard (VWR) with ultrapure water. The ICP-MS was employed to characterize the assay of the As ions in our experiments. In this research work, for the As (III) solutions with concentrations ranging from 1nM to 1 μ M, their pH values varied from 5.92 to 5.30. As reported, in this pH range, H_3AsO_3 ($\text{As}(\text{OH})_3$) is dominant;¹⁷⁸ thus only $\text{As}(\text{OH})_3$ was considered for schematic representation. Acidities were tested with a pH meter (Hanna Instruments HI98103).

4.3 Results and discussion

Figure 4.2 (a) presents a schematic of the BP/Au NPs/DTT sensing platform. BP film was mechanically exfoliated and transferred onto the Si wafer with patterned Au electrodes. Attributing to the bonding between Au NPs and thiolated groups on DTT molecules, Au NPs act as the anchoring sites to immobilize the chemical probes DTT through Au-S bonds,¹⁷⁹⁻¹⁸¹ which improves the specificity of the sensing platform. The DTT structure is shown in Figure 4.2 (b) with two thiol groups on both ends, with one end attaching to the Au NPs, and the other

end free.¹⁸²⁻¹⁸³ It is well known that As (III) has a very high affinity for thiol-containing ligands.¹⁸⁴⁻¹⁸⁶ During the sensing process, the free end thiol group will chelate with As (III) through forming covalent bonding and generates strong complex.¹⁸⁶ As shown in schematic Figure 4.2 (b), each As (III) ion can bind with three DTT-conjugated Au NPs through an As-S linkage.^{185, 187} Since the As (III) species are negatively charged, they would cause the electrons to transfer to BP film, leading to the electrical conductivity change in the BP film.

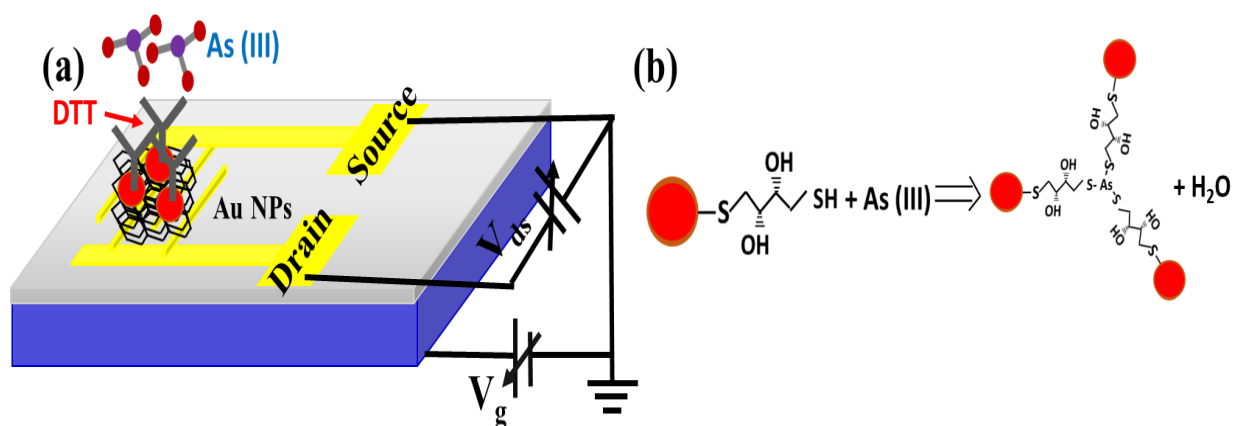


Figure 4.2 (a) Schematic of the BP/Au NPs/DTT sensing platform for the As ion detection. (b) The reaction between the DTT and As (III) ion in the detection process.

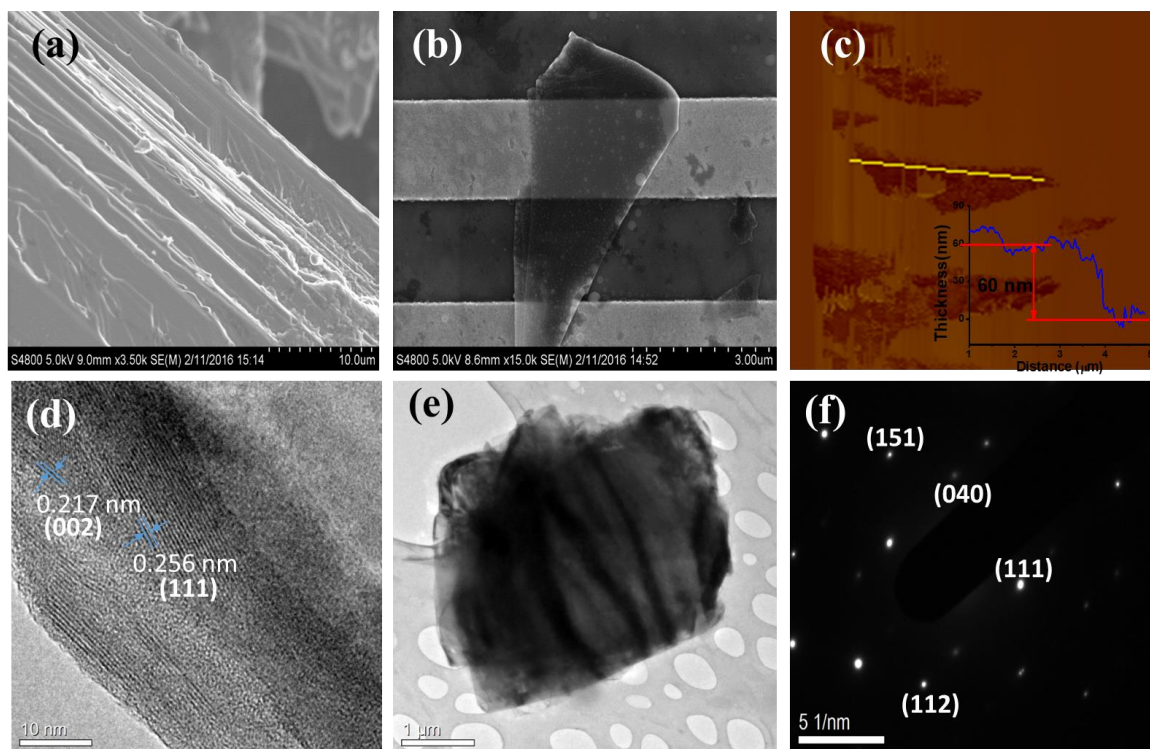


Figure 4.3 SEM images of (a) bulk BP with the layered structure, (b) an exfoliated BP flake electrically bridging the interdigitated Au electrodes. (c) AFM image of exfoliated BP flakes and, inset: the height profile across the flakes. (d) HRTEM image of a BP film, demonstrating the typical BP lattice spacing. (e) TEM image and (f) SAED pattern of the BP film.

Figure 4.3 (a) and (b) show the SEM images of bulk BP and an exfoliated BP flake, respectively. The bulk BP exhibits a layered structure on the cross section, while the as-prepared BP flake can bridge the interdigitated electrodes, working as the channel material. The AFM image in Figure 4.3 (c) and the height profile suggest that the thickness of the BP flake in the FET sensor is ~ 60 nm, corresponding to a multilayer BP film. Thinner BP flakes were also tested for the channel material, but it did not deliver stable performance as thinner flakes can be easily oxidized in air.¹⁸⁸ Figure 4.3 (d) shows the HRTEM image of an exfoliated BP film transferred onto a holey carbon grid, while the TEM image of the bulk BP is shown in Figure 4.3 (e). The typical lattice spacings in Figure 4.3 (d) are 0.256 nm and 0.217 nm, which

correspond to the (111) and (002) planes, respectively, of the side-centered orthorhombic BP.²⁰ The selected area electron diffraction (SAED) pattern in Figure 4.3 (f) indicates a single crystalline structure. The TEM characterizations in Figure 4.3 (d-f) reveal an excellent crystalline quality of the as-produced BP film in the FET sensor.

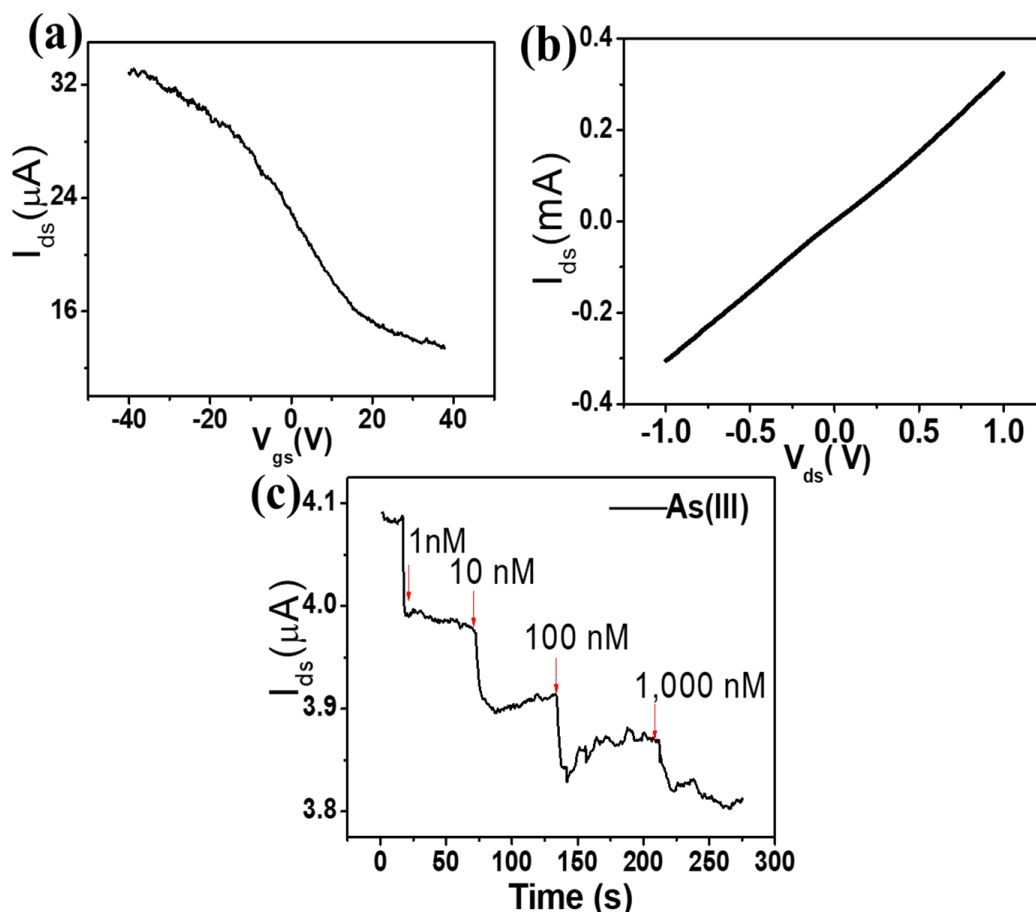


Figure 4.4 Electronic characteristics and real-time sensing performance of the FET sensor platform (a) I_{ds} - V_{gs} curve with the bias voltage V_{gs} ranging from -40 to 40 V ($V_{ds} = 0.1$ V). (b) I_{ds} - V_{ds} curve with the $V_{ds} = -1\text{V} \sim 1\text{V}$ ($V_{gs} = 0$ V). (c) Real-time detection of As (III) in water ($V_{ds} = 0.1$ V, $V_{gs} = 0$ V) with the BP/Au NPs/DTT platform, for concentrations ranging from 1 nM to 1 μM .

Since the FET sensor works by transforming the adsorbates-induced electronic perturbation into the conductance change in the channel material, an excellent FET sensor requires both a highly sensitive response to the external stimulation and a low noise. In other words, the sensor

performance is intimately related to the electronic characteristics of the channel material itself and its contact quality with the electrodes. The investigation of the electrical characteristics was first obtained at room temperature under an ambient condition in the bottom-gated FET architecture. The I_{sd} - V_{gs} characteristic of the BP FET sensor shown in Figure 4.4 (a) exhibits a well-developed saturation curve of p-type nature with an on/off current ratio up to 3. The linear I_{sd} - V_{sd} curve in Figure 4.4 (b) implies an Ohmic-like contact between Au electrodes and the BP film, suggesting an effective carrier injection from the Au electrodes into the BP film, as well as the minimization of the potential electrical noise from the mechanical perturbation during the sensing test. Figure 4.4 (c) shows the dynamic sensing performance of the as-fabricated BP device through monitoring the drain current change versus time. Obviously, we could see that the current decreases upon the addition of As (III) solutions with all different concentrations. The As (III) solution was cumulatively drop-casted onto the sensor with the concentration ranging from 1 nM to 1 μ M. The current decrease could be attribute to the fact that when the platform is exposed to the negatively charged As (III) ions, the ions will chelate with the thiol groups on the DTT molecules, through forming covalent As-S bonding and generates strong complex, as shown in schematic Figure 4.2 (b).^{185,187} Electrons are transferred from the ions into the BP film, reducing the hole concentration in the p-type BP film and thus reducing the conductivity. Defined as the concentration corresponding with a signal to noise ratio of approximately 3, the LODs of our sensor towards As (III) is 1 nM, two orders of magnitude lower than the MCL of As in drinking water defined by both EPA and WHO (130 nM).

The prepared As (III) solution were diluted from ICP As +3 standard with ultrapure water. Their pH values varied from 5.30 (1 μ M), 5.64 (100 nM), 5.80 (10 nM) to 5.92 (1nM). It has been reported that pH increasing will lead to the As species transition, from As(OH)₃ to ultimately AsO₃³⁻.¹⁷⁸ To investigate the effect of As species on the sensing performance, another group of As (III) solutions were prepared in the same manner, followed by adjusting to neutral state (pH = 7). Figure 4.5 (a) shows the high similarity in sensing performances between the neutral As (III) solutions and the as-prepared As (III) solutions (in Figure 4.4 (c)). It may result from the intrinsic high affinity between thiol groups and As (III) ions,¹⁸⁴⁻¹⁸⁶ which is independent of the As (III) species. And the comparison confirms the consistent performance of the BP/Au NPs/DTT platform in acidic and neutral aqueous environments. The result in Figure 4.5 (b) demonstrates a comparable performance of detecting As (V) with the BP/Au NPs/DTT platform to the detection of As (III), with an LOD of 1 nM. As being reported, DTT can reduce As (V) to As (III),^{185, 189-190} thus the result in Figure 4.5 (b) implies that the BP/Au NPs/DTT sensing platform can detect As (III) as well as As (V) in water samples. Compared with the current detection methods of As (summarized in Table 4.1), the BP FET platform features both a lower LOD and a quicker response.

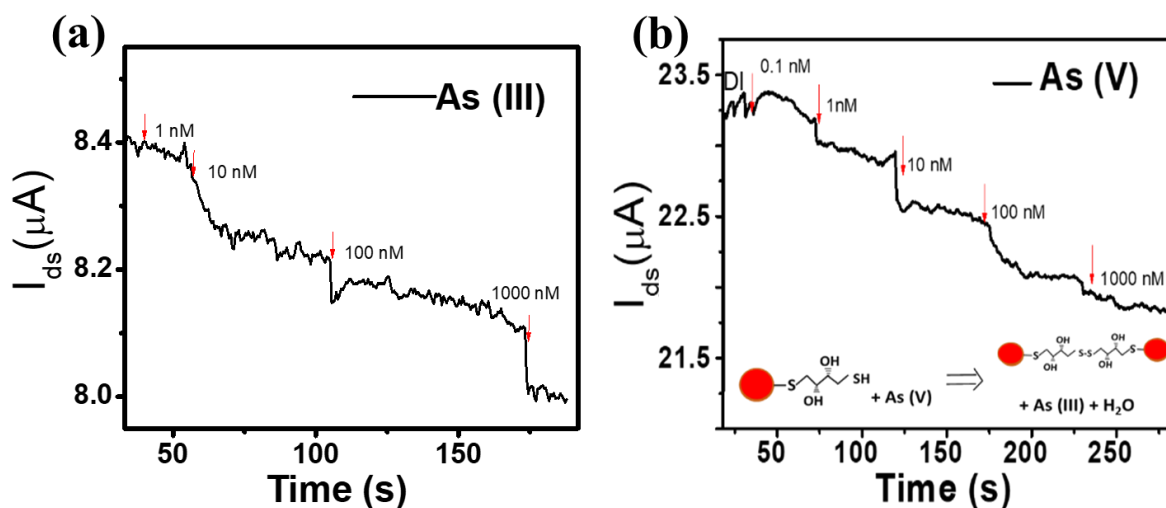


Figure 4.5 (a) Real-time detection of neutral (pH= 7) As (III) solutions in water ($V_{ds}= 0.1$ V, $V_{gs} = 0$ V) with the BP/Au NPs/DTT platform, for concentrations ranging from 1 nM to 1 μ M. (b) Real-time detection of As (V) in water ($V_{ds}= 0.1$ V, $V_{gs} = 0$ V) with the BP/Au NPs/DTT platform, for concentrations ranging from 0.1 nM to 1 μ M. Insert: the schematic of DTT reducing As (V) to As (III).

Table 4.1 Comparison of arsenic ion detection with different methods.

Methods	Structure	LOD (ppb)
Electrochemical	FePt NPs on Si ¹⁹¹	0.8
	FeAu NPs ¹⁹¹	4.1
	FePd ¹⁹¹	7.9
	Au NPs ¹⁹²	0.0096
Surface Enhanced Raman Spectroscopy	Benzenethiol-Coated Silver Nanocrystal ¹⁹³	1
Ion Selective Electrode	μ ISE/POT ¹⁹⁴	10
ICP-MS	/	As (III):0.03; As(V): 0.04 ¹⁹⁵
This work	BP/Au NPs/DTT	As (III) & As(V): 0.077

Besides functioning as the probe, adsorbed DTT molecules also work as the chemical passivation layer through the covalent functionalization between the DTT and Au NPs.¹⁹⁶ It improves the stability of the BP film by protecting it from being oxidized under the ambient condition. The good performance of the sensitivity and quick response is mainly due to the selectivity of the probe DTT to As ions. To further validate the role of probe DTT, we also designed control experiments with the bare BP film and the BP film coated with the Au NPs anchoring sites, in comparison with the BP/Au-NPs hybrid decorated with DTT probes. During the fabrication process, we can see from Figure 4.6 (a) and (b) that the current between source and drain terminals (I_{ds}) increases after the deposition of Au NPs on the BP film, indicating that the deposited Au NPs introduce a p-doping effect on BP. Because of the work function difference between the Au NPs (5.1 eV)¹⁹⁷ and BP (3.9 eV for vacuum cleaved black

phosphorus),¹⁹⁸ electron transfer occurs from BP film to Au NPs, leading to the increase of hole concentration in BP film and thus the conductivity of BP film increases. After the assembly of probe DTT, the drain current decreases, likely because the DTT was negatively charged (due to the negatively-charged thiolate -S-) and electrons will transfer to Au NPs and further to BP film. Figure 4.6 (c) shows the dynamic responses of these control group sensors to As (III) ions at different concentrations. Apparently, only the BP/Au NPs/DTT hybrid sensor exhibits significant responses and proves the necessity to use a specific probe for proper function of a sensor. The weak current decrease in BP/Au NPs platform is likely due to the non-specific attachment of As (III) ions to the Au NPs surface.

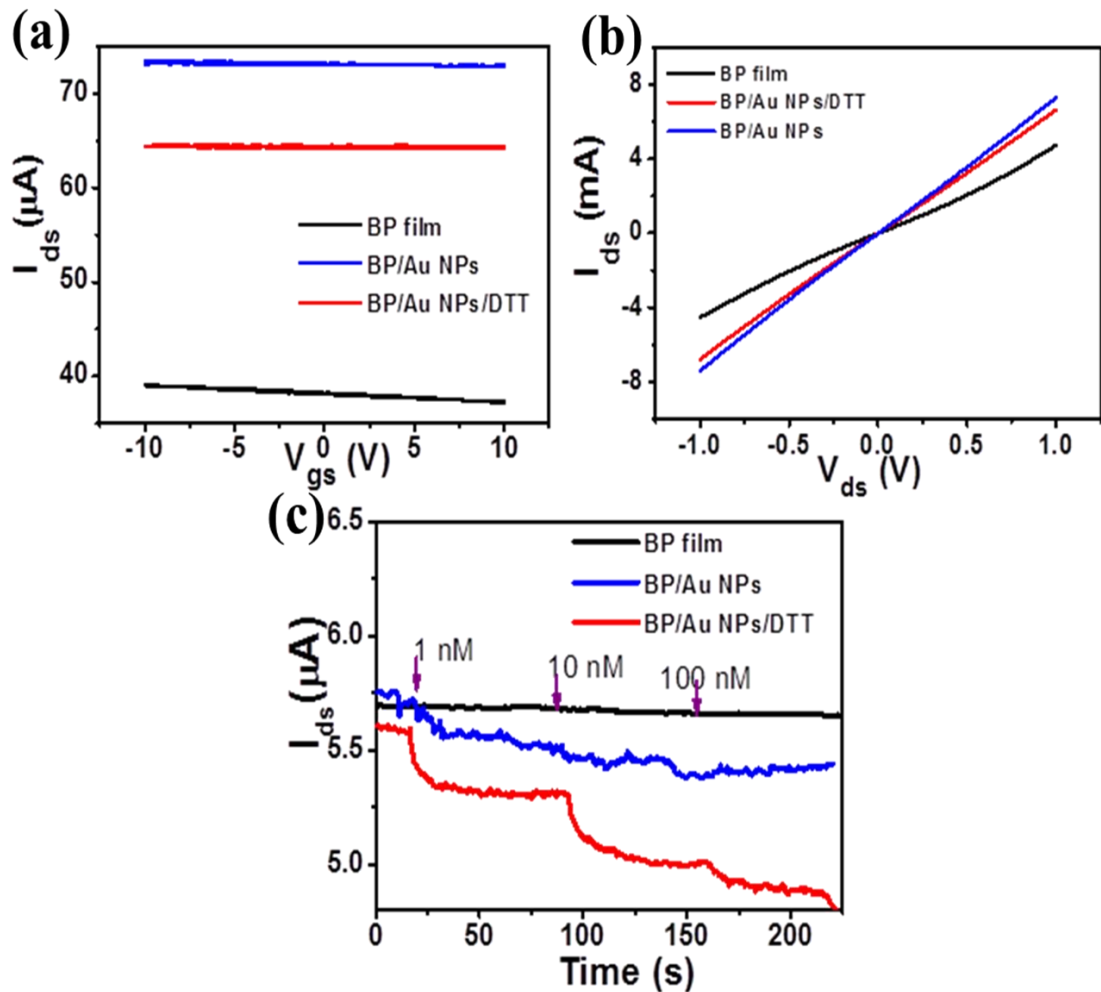


Figure 4.6 (a) I_{ds} - V_{gs} curve with the gate voltage V_{gs} ranging from -10 V to 10 V. (b) I_{ds} - V_{ds} curve with the $V_{ds} = -1$ V~1 V. (c) The I_{ds} vs. time ($V_{ds} = 0.1$ V) (dynamic responses) of BP FET-

based sensing platforms: the prepared BP film (black), BP/Au NPs (blue), BP/Au NPs/ DTT (red) in air.

4.4 Arsenic analysis in lake water samples

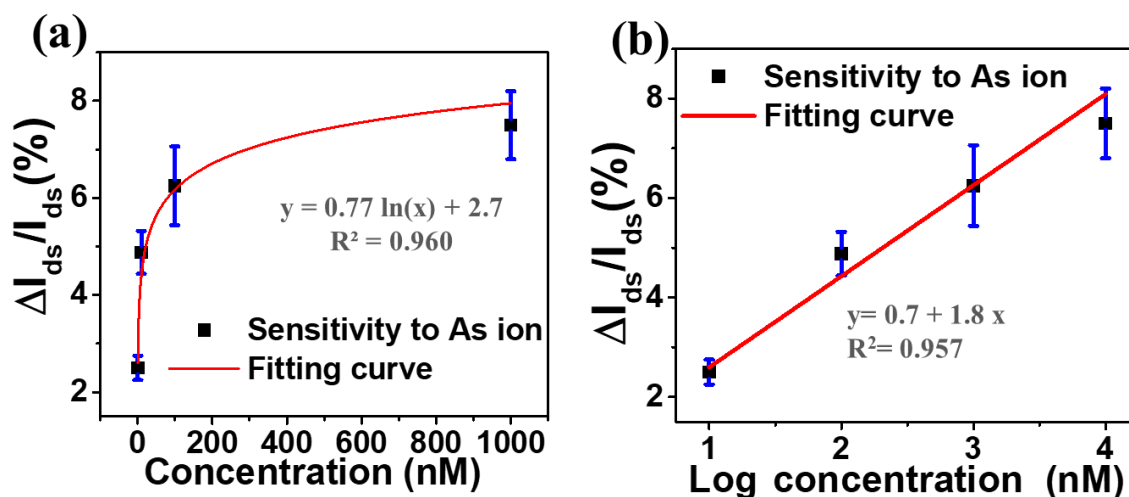


Figure 4.7 Sensitivity to As in water and (a) the logarithmic fitting curve, (b) the linear fitting curve of sensitivity as a function of As concentration for the BP/Au NPs/DTT hybrid sensor.

In Figure 4.7 (a) and (b), a logarithmic curve and a linear curve are used to fit the sensitivity as functions of As ions concentration for the BP/Au NPs/DTT hybrid sensor, respectively. The sensitivity is defined as the ratio of the source drain current change after ion addition ($\Delta I_{ds} = I_{ds}' - I_{ds}$) to the initial current (I_{ds}). The fitting curve enables the BP/Au NPs/DTT platform to predict the As concentration in real water sample. To conduct real water test, it is essential to characterize the selectivity of the platform. Here we prepared solutions containing other metal ions, including Ag^+ , Ca^{2+} , Cd^{2+} , Cu^{2+} , Fe^{3+} , Hg^{2+} , Mg^{2+} , Na^+ , Pb^{2+} , Zn^{2+} , other ubiquitous anionic species in aqueous samples, such as phosphate ions ($H_2PO_4^-$) and humic acid. As shown in Figure 4.8 (a), they were all tested with the BP/Au NPs/DTT platform in the same manner

as we discussed above. The sensors showed negligible responses from Na^+ , Ca^{2+} , Zn^{2+} , H_2PO_4^- and humic acid, but noticeable responses from Cu^{2+} , Mg^{2+} , Cd^{2+} , Fe^{3+} , Hg^{2+} , Ag^+ and Pb^{2+} .

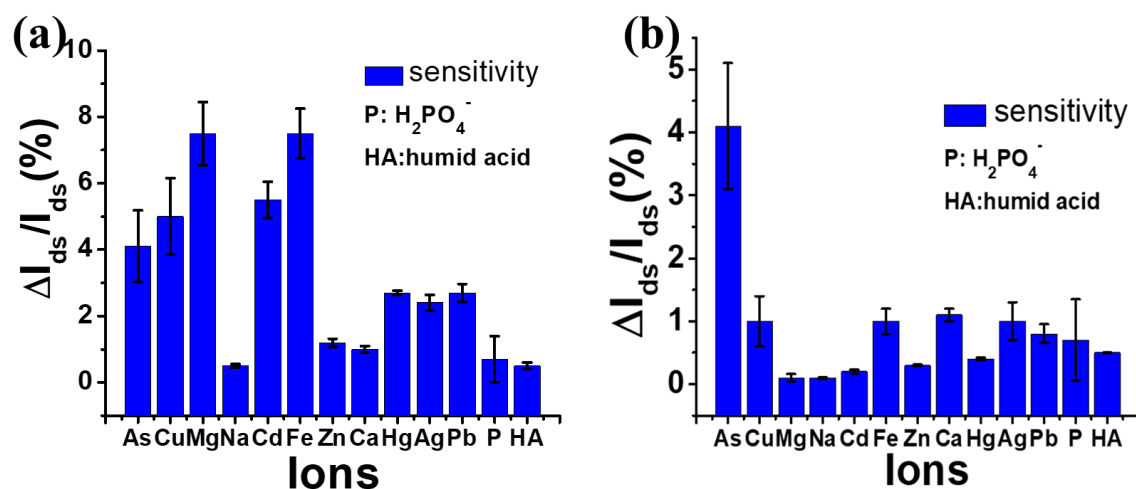


Figure 4.8 Selectivity: real-time detection of As as well as other ions (10 nM), including Ag^+ , Ca^{2+} , Cd^{2+} , Cu^{2+} , Fe^{3+} , Hg^{2+} , Mg^{2+} , Na^+ , Pb^{2+} , Zn^{2+} (a) in initial states (b) with 1:1 molar ratio of EDTA added, phosphate ions (H_2PO_4^-), and humic acid in water with the BP/Au NPs/DTT hybrid sensor ($V_{ds} = 0.1\text{V}$, $V_{gs} = 0\text{V}$).

Since the thioled molecule (DTT) modified sensing platform is not only sensitive to Arsenic ions but also to other metal cations, we also needed to remove potential interferents cations. Many research works have reported that EDTA is broadly used as a chelating agent, as it forms stable complexes with metal cations and suppress their activities.¹⁹⁹⁻²⁰⁰ The effect of EDTA (100 nM) on the sensing platform was negligible, as shown in Figure 4.9. And EDTA will not be able to bond with gold nanoparticles through the SH linkage in the same manner as DTT. Therefore, Cu^{2+} , Mg^{2+} , Cd^{2+} , Fe^{3+} , Hg^{2+} , Ag^+ and Pb^{2+} solutions were re-prepared with ultrapure water, adding 1:1 molar ratio of EDTA (as the disodium salt) and left for 1 hour. As shown in Figure 4.8 (b), an excellent selectivity over most metal ions is obtained, confirming that treatment with cation masking agent is crucial to minimize the heavy metal ion interference.

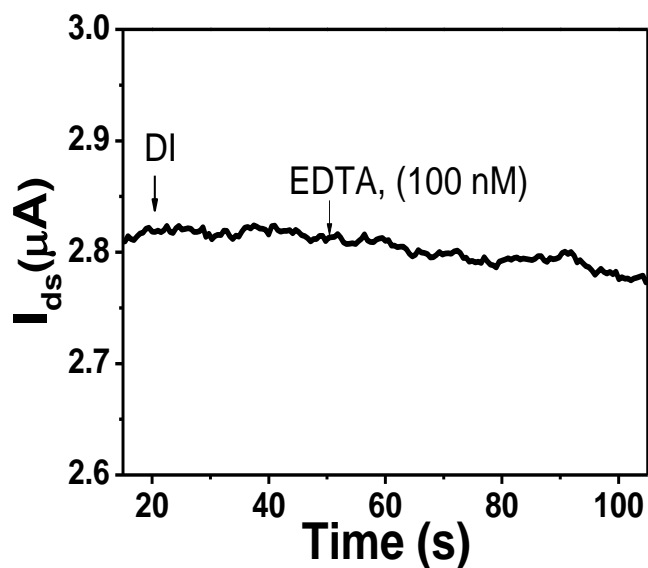


Figure 4.9 The I_{ds} change introduced by EDTA (100 nM) to the BP/Au NPs/DTT platform ($V_{ds}= 0.1$ V, $V_{gs} = 0$ V).

Here the real water samples were collected from Lake Michigan, and the collection locations was 40 meters from Milwaukee Community Sailing Center. The lake water has a very complex chemical composition and contains organic compounds, colloidal particles, bacteria and inorganic ions. Thus, pretreatment of lake water samples is essential to accurately analyze ion species with small molecular weight. In our case, filtration with 0.2 μm pore filter was used to remove potential microorganisms and large suspended particles. EDTA was added into the water for pre-treatment, and the water samples were tested by three different sensors. The prediction result with the BP/Au NPs/DTT platform is shown in Table 4.2. The average sensitivity is 4.68%. The standard deviation of sensitivity is 0.9, indicating good repeatability and consistent performance of the sensors. Comparing with real As concentration, which were obtained by ICP-MS measurement, the error of the prediction is 14%. The prediction experiment suggests that the BP/Au NPs/DTT platform has great potential to develop into a standalone sensor for water pollutant detection.

Table 4.2 Real water sample test with the BP/Au NPs/DTT sensor.

	Result
Average sensitivity tested by three sensors (%)	4.68
Standard deviation of sensitivity	± 0.9
Predicted As concentration by BP/Au NPs/DTT sensor (ppb)	1.01
Real As concentration tested by ICP-MS (ppb)	0.88
Prediction error	14%

4.5 Summary and conclusion

In summary, we demonstrated a sensitive and selective BP/Au NPs/DTT hybrid structure based FET sensor for As ion detection. In the hybrid structure, BP film works as the conducting channel, while the homogeneously dispersed Au NPs are the anchoring sites for the DTT probe, which is specific to As ions. The As ion detection is realized by monitoring the change of the source-drain current in the FET device as a function of the As ion concentration. The LOD can reach down to a concentration of 1 nM. The sensor also shows high selectivity against many other metal ions. Our sensor offers a promising route for the real-time (within 1-2 s), high-performance and low-cost detection of As ions. Overall, the simple fabrication procedure and the excellent sensing performance of the BP/Au NPs/DTT hybrid structure make it promising for real-time detection of As ions in an aqueous environment. To improve the real water analysis, further investigation is needed to construct a comprehensive calibration model considering key factors including the intrinsic electronic property of the sensing platform, ambient environment effect, interference from other water components and the sensing performance.

CHAPTER 5 SENSITIVITY IMPROVEMENT OF THE FET SENSOR BASED ON 2D NANOMATERIALS

5.1 Introduction

In previous chapters, the sensor platform is shown to exhibit a remarkable sensitivity to heavy metal ions with extremely low LODs. The rapid, selective, sensitive and stable detection performance suggests a promising future of the FET sensing platform for in-situ detection of contamination events. The FET platform could be developed into standalone sensors or integrated into existing water equipment for monitoring water contamination and mitigating the public health risk. For real water applications, we need to further understand the sensing mechanism and improve the sensing performance, especially the sensitivity. In section 5.2, we further investigate the sensing mechanism through theoretical analysis and experimental validation, and the gating effect-induced channel resistance change (ΔR_{ch}) is found to be the dominating signal from the sensing performance. To further improve the sensitivity, research is needed to identify critical factors for the gating effect. Section 5.3 discusses channel materials in terms of the effect of their electronic properties on the sensing performance, which suggests that a high sensitivity of sensors can be realized by forming hybrid structures with thinner 2D conducting materials with a larger band gap, a higher carrier mobility, and being coated with the maximum number of specific probes. Section 5.4 investigates the effect of Au NPs, and it is found that balancing the particle size and the particle number to achieve a uniform sensing surface with a maximum areal density could maximize the adsorption of probes. The formation of self-assembly monolayer (SAM) of the thiol-containing probes on Au NPs is

reported in Section 5.5, and the results suggest the optimum time, temperature, pH condition, and concentration for SAM formation.

5.2 Sensing mechanism analysis

To identify the intrinsic electrical signal and thus improve the sensitivity, the simplified Randles circuit and impedance spectroscopy method were used to differentiate the role of each electronic element in the FET platform, as shown in Figure 5.1(a). The platform resistance consists of the system resistance (R_0), the channel resistance (R_{ch}), and the contact resistance ($R_{contact}$) at the interface between the channel material and the gold electrodes. Meanwhile, under the application of voltage, the interface between the channel material and gold electrodes functions as a contact capacitor ($C_{contact}$). During the sensing test, channel capacitance C_{ch} occurs between the electrodes, resulting from the water (C_{H_2O}) and the metal ions-induced electrical double layer (C_{dl}) on the sensing surface. The whole circuit is simplified as the equivalent Randles circuit shown in Figure 5.1 (b).

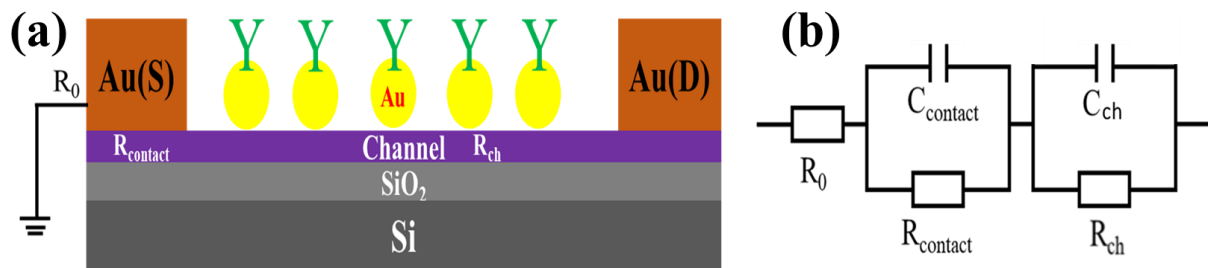


Figure 5.1 (a) Schematic of the FET sensing platform and (b) its equivalent Randles circuit.

The sensor sensitivity is defined as the ratio of the source drain current change after ion adsorption ($\Delta I_{ds} = I_{ds}' - I_{ds}$) to the initial current (I_{ds}). In terms of the resistance, it is expressed as:

$$S_R = \frac{R' - R}{R} = \frac{\Delta R}{R} = \frac{\Delta R_{contact} + \Delta R_{ch}}{R_{contact0} + R_{ch0}} \quad (5.1)$$

Here, R is the initial platform resistance,

R_{ch0} is the initial channel resistance from the channel material,

$R_{contact0}$ is the initial contact resistance at the interface between the channel material and gold electrodes,

ΔR is the total resistance change on the platform induced by the metal ions,

ΔR_{ch} is the channel resistance change induced by the metal ions,

$\Delta R_{contact}$ is the contact resistance change induced by the metal ions.

The initial channel resistance R_{ch0} is determined by the electronic conductivity of the channel material; e.g., the fully reduced monolayer rGO exhibits conductivities ranging between 0.05 and 2 S/cm and field effect mobilities of 2–200 cm²/V-s at room temperature.²⁰¹

$R_{contact0}$ is the initial contact resistance between the channel material and the gold electrodes, introduced by the non-ideal physical contact and the work function difference between the electrode and the channel material.

In the sensing platform, after introducing metal ion solutions, both R_{ch} and $R_{contact}$ would change. Charge transfer will result in the decrease of R_{ch} (Equation 5.2) because positively charged Pb^{2+} ions entrap electrons from the rGO film, thereby increasing the hole density in the p-type rGO film and leading to a decrease in R_{ch} , as shown in Figure 5.2 (a).

$$\Delta R_{ch_{CT}} \downarrow (\Delta R_{ch_{CT}} < 0) \quad (5.2)$$

Gating effect would lead to the increase of R_{ch} (Equation 5.3), since positively charged Pb^{2+} ions adsorbed on the sensor surface generate positive electric field that repels the carriers (holes) in the rGO film, thereby increasing the R_{ch} of the device, as shown in Figure 5.2 (b).

$$\Delta R_{ch_G} \uparrow (\Delta R_{ch} > 0) \quad (5.3)$$

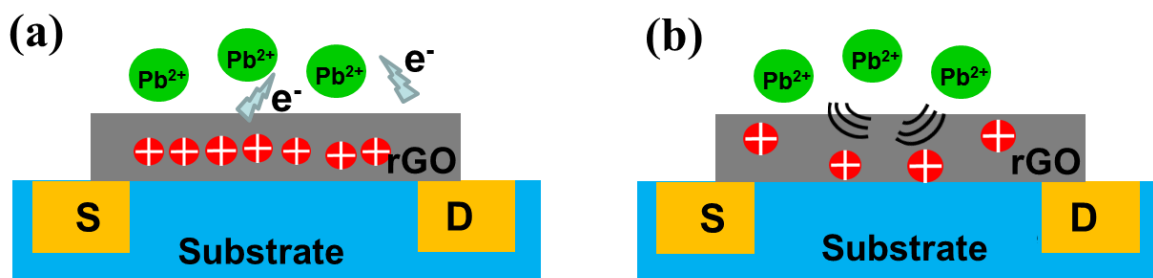


Figure 5.2 Channel resistance change mechanism after introducing Pb^{2+} ions to the rGO/AuNPs/GSH platform: (a) Charge transfer vs. (b) Gating effect.

Meanwhile, gating effect will lead to a decrease in contact resistance R_{contact} . Pb^{2+} ions adsorption results in a positive voltage to the contact regions, enhancing the tunneling probability and thus decreasing contact resistance, as shown in the schematic of Figure 5.3.

$$\Delta R_{c-G} \downarrow (\Delta R_c < 0) \quad (5.4)$$

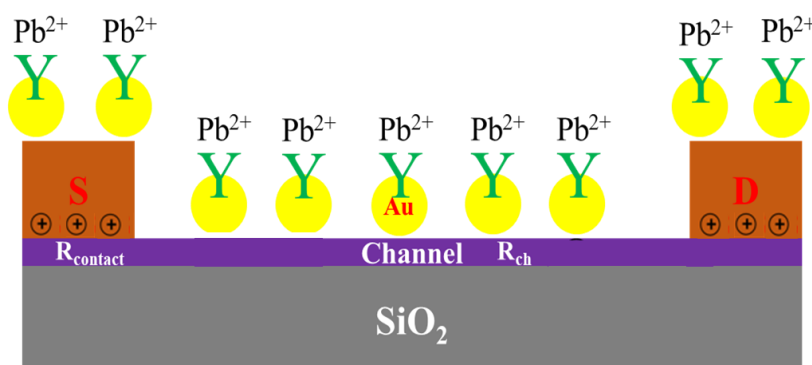


Figure 5.3 Schematic of introducing gating effect to the channel and the contact region: electrons are directly induced in the channel region, but positive voltage is applied to the contact regions.

The AC impedance analysis was employed to quantitatively characterize the channel resistance and the contact resistance changes in the sensing platform with a sinusoidal voltage applied. Figure 5.4 shows the measured electrochemical impedance spectroscopy (EIS) spectra of the Randles circuit for the response of the rGO/Au NPs/GSH platform to Pb^{2+} ions of various concentrations. The fitting of the model to the experimental data was performed using complex

nonlinear least-square procedures which are available in numerous EIS data fitting computer programs. The analysis result in Table 5.1 indicates the R_{contact} decreases with the introduction of Pb^{2+} ions, which agrees with the theoretical analysis of gating effect; the increase in R_{ch} suggests the gating effect is dominant over the charge transfer effect. However, the overall resistance change $\Delta R_{\text{total}}/R_{\text{total}}$ and related sensitivity is relatively low, since the R_{contact} and R_{ch} change in opposite directions. And the total resistance change in the platform is a sum of $\Delta R_{\text{contact}}$ and ΔR_{ch} resulting from the gating effect and the charge transfer (Equation 5.5).

$$\Delta R_{\text{ch}} = \Delta R_{\text{ch}_G} (> 0) + \Delta R_{\text{ch}_{CT}} (< 0) + \Delta R_{\text{contact}_G} (< 0) \quad (5.5)$$

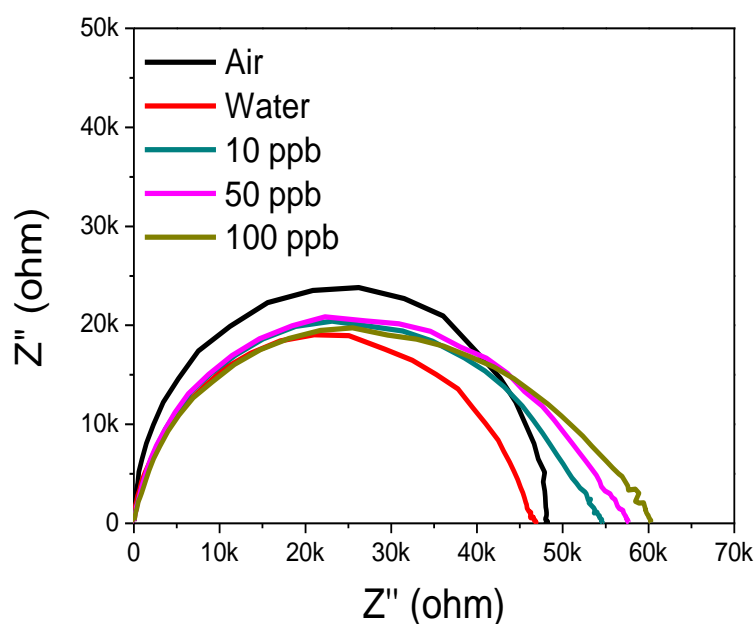


Figure 5.4 EIS spectra of the Randles circuit for the response of the rGO/Au NPs/GSH platform to Pb^{2+} ions of various concentrations.

Table 5.1 EIS analysis result for the response of the rGO/Au NPs/GSH platform to Pb^{2+} ions.

Resistance (Ω)	$R_{\text{contact}0}$	$\Delta R_{\text{contact}}/R_{\text{contact}0}$	$R_{\text{ch}0}$	$\Delta R_{\text{ch}}/R_{\text{ch}0}$	R_{total}	$\Delta R_{\text{total}}/R_{\text{total}}$
Pb^{2+} ion solution						
water	18,800	/	37,548	/	56,348	/
10ppb	11,280	-40%	45,111	20%	56,391	0.08%

50ppb	10,152	-46%	47,686	27%	57,838	2.56%
100ppb	8,460	-55%	51,065	36%	59,525	2.92%

To improve the overall sensitivity, some strategies are proposed, including reducing $R_{\text{contact}0}$; keeping R_{contact} constant, namely, $\Delta R_{\text{contact}0} = 0$; optimizing $R_{\text{ch}0}$; and reducing $R_{\text{ch-CT}}=0$. All these strategies could be realized through adjusting the platform structure, for example, through introducing a passivation layer (Al_2O_3 thin film) as a gate oxide for the channel material. The Al_2O_3 layer would reduce the $\Delta R_{\text{contact}}$ by blocking the interface as a physical barrier and keeping lead ions from leaking into the interface; it could also prevent the electrons from transferring to/from the channel material, thereby eliminating the ΔR_{ch} from the charge transfer effect.

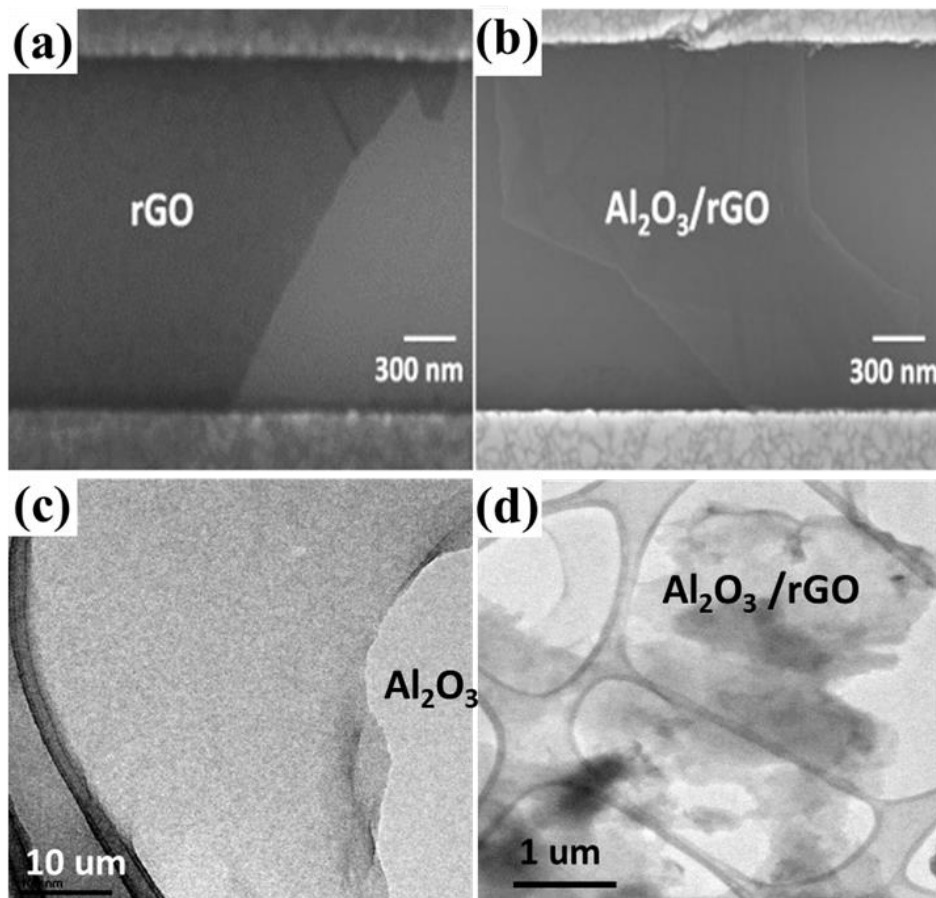


Figure 5.5 (a-b) SEM and (c-d) TEM images of rGO/Al₂O₃ structure indicate the good uniformity of Al₂O₃ film coated on the surface of rGO.

The Al₂O₃ thin film was produced using atomic layer deposition (ALD). SEM and TEM were used to characterize the Al₂O₃ thin film on rGO flakes, as shown in Figure 5.5. The images suggest the good uniformity of Al₂O₃ film coated on the surface of rGO. Figure 5.6(a) shows the schematic of the rGO/Al₂O₃/Au NPs-GSH platform and Figure 5.6(b) compares the sensitivity difference before and after applying the Al₂O₃ passivation layer. Apparently, the application of a passivation layer improves the sensitivity of the rGO/Au NPs-GSH platform to Pb²⁺ ions ranging from 1 nM to 250 nM. It verifies that tuning the sensor platform could potentially improve the $\Delta R_{\text{total}}/R_{\text{total}}$ and the resulting sensor sensitivity. Again, it confirms that the gating effect induced ΔR_{ch} is the dominating signal in the sensing platform.

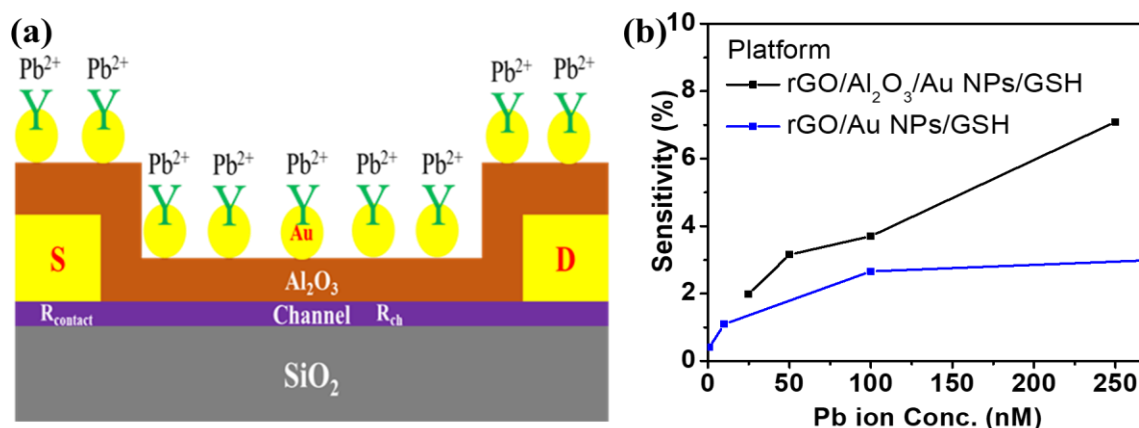


Figure 5.6 (a) Schematic of the rGO/Al₂O₃/Au NPs/GSH platform and (b) its sensing performance before and after applying Al₂O₃ passivation layer.

To further improve the sensitivity of the sensing platform, more research is needed to enhance the R_{ch} change induced by the gating effect and to identify critical factors for tuning the gating effect. Investigation into each component of the sensing platform is needed, e.g., optimizing the channel material, maximizing the anchoring site density and the probe coverage.

5.3 Channel material investigation

Aiming at theoretically analyzing the sensitivity of FET sensors, the MoS₂/DNA-Au NPs sensor is taken as an example. For the conductance-based sensor, the sensitivity S is defined as the ratio of the conductance change (ΔG) to the initial conductance (G_0), namely, $S = \Delta G/G_0$, which is also often replaced by its equivalent form $S = \Delta I/I_0$ since the current is directly monitored during the sensing test with the constant source-drain voltage V_{ds} ($G = I_{ds}/V_{ds}$). For the p-type semiconductor, $S = \Delta n_h/n_{h0}$, where Δn_h and n_{h0} are the change of hole concentration induced by the ion adsorption and the initial hole concentration, respectively. Here, $\Delta n_h = \Delta Q/t$ in which ΔQ is the amount of charge transfer and t is the sensor film thickness. n_{h0} in the p-type semiconductor is approximately proportional to $\mu^{-1} \exp(-E_g/2k_B T)$, in which μ , E_g , k_B , T are the carrier mobility, the band gap, the Boltzmann constant and the temperature, respectively. Consequently, the sensitivity of the MoS₂/DNA-Au NPs could be described as

$$S(MoS_2) \propto \frac{\Delta Q \cdot \mu(MoS_2)}{t(MoS_2)} \exp\left[\frac{E_g(MoS_2)}{2k_B T}\right], \quad (5.6)$$

which suggests that the MoS₂/DNA-Au NPs hybrid structure will have a higher sensitivity if the MoS₂ thin film has a higher carrier mobility, a smaller film thickness, and a larger band gap.

To validate Equation (5.6) in a quantitative sense, we first did a control experiment by increasing the MoS₂ film thickness from 10 nm to 20 and 28 nm. For such thick films, the mobility and the band gap are invariant and thus only the thickness plays a role in differentiating their sensing performance. The sensor test results in Figure 5.7 clearly indicate that a thinner film offers a better sensitivity. This is because the thinner film has a larger relative carrier concentration variation due to the ion adsorption as the amount of charge transfer is the

same for all the samples studied here. Next, we further studied the effect of carrier mobility. Given that both carrier mobility and band gap vary in thinner MoS₂ films but they barely change in thicker MoS₂ films, we did another control experiment by testing the sensor performance of an rGO/DNA-Au NPs hybrid structure to identify or isolate the roles of the carrier mobility/band gap in the MoS₂ film. Since the same concentration of DNA-Au NPs solution was used here, ΔQ is expected to be similar/even the same in the rGO/DNA-Au NPs and MoS₂/DNA-Au NPs hybrid structures with the same concentration of target ions. Thus, the sensitivity ratio between the MoS₂/DNA-Au NPs and the rGO/DNA-Au NPs hybrid structures is

$$\frac{S(\text{MoS}_2)}{S(\text{rGO})} \propto \frac{\mu(\text{MoS}_2)}{\mu(\text{rGO})} \frac{t(\text{rGO})}{t(\text{MoS}_2)} \exp\left[\frac{E_g(\text{MoS}_2) - E_g(\text{rGO})}{2k_B T}\right], \quad (5.7)$$

Strictly speaking, Equation (5.7) is only exact for the single flake of MoS₂ (rGO) with specific values of the carrier mobility and the band gap. However, Equation (5.7) can still be adopted for the MoS₂ (rGO) film in which many flakes are patched together using the effective carrier mobility and band gap.

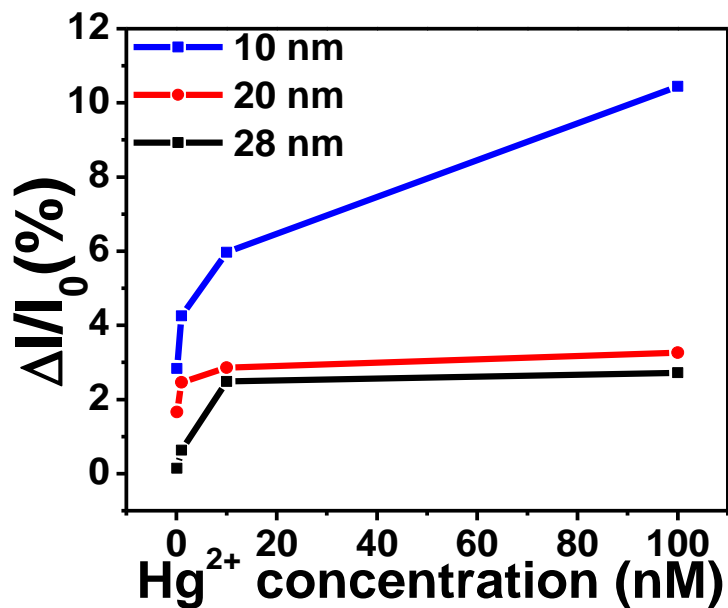


Figure 5.7 Sensitivity as a function of Hg^{2+} concentration for the $\text{MoS}_2/\text{DNA-Au}$ NPs hybrid sensor with different MoS_2 film thicknesses.

For the p-type MoS_2 (rGO), its conductance is proportional to the product of the effective carrier mobility (μ_{eff}) and the carrier concentration [$\mu_{eff}^{-1} \exp(-E_{g,eff}/2k_B T)$], namely, proportional to $\exp(-E_{g,eff}/2k_B T)$. Close examination of Figure 3.6 (b) and Figure 5.8 suggests that the initial source-drain currents for the MoS_2 and rGO based hybrid structures are very similar to each other (0.68 μA vs. 0.74 μA), indicating that their effective band gaps are comparable and the sensitivity is determined by the effective carrier mobility and the film thickness. The carrier mobility for multilayer MoS_2 is within 30-60 $\text{cm}^2\text{V}^{-1}\text{s}^{-1}$,²⁰² while it varies from 0.2 $\text{cm}^2\text{V}^{-1}\text{s}^{-1}$ to 0.6 $\text{cm}^2\text{V}^{-1}\text{s}^{-1}$ for the rGO thin film.²⁰³ The thicknesses of the MoS_2 and rGO thin films in our sensors are 10 nm and 1 nm, respectively. Consequently, the $S(\text{MoS}_2)/S(\text{rGO})$ can be estimated to range from 5 to 30; namely, the higher carrier mobility in MoS_2 would enhance the sensitivity by a factor of 5~30. In our experiments, the sensitivities of the MoS_2 (rGO)/DNA-Au NPs hybrid structure at the Hg^{2+} concentrations of 10 and 100 nM are 6.77% and 11.8% (0.2% and 1.3%), respectively. Therefore, the sensitivity enhancements are 13.5 and 9.1, respectively, just within the estimated range (5~30). It should be noted that our comparison between MoS_2 and rGO here would not imply that the MoS_2 based sensor is better than the rGO-based one; instead it only suggests future directions to achieve a lower detection limit by making thinner films with a larger band gap and a higher carrier mobility.

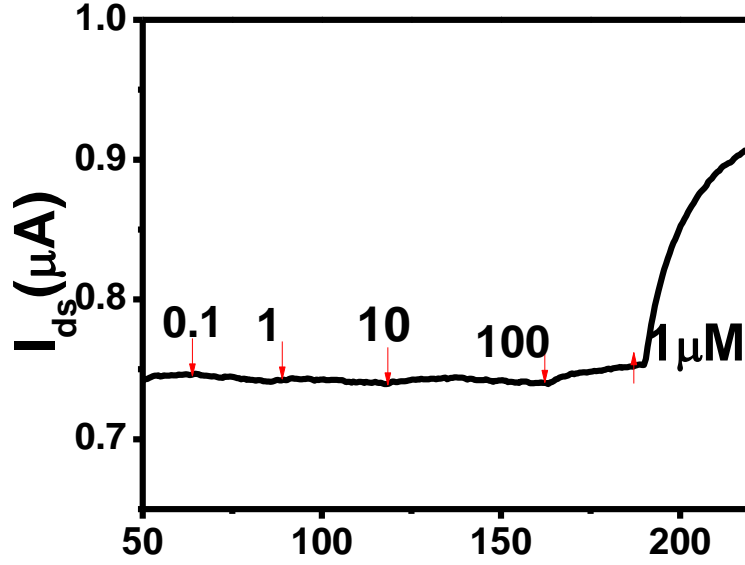


Figure 5.8 Real-time detection ($V_{ds} = 0.1$ V) of Hg^{2+} in water, with concentrations ranging from 100 pM to 10 μ M, using the rGO/DNA-Au NPs hybrid sensor. The rGO/DNA-Au NPs hybrid structure sensor was prepared with a similar method used in our previous study.⁵²

In principle, the conductance of our MoS_2 /DNA-Au NPs sensor increases gradually with the cumulative addition of the Hg^{2+} solution. The rate of increase in the conductance or source-drain current is dependent on the Hg^{2+} concentration. Moreover, this rate should gradually decrease to zero (or the sensitivity should gradually increase and eventually saturate) as the Hg^{2+} concentration increases, because the attracting sites in the DNA probes become fewer and fewer. The relationship between the sensitivity and the Hg^{2+} concentration can be described as

$$S = A[1 - \exp(-Bx)], \quad (5.8)$$

in which A and B are the fitting parameters, and x is the ion concentration. For our MoS_2 /DNA-Au NPs hybrid sensor shown in Figure 3.8 (a), A and B are fitted to be 11.6 and 0.26/nM, respectively. Note that A and B are intrinsic to the conducting channel materials and DNA probes. And the magnitude of the sensitivity (A) is dictated by the properties of conducting channel materials, while its rate of increase (B) is determined by the type of DNA

probe and its concentration. Equations (5.6) - (5.8) thus suggest that the high sensitivity for future sensors can be realized by forming hybrid structures with thinner 2D conducting materials with a larger band gap, a higher carrier mobility, and being coated with the maximum number of specific DNA probes. Therefore, sensitivity-related factors are semiconducting property of the nanomaterial (band gap, carrier mobility) and areal density of probes on the surface.

Per the theoretical analysis, we suggest employing monolayer MoS₂ and BP with a relatively larger band gap as the channel material to achieve a higher sensitivity. On the other hand, graphene has outstanding ultra-high carrier mobility among all the nanomaterials that we have introduced. However, in the real experiment, besides the semiconducting property, we also need to consider the challenge in material synthesis and transfer.

5.4 Effect of Au NP density

To improve the adsorption capacity of the Au NPs and the areal density of probes, investigation into the probe anchor—Au NPs was conducted. Literature reported that the relationship between the capacity of the probe adsorption and Au NPs mainly depends on the size of the Au NPs (the effective diameter for the adsorption).²⁰⁴ The particle size and the amount are controllable by changing the sputtering current and sputtering time, respectively. A group of control experiments were conducted for six samples with sputter-coated Au NPs on the surfaces, which were prepared with different sputtering parameters as shown in Table 5.2. The morphology of each sample was characterized with SEM, as shown in Figure 5.9, which enables the measurement of the particle size and number on the sensing surface. From

samples No.1, No.2 and No.3, we can easily tell that increasing the sputtering time results in the increase of particle number from 76 to 96 and to 104 counts. The higher the sputtering current is, the larger the particle size will be, which further leads to the particle congregation as shown in sample No.6. Besides the nanoparticles size, the number of reactive surface sites also affects the effective surface for probe adsorption. The particle number was counted with Software ImageJ. The areal density ($=N \times \pi D^2 / (\text{sample area})$) was defined as the indicator for effective adsorption surface and sample area = 24,000 nm². As calculated, samples No.2, No.3, No.4 and No.5 have obviously higher particle areal densities than sample No.1.

Table 5.2 Parameter settings for the Au NP sputtering.

Factors	Sample 1	Sample 2	Sample 3	Sample 4	Sample 5	Sample6
Sputtering current	10 mA	10 mA	10 mA	20 mA	20 mA	25 mA
Sputtering time	3 s	5 s	7 s	3 s	5 s	3 s
Au NPs size (D)	3 nm	3 nm	3 nm	4 nm	5 nm	12 nm
Count density (N)	76/ 24000nm ²	96/ 24000nm ²	104/ 24000nm ²	57/ 24000nm ²	45/ 24000nm ²	N.A.
Areal density	2147.8 nm ² / 24000 nm ²	2713.0 nm ² / 24000 nm ²	2939.0 nm ² / 24000 nm ²	2964.2 nm ² / 24000 nm ²	3140.0 nm ² / 24000 nm ²	N.A.
GSH adsorption	36%	40%	45%	42%	43%	27%

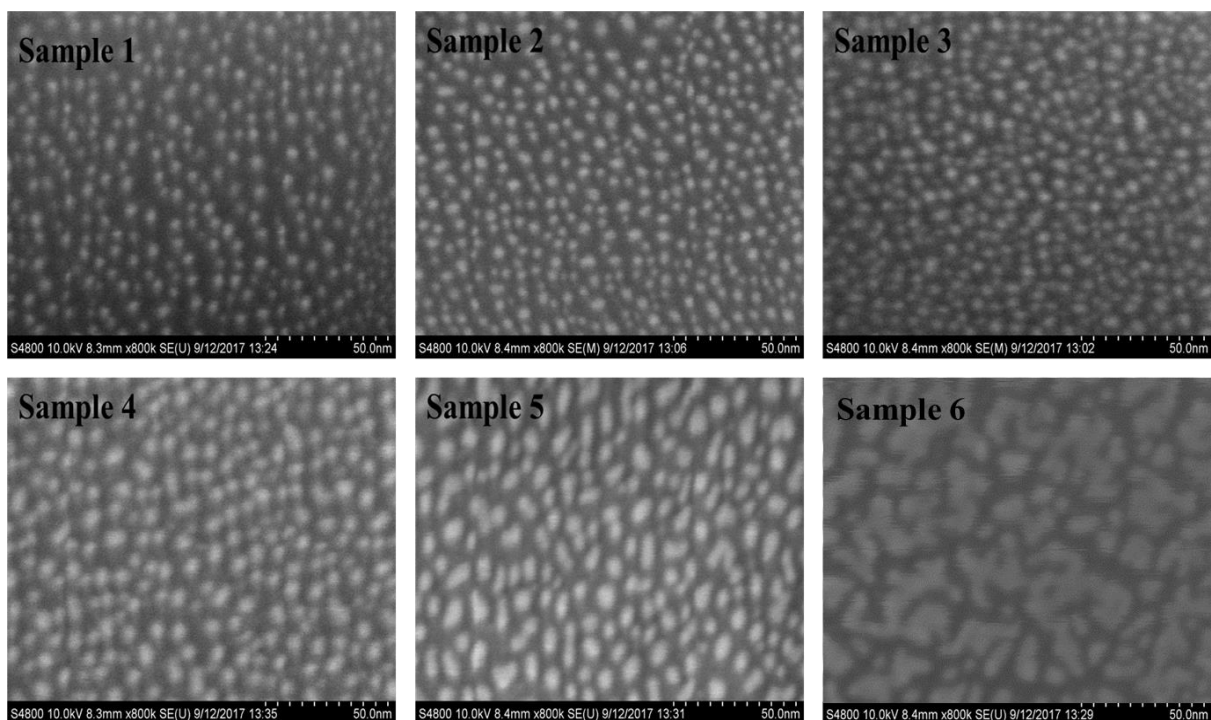


Figure 5.9 The morphology of Au NPs under different sputtering parameter settings.

To identify the real effect of Au NP size on the probe adsorption, GSH adsorption was taken as an example for the following experiment. We prepared 6 groups of samples with the same parameters of samples No.1 to No. 6. Each group has four of 1.5 cm×1.5 cm silicon wafers, and they were submersed in saturated 1 mL GSH solution (50 μ M) for 1 hour, as shown in Figure 5.10. Afterwards, the sample wafers were taken out, and the remaining GSH concentration in the solutions was measured with Fluorescence Plate Reader by reacting with the commercial Thiol Green Indicator.

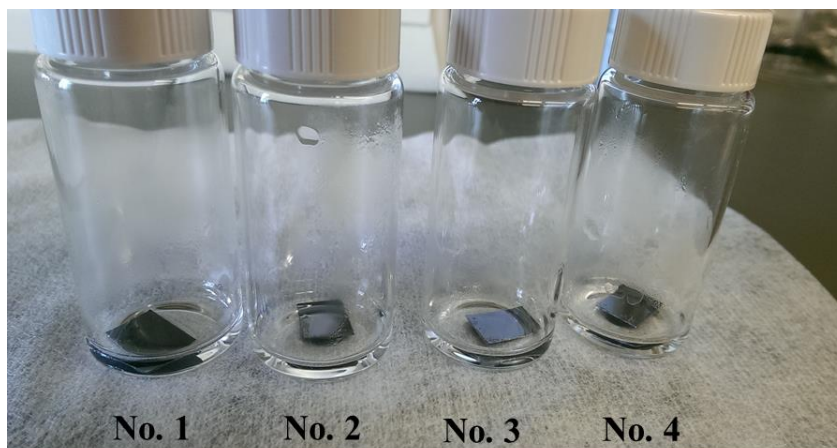


Figure 5.10 Prepared 1.5cm×1.5 cm silicon wafers submersed in saturated 1 mL GSH solution(50 μ M).

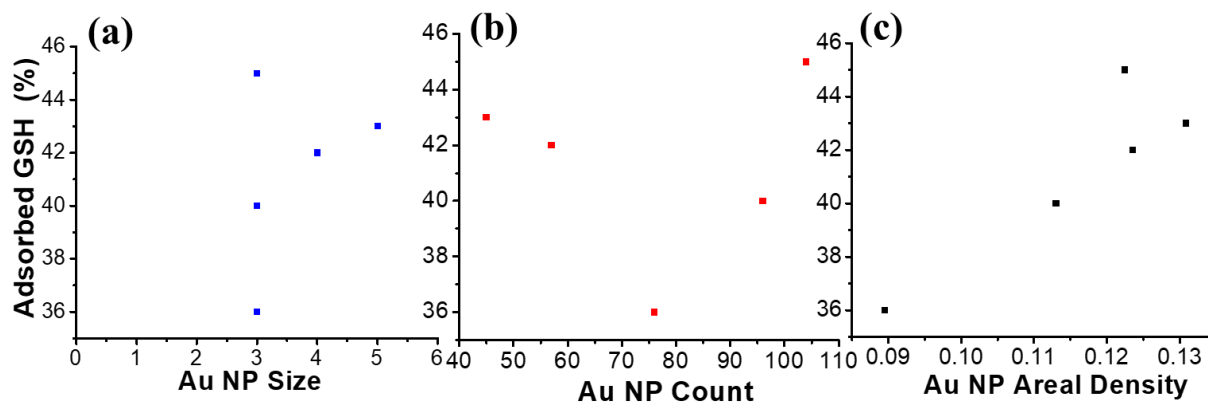


Figure 5.11 Correlation between GSH adsorption and (a) Au NP size, (b) particle number and (c) areal density.

Figure 5.11 exhibits the correlation between GSH adsorption and Au NPs size, count and areal density. It indicates, compared with particle number or particle size, the probe adsorption has higher dependency on Au NPs areal density, as shown in Figure 5.11 (c), which will be used as the index for the effective probe adsorption. Therefore, balancing the particle size and the particle number to achieve a uniform sensing surface with a maximum areal density could maximize the probe adsorption. However, different sputter coaters have different sputtering

intensities. In this thesis, the parameter setting for RF (60Hz) Emitech K550x sputter coater in Table 5.2 is just used as a reference.

5.5 Effect of probe coverage

In this thesis, different molecular recognition probes were used, including small organic molecules (e.g., GSH, DTT) and DNA. The probes were immobilized onto the sensing surface through the thiol-gold bonding with anchoring sites (Au NPs), generating a SAM. To maximize the probe adsorption, we investigated critical factors for the thiol-gold bonded SAM, i.e., concentration, temperature, time and pH condition.

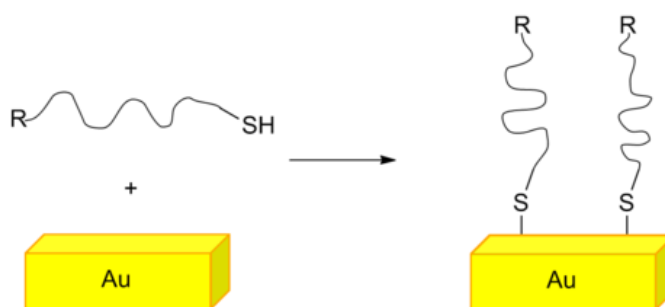


Figure 5.12 Dynamics and kinetics of thiol coating on Au: from approaching to adsorption.

Literature reported that the self-assembly is a spontaneous process from approaching to adsorption, as shown in Figure 5.12. Its growth in micromolar solutions is a multistep process consisting of a fast-initial adsorption followed by at least one slower step involving organization of the monolayer. The onset of thiol adsorption is rapid, occurring within a few seconds, and proceeds to an identifiable saturation point within a few minutes.²⁰⁵ Others also reported that SAM adsorption is a linear behavior with time for most of the adsorption, with a distinct slowdown at greater than about 80% of a monolayer. Steady-state coverage is independent of solution concentration even at a small concentration, and eventually the coverage

reaches a “full” monolayer.²⁰⁶ Therefore, the maximum solubility of probe is more than enough. In terms of the time effect, changing the time for the SAMs formed on gold surface from 0.5 h to 24.0 h did not introduce significant variation of mechanical stability for them. Further prolonged reaction time to 5 days can even weaken the thiol–gold interactions. This result indicates that from the stability point of view, 0.5 h is enough for the formation of SAMs, and very long reaction time is not helpful.²⁰⁷ For the temperature effect on SAM formation, simulation and experimental results both revealed that the values of local thermal boundary conductance (TBC) at gold/SAM interface do not change significantly within the temperature range of 280 to 340 K.²⁰⁸ Furthermore, environmental pH (from 5 to 8) will not affect the stability of the SAMs. However, during the formation of SAMs, the solution pH changes from 5 to 8 can affect the efficiency for the conversion of thiol–gold contacts from coordinate bonds to covalent bonds, since basic solution facilitates the deprotonation of thiol group (-SH).²⁰⁷

Eventually, with all the information we identified above, we measured the GSH- Au NPs coverage ratio. ICP-MS was employed because of its great advantage of being independent of sample preparation. It means sample loss during the washing step does not affect the test results. As shown in Table 5.3, GSH of 163 mM (the max solubility of GSH in water) were added to 50 μ M Au NP solution (uniform particle of 5 nm, from Sigma Aldrich). After being incubated for 1 hour at room temperature, the mixed solution was washed with ultracentrifugation (15,000 rpm, 10 mins) for three times, and then the sediment was diluted in ultrapure water again. The average GSH/Au NPs coverage ratio is identified to be 5.49, indicating sufficient amounts of probe molecules have been immobilized onto the FET

platform for the specific reaction with analytes. The repeatable test result implies ICP-MS is a reliable method to identify the probe coverage.

Table 5.3 Au NPs - GSH coverage ratio tested by ICP-MS.

Prepared Concentration		Prepared GSH/Au molar ratio	ICP-MS Tested GSH/Au coverage ratio
GSH (mM)	Au NPs (uM)		
163	50	3260	5.49

5.6 Summary and conclusion

We investigated sensitivity improvement through theoretical analysis and experimental validation. Randle equivalent circuit was used to identify the intrinsic electrical signal in the FET platform, which consists of system resistance (R_0), the channel resistance (R_{ch}), the contact resistance ($R_{contact}$) between the channel material and terminals (gold electrodes), contact capacitance ($C_{contact}$), and channel capacitance C_{ch} . The impedance analysis was employed to obtain the Randles circuit parameters. Both the theoretical analysis and the EIS analysis show that metal ion solutions will change the R_{ch} and $R_{contact}$ in the platform. Charge transfer between metal ions and the channel material will result in the decrease of channel resistance (R_{ch}), and gating effect would lead to the increase of R_{ch} and the decrease of contact resistance ($R_{contact}$). It is shown that through applying a passivation layer (Al_2O_3 thin film), which reduces/eliminates the $\Delta R_{contact}$ and prevents the electrons from transferring to/from the channel material, the overall sensitivity can be improved. And it also indicates that gating effect induced ΔR_{ch} is the dominating signal from the sensing platform. Further improvement in the sensitivity could be realized through enhancing the gating effect induced ΔR_{ch} . Therefore, investigation into the 2D nanomaterial based sensing platform is warranted, e.g., optimizing the channel

material, maximizing the anchoring density and the probe coverage. Experimental results further suggest that a higher sensitivity for future sensors can be realized by forming hybrid structures with thinner 2D conducting materials with a larger band gap, a higher carrier mobility, and being coated with the maximum number of specific probes. In terms of the Au NPs, compared with particle number or particle size, the probe adsorption has a higher dependency on particle areal density, which becomes the index for the probe adsorption. Overall, balancing the particle size and the number to achieve a uniform sensing surface with maximum areal density could maximize the adsorption of probes. The formation of SAM of thiol-containing probes on the Au NPs is a spontaneous process from approaching to adsorption. Steady-state coverage is independent of the probe solution concentration because eventually the coverage reaches a “full” monolayer.

CHAPTER 6 STABILITY STUDY OF THE FET SENSOR BASED ON 2D NANOMATERIALS

6.1 Introduction

Considering all the interferences in the real-life water sensing, stable and reliable responses for an extended period are needed for the FET platform, especially for integration into existing water equipment. Stability of the sensor would be limited by the most vulnerable factors including the channel material, the anchoring site, and the probe. To investigate the stability of the FET sensor platform, several subtasks need to be addressed, including the stability of channel materials, the degradation of anchoring sites, the lifetime of probes, etc. Section 6.2 investigates the stability of rGO, MoS₂ and BP in ambient environment and aqueous environment. Al₂O₃ thin film is used to protect BP from being oxidized by O₂ in air or water. Sections 6.3 and 6.4 discuss the stability of sputter-coated Au NPs, probe diffusion and lifetime. Section 6.5 demonstrates the integration of the passivation layer protected FET platform into a flowing system and its application for real-time detection of Pb²⁺ ions.

6.2 Channel material stability investigation

It was noticed that during the rGO sensor storage in air, the resistance of the prepared sensor increased gradually, as recorded in Table 6.1. Under the ambient condition, the prepared rGO would have adsorbed O₂ molecules from air, resulting in the resistance change. Meanwhile, some studies based on density functional theory (DFT) calculations suggest that monolayer MoS₂ with exposed edge sites are also unstable due to oxidation in air.²⁰⁹⁻²¹⁰ It occurs at the

Mo-edges of MoS₂ because of the low energetic barrier to dissociation of O₂ molecules. Experimental observation also confirms the cracking of MoS₂ flakes in air. For the storage of BP thin film, it is widely accepted that the main disadvantage of BP is the poor air stability under ambient condition.¹⁰⁴ It was reported that BP rapidly gets oxidized in air, as O₂ etches away the thinner parts of the flakes, generates fractions and degrades the BP film. Other research work exhibits that the oxidation of BP involves a facile dissociative chemisorption of O₂, whereas H₂O molecules are weakly physisorbed and do not dissociate on the BP surface. Therefore, BP rapidly degrades whenever oxygen is present; however, it is unaffected by deaerated (i.e., O₂ depleted) water.¹⁸⁸ Therefore, the oxidation of the channel material and damage to the platform could be potentially avoided through storing the prepared sensors in an appropriate environment.

To identify the best storage condition, we first prepared a group of rGO sensors and stored them in moist air, dry air, argon (purity: 99%), separately. Their resistance changes in the following 6 months were tracked and recorded in Table 6.1. The sensor resistances on average increased by 206.7%, 7.08%, -6.45% after storage in moist air, dry air and argon for 2 weeks, respectively. Six months later, the increases became 390%, 59%, 6.44% for moist air, dry air, and argon storage, respectively. Compared with the sensors stored in moist air (390%), apparently, the argon stored sensors (6.44%) have better stability. The increase in the sensor resistance in moist air is likely attributed to the adsorption of O₂ and water molecules to the rGO surface, leading to re-oxidation and decrease in the carrier density (and the related conductivity) of the channel material. In contrast, the sensors stored in dry air showed 59% resistance change during 6 months' storage, which indicates that reduced water vapor in

ambient environment would alleviate the re-oxidation of rGO. However, protection of the sensor with an inert gas would prevent the adsorption of O₂ molecules to the channel material surface, enhancing the stability of the channel material, and eventually, improving the sensor lifetime.

Table 6.1 rGO sensor resistance change in different ambient environments.

Time	Group 1 stored in moist air		Group 2 stored in dry air		Group 3 stored in argon	
	Average Resistance (KΩ)	Average Resistance Change	Average Resistance (KΩ)	Average Resistance Change (%)	Average Resistance (KΩ)	Average Resistance Change (%)
1 st day	3.40	/	2.57	/	2.97	/
15 th day	9.83	206.66%	2.75	7.08%	2.67	-6.49%
180 th day	16.64	390.20%	4.18	59.19%	3.13	6.44%

An inert atmosphere (e.g., Ar or N₂) is identified to be the best environment for the channel material storage. Therefore, we prepared MoS₂ and BP sensors in the same manner as we discussed in Chapters 3 and 4, respectively, and stored them in argon. Tables 6.2 and 6.3 demonstrate their resistance changes over the storage. MoS₂ thin film sensors were stable with an average resistance increase of 3.9% after one month's storage in argon. BP sensors were relatively unstable, and their average resistance increased by 285% after 32 days' storage and showed exponential increase after 42 days. Although the prepared BP sensors were stored in argon, they were likely exposed to oxygen when being taken out from argon for the resistance tracking, leading to the oxidation and resulting in the resistance increase. It is thus consistent with the literature that BP rapidly gets oxidized in air and oxygen etches away the thinner parts of the flakes.²¹¹ Recent studies demonstrated that Al₂O₃ encapsulation enables highly stable

BP based devices.^{212 213} Thus, a passivation layer was applied to protect the channel material, especially BP. As shown in Figure 6.1, a 3-nm thick Al₂O₃ film is deposited onto the BP based FET platform using the ALD technology. Compared with the sensor resistance change before the Al₂O₃ film deposition, as recorded in Table 6.3, the application of a passivation layer greatly delayed the oxidation and extended the lifetime of the BP from 32 days to more than two months. It confirms that Al₂O₃ encapsulation protects the BP sensor from rapid oxidation under ambient environment.

Table 6.2 Resistance tracking of MoS₂ based sensors stored in argon.

Time	Average Resistance (KΩ)	Resistance Change (%)
1 st day	49.30	/
8 th day	45.50	-6.2%
18 th day	51.15	5.3%
24 th day	48.58	-1.1%
31 th day	50.60	3.9%

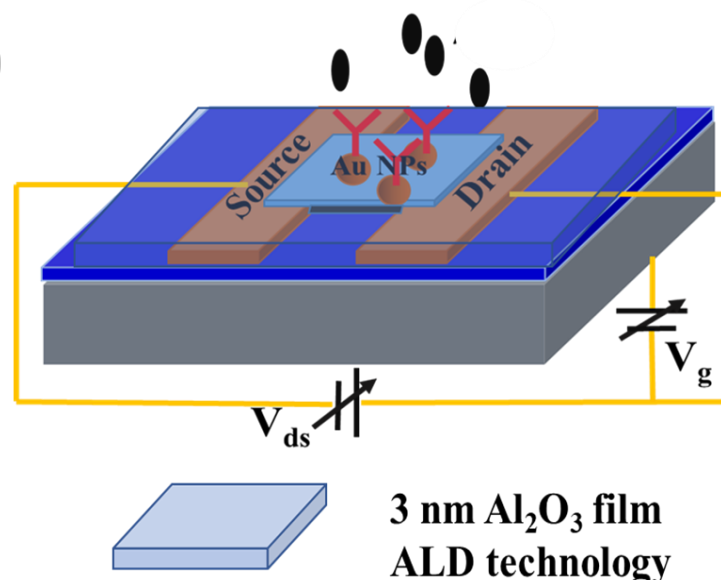


Figure 6.1 Schematic of the BP/Al₂O₃/Au NPs/DTT platform.

Table 6.3 Resistance tracking of BP based sensors stored in argon.

Time	BP sensors stored in argon		Al ₂ O ₃ protected BP sensors stored in argon	
	Average Resistance (K Ω)	Resistance Change (%)	Average Resistance (K Ω)	Resistance Change (%)
1 st day	1.56	/	0.68	/
20 th day	3.50	124%	1.10	62%
32 th day	6.01	285%	1.50	121%
42 th day	2,000	57,000%	3.83	463%
48 th day	Infinity	Infinity	3.90	474%
55 th day	/	/	9.20	1,253%
63 th day	/	/	13.2	1,841%

Further experiment was accomplished through storing the rGO sensors in DI water to verify the stability of rGO in water. As we can identify with the SEM images in Figure 6.2, the monolayer rGO flake did not show any visible change after storage in DI water for one month, which indicates the good stability of rGO in water. It agrees with the literature report that rGOs exhibit high stability in artificial surface water.²¹⁴⁻²¹⁵ DFT calculations reported that both graphene and MoS₂ tend to avoid water intercalation between their layers and only defects located on the basal plane display mild reactivity. MoS₂ edges are stable in water and water-driven oxidation of MoS₂ layers is unfavored compared with adsorption.²¹⁶ Prolonged storage of chemically exfoliated MoS₂ dispersion is found with lateral fracture and aggregation, which is associated with the re-oxidation of the nanosheets. Fortunately, storing the sample in an inert atmosphere could prevent such nanosheet degradation effectively through suppressing the re-oxidation process. And it is crucial to maintain the performance of MoS₂ nanosheets when it is utilized in a device or an application.²¹⁷

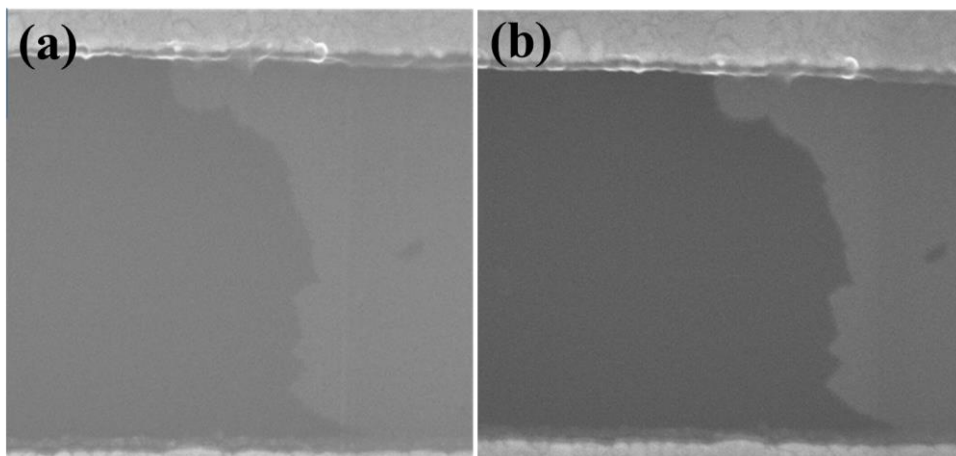


Figure 6.2 SEM images of the Au electrodes with (a) newly prepared rGO flake bridging the electrodes and (b) the same rGO flake stored in DI water for one month.

Finally, we need to identify the stability of the entire FET platform. Here we prepared a group of the rGO/Au NPs-GSH sensors. With an interval of every a few days, their responses were measured with the semiconductor analyzer and recorded. As shown in Figure 6.3, the rGO/Au NP-GSH sensors showed a continuous degradation of response to Pb^{2+} ions during the storage in water, and almost completely lost their reactivity after 4 weeks' storage. Further confirmation indicates the shelf time of rGO/Au NPs-GSH in air is two months. This discovery gives rise to two critical questions. First, why does the sensor lose its reactivity after two months' storage in air? The stability of a sensor would be limited by the most vulnerable component, such as the channel material, the anchoring site, and the probe. A comparison of lifetimes of sensors stored in air and in water indicates that storage in water speeds up the degradation. Therefore, the second question is, which element accelerates the sensor degradation in water? Since we have investigated and confirmed the rGO sensor could survive more than six months in air and it has good stability in water for over one month, the channel

material rGO is not the cause for the accelerated degradation. Further investigation into the anchoring site and the probe is needed.

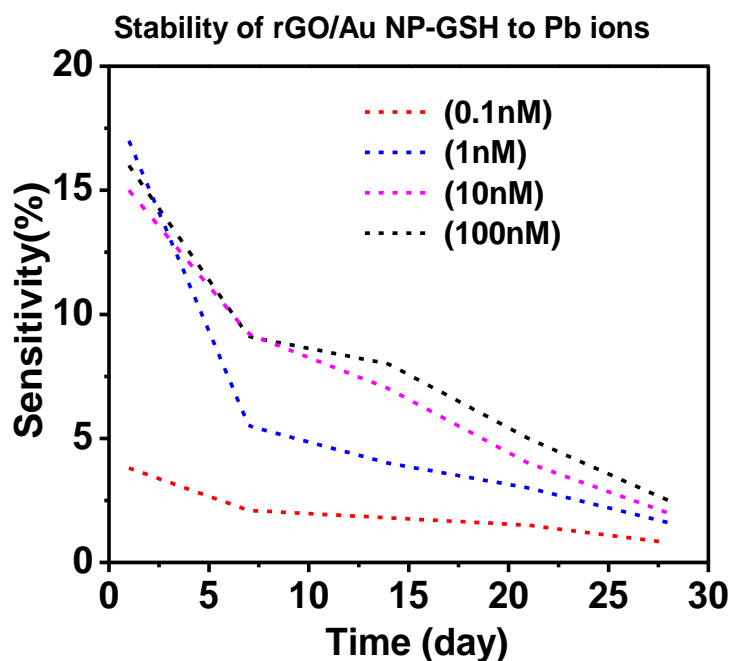


Figure 6.3 The stability of rGO/Au NP-GSH sensor stored in water.

6.3 Anchoring sites -Au NPs stability investigation

To identify the real reason of sensor degradation in water, we need to investigate every element in the FET platform. As we discussed above, Au NPs were sputter deposited onto the sensing surface using an RF (60 Hz) Emitech K550x Sputter coater apparatus with an Au target (99.999% purity) at an Ar pressure of 0.03 mbar. Sputter deposition is a physical vapor deposition (PVD) method of thin film deposition. Sputtered particles/films typically have a better adhesion on the substrate than evaporated particles/films. Au NPs (5 nm) were sputtered and attached on the channel materials with a stable physical contact. Initial stability experiment is to store the Au NPs coated electrodes in DI water to check the anchoring stability of sputter-coated Au NPs in water. SEM imaging was used to track their morphology, and the results are

recorded in Figure 6.4. After 34 days' storage in water, Au NPs were still stably attached on electrodes and the sensor showed no visible difference compared with the newly prepared one. It indicates the good stability of sputter-coated Au NPs deposited on the sensor platform.

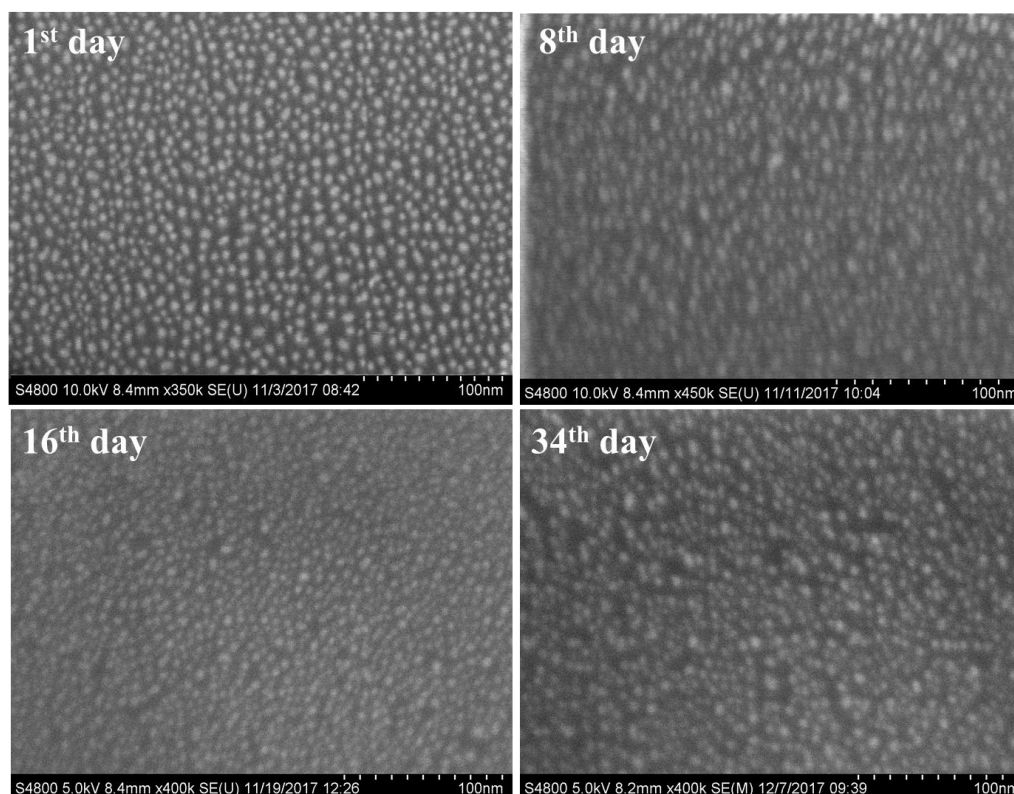


Figure 6.4 SEM images of the sensing surface with sputter-coated Au NPs stored in water for various times as labeled.

6.4 Probe stability investigation

The last possibility for accelerated degradation in water is the probes, which were immobilized on the sensing surface through the anchoring sites. It might be attributed to its detachment from the anchoring site, or its loss of activity. First, we investigated the possibility of its diffusion from the sensor platform during the storage. Initial experiment was carried out by directly measuring the GSH attached on the sensing surface. Conventional methods, including Fourier-transform infrared spectroscopy (FTIR), SEM-EDX (Energy Dispersive X-

Ray Spectroscopy), confocal microscope, etc., were used to measure the GSH molecules on the sensing surface through identifying its chemical bonding, elemental composition, fluorescent signal (after been labeled), respectively. However, none of the conventional methods worked out successfully, since the GSH signal on the sensing surface (300 nm×800 nm) was too weak to be captured. Alternative method is to indirectly test the GSH through replacing the small sensing surface with a much larger Si substrate, which would provide a stronger signal. And it would be more reliable if using fluorescent method to measure and track the GSH diffusion in solution instead of testing GSH on the sensing surface. Therefore, a group of 1.5 cm×1.5 cm silicon wafers were prepared and coated with sputtered Au NPs in the same manner as we discussed above, with the optimum parameters we identified in Section 5.3. It was followed by submersing the Au NPs-coated Si wafers in prepared 1 mL GSH solutions (50 μM) at RT, as shown in Figure 5.10. After 1 hour's adsorption, all the Si wafers were taken out and the remaining GSH solutions were taken for the fluorescence test with a Fluorescence Plate Reader by reacting with the commercial Thiol Green Indicator (Thiolite™ Green). The difference between the initial 50 μM and the GSH concentration in the remaining solutions was defined as the GSH molecules that were attached onto the Au NP surfaces.

Through averaging the results from 3 different samples, we found ~ 19 μM GSH molecules were adsorbed onto the Au NPs. Afterwards, each of the Si wafer with attached GSH was immersed in a vial with 5 ml ultrapure water. The GSH concentration in the ultrapure water was measured every few days to identify the amount of GSH molecules that were detached from the Au NP surface. All the diffusion data were recorded and the diffusion curves were plotted in Figure 6.5, and it reveals that the GSH diffusion was constantly going on. Until the

44th day, about half of the GSH molecules detached from the sensing surface, which explains the limited lifetime of rGO/Au NPs/GSH platform in water. After 103 days, ~ 85 % of the adsorbed GSH probes left the Au NP surface. Another possible mechanism for the loss of GSH molecules under ambient condition is their degradation. Since the surface plasmon resonance (SPR) in Au NPs would give rise to superoxide radical (O_2^-) and O_2^- converts into hydroxyl radical (OH^\cdot) in humid environment, OH^\cdot radicals could react with GSH. Eventually GSH breaks down due to the SPR of Au NPs.²¹⁸⁻²²⁰ Thus, to protect GSH from degradation, the best storage condition would be dark condition and O_2 , H_2O free environment (e.g., Ar or N_2 atmosphere).

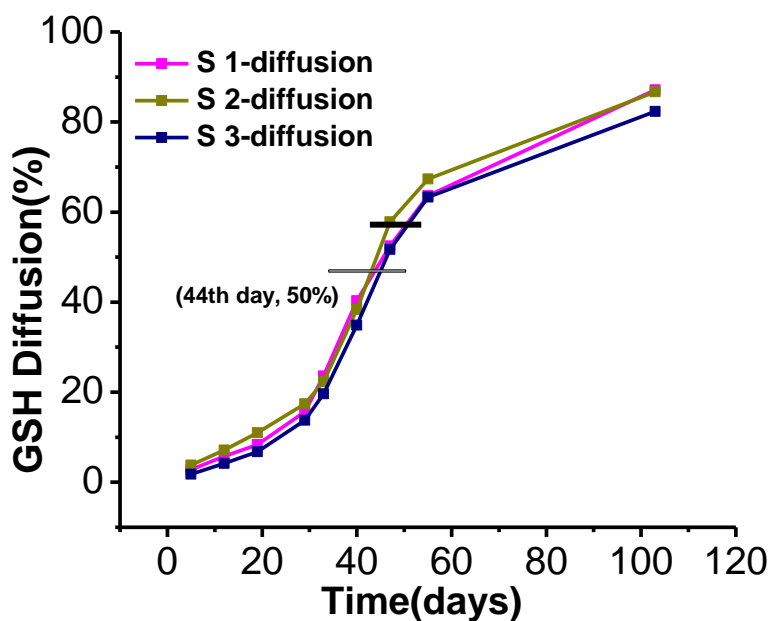


Figure 6.5 The plot of GSH detached from Au NPs in ultrapure water.

All the experimental procedures for measuring the GSH detachment were recorded as follows:

Preparation of GSH-functionalized Au NPs

1. Prepare a group of three Si wafer samples by sputtering Au NPs (20 mA, 3S) onto the acetone cleaned Si wafer.
2. Submerge each Si wafer sample into prepared 1 mL GSH solution of 50 μM for 1 hour.
(protected from light and stored at RT to avoid GSH oxidation)
3. Take the Si wafers out and rinse with static ultrapure water.
4. Submerge each of the Si wafers into a vial with 5 mL ultrapure water so that the attached GSH molecules spontaneously diffuse into the clean water. (protected from light and stored at 4 °C)
5. Measure the GSH concentration in the ultrapure water to identify the amount of GSH that got detached from the Au NP surface.

Identification of the calibration curve for GSH concentration

1. Prepare standard GSH solutions of various concentrations: 100 μM , 50 μM , 20 μM , 10 μM , 5 μM , 2 μM , 1 μM , 0 μM with KPE (0.1 M potassium phosphate buffer with 5 mM EDTA disodium salt, pH 7.5).
2. Identify their pH values with pH meter: 4.34, 4.75, 5.45, 6.65, 7.50, 8.11, 8.10, respectively.
(pH value of DI water in Global Water Center, Milwaukee, Wisconsin: 7.34)
3. Adjust pH values of these calibration solutions with PBS buffer ($\times 1$) to 7.

GSH-Au NPs quantification with florescent plate reader

1. Extract 50 μL blank DI water, 50 μL calibration solution of each concentration, 50 μL GSH diffusion solution of each sample to the 96 well plate. Repeat 3 times.
2. Thaw the frozen Thiol Green Indicator (40 μl per vial) with PBS buffer ($\times 1$) (pH= 7), 1.5 mL.

3. Extract 50 μL Thiol Green Indicator into the blank DI water, each calibration solution and each GSH diffusion solution in Step 1. Protect the samples from light and keep at 4 $^{\circ}\text{C}$.
4. Test the fluorescent intensity of samples in Step 3 with Fluorescence Plate Reader. (Ex/Em (nm)=510/524) within 1 hour starting from Step 1. Average the result for each sample as the GSH intensity signal.
5. Identify the calibration curve with all the intensity signals of the calibration solutions in Step 4, as shown in Figure 6.6 and calculate the GSH concentrations in the diffusion samples through interpolation.

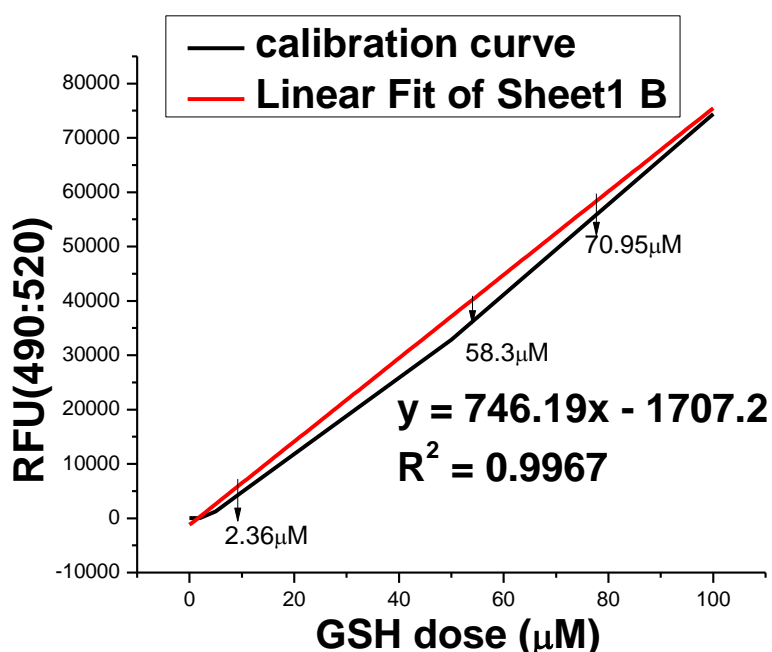


Figure 6.6 The calibration curve for GSH concentration and the interpolation calculation.

For the stability of probes in the sensing platform, another aspect is the lifetime of probes. Conventional methods to test the chemical activity of GSH are High Performance Liquid Chromatography (HPLC) and Ion Titration. As the vendor (Sigma Aldrich) tested, GSH and DTT both have one year's chemical activity, starting from the date of shipping. It means probe's chemical activity is not the limitation for the rGO/Au NPs/GSH sensor's lifetime in air

and in water. Moreover, the best storage temperature for GSH (and DTT) is 2- 8°C. For another probe used in this thesis, DNA, the storage time is 2 years at - 20 °C, 1 year at 4 °C and 6 weeks at 37 °C, as the vendor (IDT) suggested.

6.5 Flowing water test

For the stability improvement, Al₂O₃ passivation layer is used to protect the channel material from being oxidized in air and water. Here we take the test of lead ions with rGO/Al₂O₃/Au NPs/GSH sensor as an example. The sensor uses monolayer rGO to bridge the electrodes and then is coated with Al₂O₃ thin film with ALD technology to protect the rGO and the gold electrodes, followed by the sputter-coated Au NPs and immobilization of GSH molecules. The FET platform was developed into sensors of 5 mm×8 mm based on the Si substrate, as shown in the inset of Figure. 6.7 (c). The sensor chip is imbedded in a test cell (Figure. 6.7 (c)) and then integrated into a flowing system switchable between metal ion solution and DI water, which is demonstrated in Figure 6.7 (a). Figure 6.7 (b) shows the 3-way valve used in the system to switch the water inlet between metal ion solution and DI water. Figure 6.7 (d) is the updated bypass system that allows for the assembly of the test cell into the flowing tube.

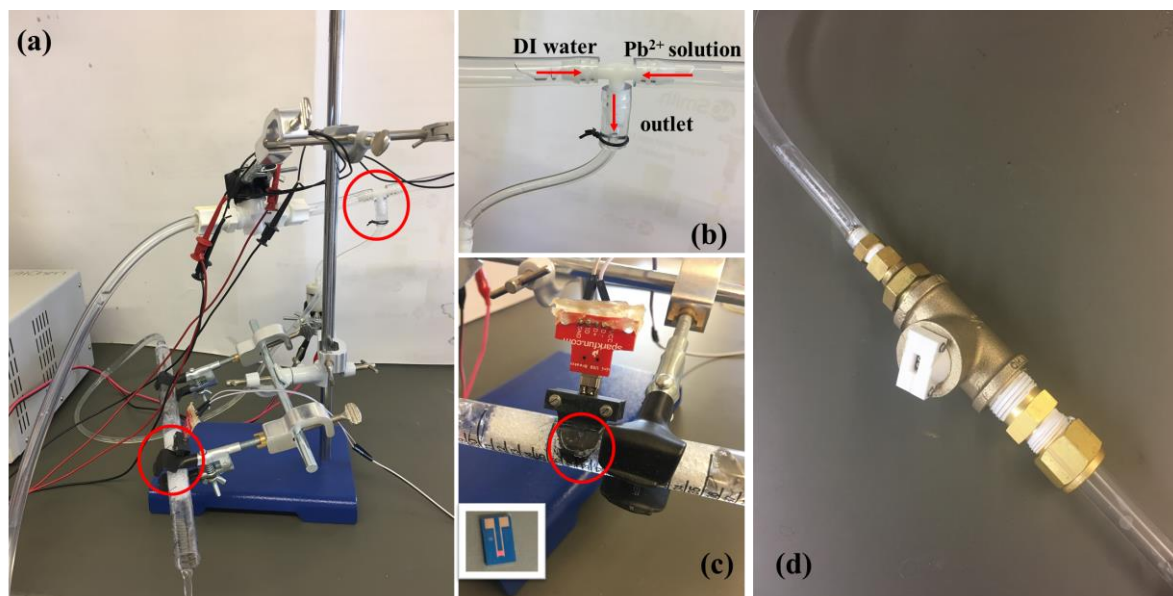


Figure 6.7 (a) The flowing water system; (b) the 3-way valve that controls the switching between metal ion solution and DI water; (c) the sensor imbedded test-cell is integrated in the flowing tube (Inset: the sensor chip); and (d) the bypass system.

The flowing water system enables easy, reliable, and inline detection of metal ions in water with the FET sensor. The repeatable detection performance of flowing Pb^{2+} ion solution is demonstrated in the Figure 6.8. The introduction of Pb^{2+} ions leads to an obvious current change in the sensor, with a lower detection limit of 200 ppb. A control experiment was conducted to test DI water with the flowing system, which showed no current change. It confirms that the current signal indeed results from the Pb^{2+} ions instead of the system. The sensing performance in Figure 6.8 shows that the Pb^{2+} ions-induced response is reversible, and further introducing DI water to the platform will bring the current back to the initial level (before introducing Pb^{2+} ions). However, the current signal reveals a consistent increase upon introduction of lead ions, instead of the decreased current pattern as discussed in Section 2.2 and Section 5.1 (Pb^{2+} ions introduce gating effect that leads to a decrease in the rGO conductivity). This dilemma is not fully understood at this point. However, there are a few

possible reasons that can lead to this opposite response. One possibility is the increase in the ionic conductivity for high concentrations of Pb^{2+} ions, but further research is needed to fully resolve the contribution of the increased ionic conductivity.

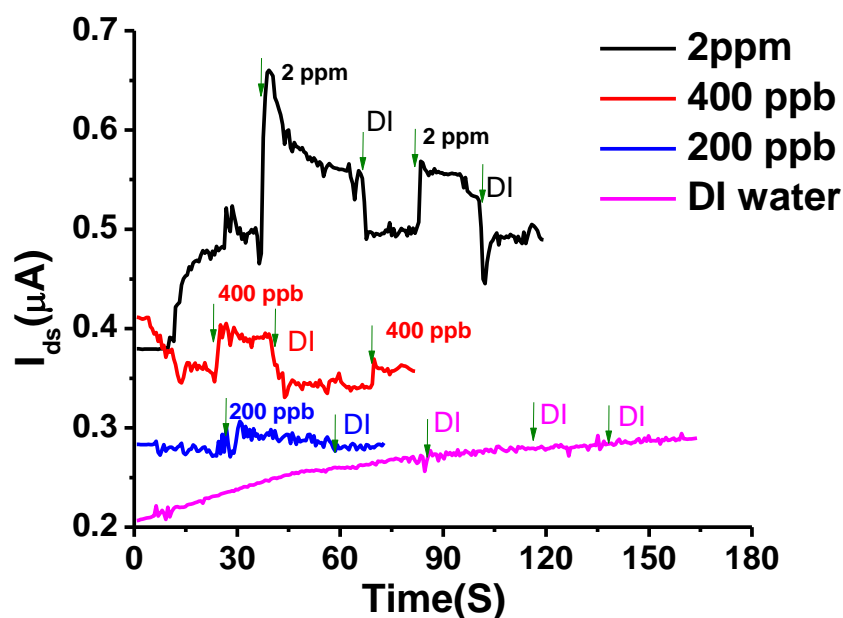


Figure 6.8 The dynamic sensing performance of the rGO/Al₂O₃/Au NPs/GSH sensor to Pb²⁺ ions of various concentrations 200 ppb, 400 ppb, 2 ppm and DI water in the flowing system.

Meanwhile, comparing the testing performance between the flowing water and static water, it is noticeable that the lower detection limit in flowing water (200 ppb) is much higher than that in static water test (2 ppb). Theoretical analysis was conducted to compare the Pb²⁺ ion adsorption and resulting sensing signals in the two scenarios.

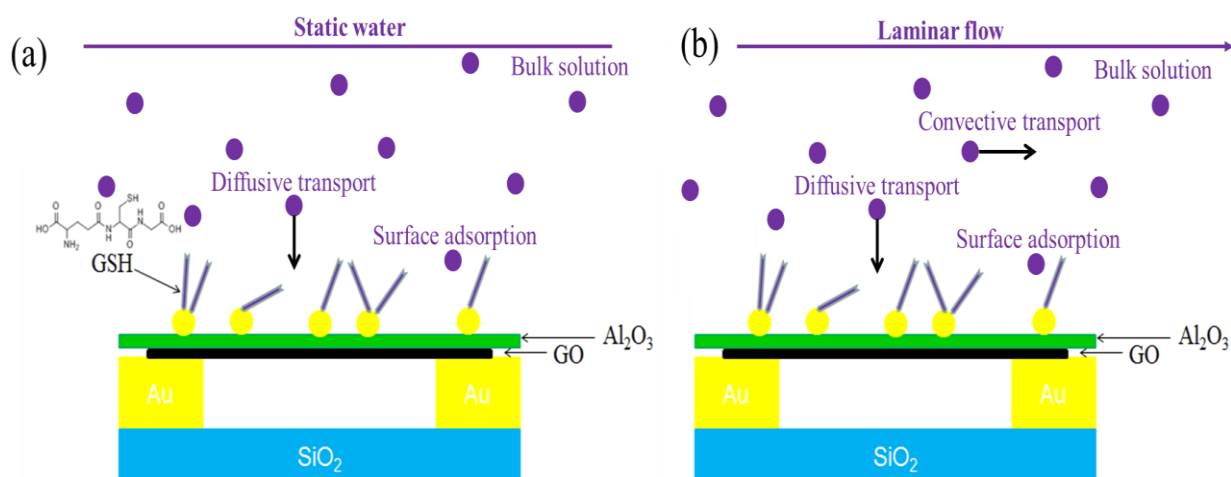


Figure 6.9 Schematic of Pb^{2+} ion adsorption in (a) the static water and (b) the flowing water system.

Figure 6.9 (a) shows the schematic of Pb^{2+} ion diffusion from the bulk solution and adsorption of Pb^{2+} ions onto GSH molecules. While in the flowing water system, besides diffusive transport, the convective transport of Pb^{2+} ions is present, as shown in Figure 6.9 (b). To investigate the Pb^{2+} ion adsorption at equilibrium, we should first estimate the amount of discrete and non-uniform distribution of Au immobilized GSH molecules. The Au-GSH adsorption coverage is calculated as Langmuir adsorption isotherm.

$$\theta = \frac{K_e P}{1 + K_e P} \quad (6.1)$$

where,

θ : adsorption coverage

P : osmotic pressure

K_e : equilibrium constant.

Therefore, the Pb^{2+} adsorption density is:

$$n_a = \theta \cdot s \rho_{GSH} \quad (6.2)$$

where s : the number of Pb^{2+} attached to each GSH,

ρ_{GSH} : areal density of GSH.

Using Grahame equation, Pb^{2+} adsorption induced gating voltage is

$$\Delta V_{Pb^{2+}} = \frac{k_B T}{e} \sinh^{-1} \left(\frac{n_a \times 10^4}{\sqrt{8 k_B T \epsilon \epsilon_0 C_{Pb^{2+}}}} \right) \quad (6.3)$$

The sensor sensitivity is thus

$$S = \frac{\Delta Q}{Q_0} \quad (6.4)$$

where

$$\Delta Q = e \frac{\varepsilon_0 \varepsilon_{Al_2O_3}}{d_{Al_2O_3}} \Delta V_{Pb^{2+}} \quad (6.5)$$

Thus,

$$S = \frac{e \frac{\varepsilon_0 \varepsilon_{Al_2O_3}}{d_{Al_2O_3}} k_B T}{Q_0 e} \sinh^{-1} \left(\frac{n_a \times 10^4}{\sqrt{8 k_B T \varepsilon \varepsilon_0 C_{Pb^{2+}}}} \right) \quad (6.6)$$

Q_0 : initial carrier concentration.

In the flowing water (Figure 6.9 (b)), both diffusive transport and convective transport of Pb^{2+} ions co-exist and the mass balance of Pb^{2+} ions can be expressed as,

$$\frac{\partial C}{\partial t} + \vec{U} \cdot \nabla C = D \nabla^2 C \quad (6.7)$$

Here,

D : diffusion coefficient (diffusivity) of Pb^{2+} in water

C : concentration of Pb^{2+}

\vec{U} : water velocity vector

And the sensitivity induced by the gating effect could be expressed similarly as in Equation (6.6).

$$S = \frac{e \frac{\varepsilon_0 \varepsilon_{Al_2O_3}}{d_{Al_2O_3}} k_B T}{Q_0 e} \sinh^{-1} \left(\frac{q \times 10^4}{\sqrt{8 k_B T \varepsilon \varepsilon_0 C_{Pb^{2+}}}} \right) \quad (6.8)$$

where,

q : adsorption density of Pb^{2+} .

Because of the presence of convective transport, adsorption equilibrium coefficient of the probe will be lower compared with that in the static water. Therefore, the adsorption density

of Pb^{2+} ions (q) is smaller than that of the static state (n_a). As a result, the sensitivity in the flowing water would be smaller than that in the static water. Specifically, the sensing performance difference of the FET sensor is attributed to the flowing water velocity, the size of the tube, and the water pressure in the flowing system, among others.

6.6 Summary and conclusion

The FET sensor stability is investigated by examining each component of the sensor as the sensor stability is limited by the most vulnerable component. Resistance tracking indicates that channel material will adsorb O_2 , which further leads to oxidization in ambient environment, especially BP. An air free and inert gas environment (e.g., Ar) would enhance the stability of the channel materials during the storage. A passivation layer is necessary for protecting the BP sensor from being exposed to O_2 under ambient environment and being oxidized. For stability of the entire platform, rGO/Au NP-GSH sensor shows a continuous degradation response to Pb^{2+} ions during its storage in water, and completely loses its sensitivity after 4 weeks' storage in water. SEM tracking of the sensor platform indicates the good stability of rGO nanosheet and sputter-coated Au NPs in water. Fluorescence plate reader is used for the probes' diffusion tracking. Until the 44th day, half GSH detached from the sensing surface, which rationalizes the limited lifetime of rGO/Au NPs/GSH platform in water. To avoid the probe degradation, the sensors should be stored away from direct sunlight and high humidity. An FET sensor integrated flowing water system has been designed for the inline detection of flowing Pb^{2+} ions, which shows a repeatable dynamic response. However, it is unexpected with a current signal of consistent increase and a LOD of as high as 200 ppb, which are partially attributed to the

higher ionic conductivity for high concentrations of Pb^{2+} ions and the convective transport of Pb^{2+} ions in the flowing water system, respectively.

CHAPTER 7 CONCLUSIONS AND OUTLOOK

7.1 Conclusions

The overall objective of the dissertation research is to explore and understand 2D nanomaterials-based FET sensors for water sensing applications. Major conclusions are summarized below under each specific major task.

Task 1. Develop a low-cost, portable, user-friendly, sensitive, and selective analytical platform for in-line analysis of heavy metal ions.

We have demonstrated a sensitive and selective FET sensor based on 2D nanomaterial/ Au NP hybrid structures for detection of Hg^{2+} , Pb^{2+} , As(V) and As(III) ions in water. The hybrid structure consists of a 2D nanomaterial film, homogeneously dispersed Au NPs, and specific probes. Unique properties of various nanomaterials (rGO, MoS₂, and BP) have been explored and specific probes have been identified to realize sensitive and selective detection of toxic heavy metal ions. The detection is enabled by recording the electrical conductance of the device and by monitoring the change in the drain current of the 2D nanomaterial FET sensor device. The platform offers a promising route for real-time (1-2 seconds), high-performance and low-cost detection of heavy metal ions. The lower detection limit can reach the order of ppb, which is below the EPA action level. Meanwhile, the sensor also shows high selectivity against other interfering heavy metal ions. The sensing platform features the following advantages:

Faster – Rapid response for real-time monitoring (detection time on the order of seconds);

Miniaturized – The micron-sized sensor can be integrated into existing water equipment;

Highly sensitive – Lower detection limit on the order of ppb;

Scalable – Fabrication can be scaled up with good reproducibility/high electrical stability;

Inline continuous detection – Sensors can be placed directly in the flowing water system;

Wireless communication compatible – Ready for integration with wireless communication.

The simple fabrication method and excellent sensing performance of the hybrid structure have been demonstrated for the accurate prediction of arsenic ions in lake water.

Task 2. Investigate the FET sensing mechanism.

The investigation of the sensing mechanism in the FET platform is completed through theoretical analysis and experimental validation. Theoretically, the adsorption of target metal ions will induce charge transfer and gating effect in the FET platform. The adsorption of charged ions to the platform will induce the electron transfer between the ions and the channel material, altering the carrier (i.e., holes or electrons) concentration in the channel film and further introducing a current difference between the source and drain electrodes. Meanwhile, the charged ions adsorbed on the sensor surface would generate an electric field, which repels or attracts the carriers in the channel material, leading to a current change between source and drain electrodes. AC impedance analysis indicates resistance in the platform consists of system resistance (R_0), channel resistance (R_{ch}), and the contact resistance ($R_{contact}$) at the interface between the channel material and gold electrodes. The EIS data fitting result agrees with the theoretical analysis that the R_{ch} change is induced by both the gating effect and the charge transfer effect, and the two changes are in opposite directions. As a result, the overall resistance change and the resulting sensitivity is relatively low. Finally the EIS result reveals that the gating effect dominates over the charge transfer in the sensing platform. A passivation

layer (Al_2O_3 thin film) for the sensing platform is proposed and deposited onto the platform with ALD technology to reduce the gating effect on the contact region as well as to reduce the R_{ch} change induced by the electron transfer between the channel material and metal ions, eventually improving the sensor sensitivity.

Task 3. Improving the sensitivity of the nanomaterial-based electronic sensor.

We investigate sensitivity through theoretical analysis and experimental validation. Theoretical analysis indicates that sensitivity related factors are semiconducting properties of nanomaterials (e.g., carrier mobility, band gap), number of probes, and adsorption capacity of Au NPs. Experimental results suggest that the high sensitivity can be realized for future sensors by forming hybrid structures with thinner 2D conducting materials with a larger band gap and a higher carrier mobility, by increasing the areal density of anchoring sites on the platform and enhancing the adsorption of capturing probes. Compared with Au particle number or particle size, the probe adsorption has a higher dependency on Au NPs areal density, which becomes the index for the effective adsorption surface. Overall, balancing the particle size and the particle number to achieve a uniform sensing surface with maximum areal density could maximize the adsorption of probes. Other conditions, e.g., probe concentration, temperature, assembly time, and solution pH, will also affect the generation of self-assembled probe monolayer.

Task 4. Improving the stability of the nanomaterial-based electronic sensor.

To understand and potentially enhance the stability and lifetime of the electronic sensor, we investigate stability through theoretical analysis and experimental validation. It includes the

binding between the nanomaterial and electrodes, the detachment of Au NPs, the lifetime and diffusion of probes, and the sensor overall stability. Initial experiments on the lifetime of rGO storage in water indicates the good stability of the channel material. And protection with an inert gas would prevent the adsorption of O₂ to channel material surface, thereby enhancing the stability of sensors. Meanwhile, the application of Al₂O₃ thin film improves the stability of sensors through protecting the channel material (especially BP) from oxidation. Comparing the resistance change of BP sensor before and after applying the passivation layer, its lifetime extends from one month to more than two months. SEM tracking indicates the good stability of sputter-coated Au NPs in water. Fluorescence test indicates that about 50% GSH probes diffuse away from the sputter-coated Au NPs in 44 days' storage in water. To avoid the probe degradation, the sensors should be kept away from direct sunlight and high humidity. Preliminary experiments show that an FET sensor integrated flowing water system can be designed for the inline detection of flowing Pb²⁺ ions.

7.2 Outlook

For fundamental research, we have reported the 2D nanomaterial-based FET sensor with comparable or better performance than conventional methods and standard instruments. However, there are still several challenges to overcome for the sensor fabrication and testing process at a large scale, degradation and device-to-device variations in the sensor performance/quality. And the application of these heavy metal ion sensors in real tap water or surface water is more complicated than that in ultrapure water. Therefore, further research is warranted to enable the ultimate practical application of these novel FET sensors based on 2D nanomaterials.

Fabrication: From the perspective of device fabrication, the challenge in the uniform fabrication (the ability to fabricate many sensors with the same performance) still exists. It is especially challenging to deposit the channel materials onto the sensing surface, due to their ultra-small size and the technical limitation for nanomaterial preparation and manipulation.²²¹ Currently, the rGO sheets are fabricated onto the substrate through a self-assembly method; chemically exfoliated MoS₂ flakes are prepared into a thin film and then transferred onto the substrate; BP sensor is prepared with the mechanical exfoliation method. Just like none of two peas is exactly the same, none of the sensors is exactly like each other. Meanwhile, any small variations in the fabrication procedure might lead to a large difference in the final sensing performance. To address the challenges of device-to-device variations, rigorous quality control of sensor fabrication is needed, likely through process monitoring and automation. For example, automated printing process can be explored for the manufacture of these sensors.

Sensing performance (sensitivity, selectivity and stability): Meanwhile, understanding the sensing mechanism for the observed sensor signals is the key to optimize the sensor design, improve the sensing performance, and enhance the sensor reproducibility and reliability. Tuning the platform structure could be effective in reducing or eliminating the interference from the testing solution. For instance, a gate insulator or a passivate layer is needed for reducing or eliminating the signal change introduced by the electron transfer between metal ions and the channel material. But this leads to another challenge for the real application of FET water sensors--the thickness control of the passivation layer. On one hand, it needs to be thick enough to cover the sensing platform; on the other hand, a good detection sensitivity requires a thin enough Al₂O₃ layer because of the sensing range limited by the Debye length.

For the detection of contaminants in ultrapure water, the FET sensors are sensitive and selective to targeted metal ions. However, heavy metal ion detection in tap water or surface water is more complicated. Surface water usually has a very complex chemical composition

and carries inorganic ions, organic compounds and colloidal particles. These compositions would lead to large uncertainties in the detection, and possibly degrade the sensor's sensitivity and reduce its stability. Inevitably, the large number of these stray ions (e.g., Na⁺, Cl⁻ ions) and dissolved organic carbon would affect the sensing signal. Therefore, the ionic strength of the liquid media should be considered.²²²⁻²²³ For example, with the high ionic strength, the Debye length of the probe molecules becomes smaller because of the electrostatic screening effect. Thus, the strength of the bonded metal ions induced gating effect will be weakened, further leading to a weaker sensitivity. Consequently, it needs more careful consideration for the gate dielectric and probe selection during the sensor design. The thickness of the gate dielectric needs to balance between the sensing signal and the platform protection. And the probe size should be moderately small to decrease the distance between the adsorbed charged target analytes and the channel material and meet the Debye length requirement. In addition to the above-mentioned challenges, temperature impact on the sensor performance should be carefully addressed, since 2D semiconducting nanomaterials are sensitive to temperature variations in the environment. A possible research direction is to design a compensation method for the temperature variations. Further investigation is needed to construct a comprehensive calibration model considering the sensing performance as well as all possible influencing factors, including ambient environment (i.e., pH, temperature, humidity) and interference from other water components.

Continuous flow sensing: To enable the real application of FET sensors in the flowing water system, future research is needed to address a few challenges, including improving the reliability of the flowing water system set-up, resolving the effect of the convective transport on the adsorption of metal ions, and identifying the effect of flowing water on the chelation between the capturing probes and targeted ions. Eventually, integration of the FET sensor into

existing water equipment for inline, continuous monitoring of water contamination could be demonstrated.

REFERENCES

1. Radisavljevic, B.; Radenovic, A.; Brivio, J.; Giacometti, V.; Kis, A., Single-layer MoS₂ transistors. *Nature nanotechnology* **2011**, *6*, 147.
2. Järup, L., Hazards of heavy metal contamination. *British Medical Bulletin* **2003**, *68* (1), 167-182.
3. Singh, R.; Gautam, N.; Mishra, A.; Gupta, R., Heavy metals and living systems: An overview. *Indian Journal of Pharmacology* **2011**, *43* (3), 246-253.
4. Regulations - New Drinking Water Rules Announced. *Pollut Eng* **1999**, *31* (2), 14-15.
5. McIntyre, T., Phytoremediation of heavy metals from soils. *Advances in biochemical engineering/biotechnology* **2003**, *78*, 97-123.
6. Zahir, F.; Rizwi, S. J.; Haq, S. K.; Khan, R. H., Low dose mercury toxicity and human health. *Environmental Toxicology and Pharmacology* **2005**, *20* (2), 351-360.
7. Rice, D. C.; Gilbert, S. G., Effects of developmental exposure to methyl mercury on spatial and temporal visual function in monkeys. *Toxicology and applied pharmacology* **1990**, *102* (1), 151-63.
8. Krabbenhoft, D. P. R., David A., Mercury Contamination of Aquatic Ecosystems *U.S. GEOLOGICAL SURVEY Fact Sheet* **2013**, *Version 1.0* (216), 95.
9. Halim, C. E.; Scott, J. A.; Natawardaya, H.; Amal, R.; Beydoun, D.; Low, G., Comparison between acetic acid and landfill leachates for the leaching of Pb(II), Cd(II), As(V), and Cr(VI) from cementitious wastes. *Environmental science & technology* **2004**, *38* (14), 3977-83.
10. Mason, S. E.; Trainor, T. P.; Chaka, A. M., Hybridization-reactivity relationship in Pb(II) adsorption on α -Al₂O₃-water interfaces: A DFT Study. *The Journal of Physical Chemistry C* **2011**, *115* (10), 4008-4021.
11. <https://www.epa.gov/ground-water-and-drinking-water/basic-information-about-lead-drinking-water>.
12. Shukla, G. S.; Singhal, R. L., The present status of biological effects of toxic metals in the environment: lead, cadmium, and manganese. *Canadian journal of physiology and pharmacology* **1984**, *62* (8), 1015-31.
13. Walsh, A.; Watson, G. W., The origin of the stereochemically active Pb(II) lone pair: DFT calculations on PbO and PbS. *Journal of Solid State Chemistry* **2005**, *178* (5), 1422-1428.
14. Mays, D. E.; Hussam, A., Voltammetric methods for determination and speciation of inorganic arsenic in the environment—A review. *Analytica Chimica Acta* **2009**, *646* (1-2), 6-16.
15. Yokel, R. A.; Lasley, S. M.; Dorman, D. C., The Speciation of Metals in Mammals Influences Their Toxicokinetics and Toxicodynamics and Therefore Human Health Risk Assessment. *Journal of Toxicology and Environmental Health, Part B* **2006**, *9* (1), 63-85.
16. Wang, S.; Mulligan, C. N., Occurrence of arsenic contamination in Canada: sources, behavior and distribution. *The Science of the total environment* **2006**, *366* (2-3), 701-21.
17. Centre., I. G. R. A., Arsenic in Groundwater: A World Problem. **2009**.
18. Mandal, B. K.; Suzuki, K. T., Arsenic round the world: a review. *Talanta* **2002**, *58* (1), 201-235.
19. Wang, J. S.; Wai, C. M., Arsenic in Drinking Water—A Global Environmental Problem. *Journal of Chemical Education* **2004**, *81* (2), 207.
20. Hultgren, R., Gingrich, N. S. & Warren, B. E. , The atomic distribution in red and black phosphorus and the crystal structure of black phosphorus. *J. Chem. Phys.* **1935**, *3*, 351-355.
21. Puk, R.; Weber, J. H., Determination of Mercury(Ii), Methylmercury Cation, Dimethylmercury and Diethylmercury by Hydride Generation, Cryogenic Trapping and Atomic-Absorption Spectrometric Detection. *Analytica Chimica Acta* **1994**, *292* (1-2), 175-183.

22. Bhat, K. R.; Arunachalam, J.; Yegnasubramanian, S.; Gangadharan, S., Trace elements in hair and environmental exposure. *The Science of the total environment* **1982**, *22* (2), 169-78.
23. Qing, Z. H.; He, X. X.; Wang, K. M.; Zou, Z.; Yang, X.; Huang, J.; Yan, G. P., Colorimetric multiplexed analysis of mercury and silver ions by using a unimolecular DNA probe and unmodified gold nanoparticles. *Anal Methods-Uk* **2012**, *4* (10), 3320-3325.
24. Zhang, J.; Mao, L. L.; Yang, G. P.; Gao, X. C.; Tang, X. L., Determination of Trace Mercury in Wastewater by a Flow Injection Analysis Composed of Immobilized Ionic Liquid Enrichment and Colorimetric Detection. *Spectrosc Spect Anal* **2010**, *30* (7), 1979-1982.
25. Perez-Hernandez, J.; Albero, J.; Correig, X.; Llobet, E.; Palomares, E., Multivariate calibration analysis of colorimetric mercury sensing using a molecular probe. *Analytica Chimica Acta* **2009**, *633* (2), 173-180.
26. Watson, C. M.; Dwyer, D. J.; Andle, J. C.; Bruce, A. E.; Bruce, M. R. M., Stripping analyses of mercury using gold electrodes: Irreversible adsorption of mercury. *Anal Chem* **1999**, *71* (15), 3181-3186.
27. Zhang, Y.; Zeng, G. M.; Tang, L.; Li, Y. P.; Chen, Z. M.; Huang, G. H., Quantitative detection of trace mercury in environmental media using a three-dimensional electrochemical sensor with an anionic intercalator. *Rsc Adv* **2014**, *4* (36), 18485-18492.
28. Yang, S. J.; Meng, D. L.; Sun, J. H.; Hou, W. P.; Ding, Y. B.; Jiang, S. D.; Huang, Y.; Huang, Y.; Geng, J. X., Enhanced electrochemical response for mercury ion detection based on poly(3-hexylthiophene) hybridized with multi-walled carbon nanotubes. *Rsc Adv* **2014**, *4* (48), 25051-25056.
29. Luo, T.; He, M.; Gao, C.; Liu, J. H.; Huang, X. J., Specific size-matching strategy for electrochemical selective and sensitive detection of mercury(II) based on a three-dimensional-gap-net in a Au-thiol coordination polymer. *Electrochem Commun* **2014**, *42*, 26-29.
30. Bloxham, M. J.; Hill, S. J.; Worsfold, P. J., Determination of mercury in filtered sea-water by flow injection with on-line oxidation and atomic fluorescence spectrometric detection. *J Anal Atom Spectrom* **1996**, *11* (7), 511-514.
31. Boyanov, M. I.; Kmetko, J.; Shibata, T.; Datta, A.; Dutta, P.; Bunker, B. A., Mechanism of Pb Adsorption to Fatty Acid Langmuir Monolayers Studied by X-ray Absorption Fine Structure Spectroscopy. *The Journal of Physical Chemistry B* **2003**, *107* (36), 9780-9788.
32. Beqa, L.; Singh, A. K.; Khan, S. A.; Senapati, D.; Arumugam, S. R.; Ray, P. C., Gold nanoparticle-based simple colorimetric and ultrasensitive dynamic light scattering assay for the selective detection of Pb(II) from paints, plastics, and water samples. *ACS applied materials & interfaces* **2011**, *3* (3), 668-73.
33. Balaji, T.; El-Safty, S. A.; Matsunaga, H.; Hanaoka, T.; Mizukami, F., Optical sensors based on nanostructured cage materials for the detection of toxic metal ions. *Angewandte Chemie (International ed. in English)* **2006**, *45* (43), 7202-8.
34. Stroganov, V.; Ryabchun, A.; Bobrovsky, A.; Shibaev, V., A novel type of crown ether-containing metal ions optical sensors based on polymer-stabilized cholesteric liquid crystalline films. *Macromolecular rapid communications* **2012**, *33* (21), 1875-81.
35. Sener, G.; Uzun, L.; Denizli, A., Colorimetric sensor array based on gold nanoparticles and amino acids for identification of toxic metal ions in water. *ACS applied materials & interfaces* **2014**, *6* (21), 18395-400.
36. Wang, X. C.; Liu, X. D.; Yang, Y. L.; Shen, Q. H.; Luo, S. G.; Li, Q., Application of Rhodamine-Based Fluorescence Chemosensor in Heavy Metal Ions and Transition Metal Ions Detection. *Spectrosc Spect Anal* **2010**, *30* (10), 2693-2699.
37. Margheri, G.; Giorgetti, E.; Marsili, P.; Zoppi, A.; Lascialfari, L.; Cicchi, S., Metal-clad optical waveguide fluorescence device for the detection of heavy metal ions. *OPTICE* **2014**, *53* (7), 071816-071816.

38. Li, M.; Wang, Q.; Shi, X.; Hornak, L. A.; Wu, N., Detection of mercury(II) by quantum dot/DNA/gold nanoparticle ensemble based nanosensor via nanometal surface energy transfer. *Anal Chem* **2011**, *83* (18), 7061-5.
39. Vazquez-Gonzalez, M.; Carrillo-Carrion, C., Analytical strategies based on quantum dots for heavy metal ions detection. *Journal of biomedical optics* **2014**, *19* (10), 101503.
40. Chen, J.; Zheng, A.; Gao, Y.; He, C.; Wu, G.; Chen, Y.; Kai, X.; Zhu, C., Functionalized CdS quantum dots-based luminescence probe for detection of heavy and transition metal ions in aqueous solution. *Spectrochimica acta. Part A, Molecular and biomolecular spectroscopy* **2008**, *69* (3), 1044-52.
41. Aragay, G.; Pons, J.; Merkoci, A., Recent trends in macro-, micro-, and nanomaterial-based tools and strategies for heavy-metal detection. *Chemical reviews* **2011**, *111* (5), 3433-58.
42. Buffle, J.; Tercier-Waeber, M. L., Voltammetric environmental trace-metal analysis and speciation: from laboratory to in situ measurements. *TrAC Trends in Analytical Chemistry* **2005**, *24* (3), 172-191.
43. Yong, Y.; Shigemasha, M.; Masayuki, N.; Jianlin, S.; Weiming, H., One-dimensional self-assembly of gold nanoparticles for tunable surface plasmon resonance properties. *Nanotechnology* **2006**, *17* (11), 2821.
44. Li, M.; Zhou, X.; Ding, W.; Guo, S.; Wu, N., Fluorescent aptamer-functionalized graphene oxide biosensor for label-free detection of mercury(II). *Biosensors and Bioelectronics* **2013**, *41*, 889-893.
45. Economou, A.; Fielden, P. R., Mercury film electrodes: developments, trends and potentialities for electroanalysis. *The Analyst* **2003**, *128* (3), 205-12.
46. Gao, C.; Yu, X.-Y.; Xu, R.-X.; Liu, J.-H.; Huang, X.-J., AlOOH-Reduced Graphene Oxide Nanocomposites: One-Pot Hydrothermal Synthesis and Their Enhanced Electrochemical Activity for Heavy Metal Ions. *ACS applied materials & interfaces* **2012**, *4* (9), 4672-4682.
47. Field-effect transistor. https://en.wikipedia.org/wiki/Field-effect_transistor.
48. Zhou, G.; Chang, J.; Pu, H.; Shi, K.; Mao, S.; Sui, X.; Ren, R.; Cui, S.; Chen, J., Ultrasensitive Mercury Ion Detection Using DNA-Functionalized Molybdenum Disulfide Nanosheet/Gold Nanoparticle Hybrid Field-Effect Transistor Device. *ACS Sensors* **2016**, *1* (3), 295-302.
49. Mao, S.; Chang, J.; Zhou, G.; Chen, J., Nanomaterial-enabled Rapid Detection of Water Contaminants. *Small (Weinheim an der Bergstrasse, Germany)* **2015**, *11* (40), 5336-59.
50. Chang, J.; Zhou, G.; Gao, X.; Mao, S.; Cui, S.; Ocola, L. E.; Yuan, C.; Chen, J., Real-time detection of mercury ions in water using a reduced graphene oxide/DNA field-effect transistor with assistance of a passivation layer. *Sensing and Bio-Sensing Research* **2015**, *5*, 97-104.
51. Chang, J.; Zhou, G.; Christensen, E. R.; Heideman, R.; Chen, J., Graphene-based sensors for detection of heavy metals in water: a review. *Analytical and bioanalytical chemistry* **2014**, *406* (16), 3957-75.
52. Zhou, G.; Chang, J.; Cui, S.; Pu, H.; Wen, Z.; Chen, J., Real-Time, Selective Detection of Pb²⁺ in Water Using a Reduced Graphene Oxide/Gold Nanoparticle Field-Effect Transistor Device. *ACS applied materials & interfaces* **2014**, *6* (21), 19235-19241.
53. Gao, X. P. A.; Zheng, G.; Lieber, C. M., Subthreshold Regime has the Optimal Sensitivity for Nanowire FET Biosensors. *Nano Letters* **2009**, *10* (2), 547-552.
54. Zhou, J.; Barbara, P.; Paranjape, M., Novel in-situ decoration of single-walled carbon nanotube transistors with metal nanoparticles. *Journal of nanoscience and nanotechnology* **2010**, *10* (6), 3890-4.
55. Sudibya, H. G.; He, Q.; Zhang, H.; Chen, P., Electrical Detection of Metal Ions Using Field-Effect Transistors Based on Micropatterned Reduced Graphene Oxide Films. *ACS Nano* **2011**, *5* (3), 1990-1994.
56. Li, B. R.; Chen, C. W.; Yang, W. L.; Lin, T. Y.; Pan, C. Y.; Chen, Y. T., Biomolecular recognition with a sensitivity-enhanced nanowire transistor biosensor. *Biosensors & bioelectronics* **2013**, *45*, 252-9.

57. Sudibya, H. G.; He, Q.; Zhang, H.; Chen, P., Electrical detection of metal ions using field-effect transistors based on micropatterned reduced graphene oxide films. *Acs Nano* **2011**, *5* (3), 1990-4.
58. Sun, Z.; James, D. K.; Tour, J. M., Graphene Chemistry: Synthesis and Manipulation. *The Journal of Physical Chemistry Letters* **2011**, *2* (19), 2425-2432.
59. Lu, G. H.; Ocola, L. E.; Chen, J. H., Reduced graphene oxide for room-temperature gas sensors. *Nanotechnology* **2009**, *20* (44).
60. Avouris, P., Graphene: Electronic and Photonic Properties and Devices. *Nano Lett* **2010**.
61. Chang, J.; Mao, S.; Zhang, Y.; Cui, S.; Zhou, G.; Wu, X.; Yang, C. H.; Chen, J., Ultrasonic-assisted self-assembly of monolayer graphene oxide for rapid detection of Escherichia coli bacteria. *Nanoscale* **2013**, *5* (9), 3620-6.
62. Novoselov, K. S.; Geim, A. K.; Morozov, S. V.; Jiang, D.; Zhang, Y.; Dubonos, S. V.; Grigorieva, I. V.; Firsov, A. A., Electric field effect in atomically thin carbon films. *Science* **2004**, *306* (5696), 666-9.
63. M, J., Nobel prize in physics. . *Chem Eng News Arch* **2010**, *88* (41), 8.
64. Geim, A. K., Graphene: status and prospects. *Science* **2009**, *324* (5934), 1530-4.
65. Fitzer, E.; Kochling, K. H.; Boehm, H. P.; Marsh, H., Recommended terminology for the description of carbon as a solid (IUPAC Recommendations 1995). In *Pure and Applied Chemistry*, 1995; Vol. 67, p 473.
66. Salas, E. C.; Sun, Z.; Lüttge, A.; Tour, J. M., Reduction of Graphene Oxide via Bacterial Respiration. *ACS Nano* **2010**, *4* (8), 4852-4856.
67. Stankovich, S.; Piner, R. D.; Chen, X.; Wu, N.; Nguyen, S. T.; Ruoff, R. S., Stable aqueous dispersions of graphitic nanoplatelets via the reduction of exfoliated graphite oxide in the presence of poly(sodium 4-styrenesulfonate). *Journal of Materials Chemistry* **2006**, *16* (2), 155-158.
68. Gilje, S.; Han, S.; Wang, M.; Wang, K. L.; Kaner, R. B., A Chemical Route to Graphene for Device Applications. *Nano Letters* **2007**, *7* (11), 3394-3398.
69. Park, S.; Ruoff, R. S., Chemical methods for the production of graphenes. *Nat Nano* **2009**, *4* (4), 217-224.
70. Hilder, M.; Winther-Jensen, B.; Li, D.; Forsyth, M.; MacFarlane, D. R., Direct electro-deposition of graphene from aqueous suspensions. *Physical Chemistry Chemical Physics* **2011**, *13* (20), 9187-9193.
71. McAllister, M. J.; Li, J.-L.; Adamson, D. H.; Schniepp, H. C.; Abdala, A. A.; Liu, J.; Herrera-Alonso, M.; Milius, D. L.; Car, R.; Prud'homme, R. K.; Aksay, I. A., Single Sheet Functionalized Graphene by Oxidation and Thermal Expansion of Graphite. *Chemistry of Materials* **2007**, *19* (18), 4396-4404.
72. Cote, L. J.; Cruz-Silva, R.; Huang, J., Flash Reduction and Patterning of Graphite Oxide and Its Polymer Composite. *Journal of the American Chemical Society* **2009**, *131* (31), 11027-11032.
73. Quinlan, R. A.; Javier, A.; Foos, E. E.; Buckley, L.; Zhu, M.; Hou, K.; Widenkvist, E.; Drees, M.; Jansson, U.; Holloway, B. C., Transfer of carbon nanosheet films to nongrowth, zero thermal budget substrates. *Journal of Vacuum Science & Technology B* **2011**, *29* (3), 030602.
74. Rao, C. N. R.; Sood, A. K.; Subrahmanyam, K. S.; Govindaraj, A., Graphene: The New Two-Dimensional Nanomaterial. *Angewandte Chemie International Edition* **2009**, *48* (42), 7752-7777.
75. Bao, Q.; Loh, K. P., Graphene Photonics, Plasmonics, and Broadband Optoelectronic Devices. *ACS Nano* **2012**, *6* (5), 3677-3694.
76. Hong, S.; Myung, S., Nanotube Electronics: A flexible approach to mobility. *Nat Nano* **2007**, *2* (4), 207-208.
77. Sridhar, V.; Kim, H.-J.; Jung, J.-H.; Lee, C.; Park, S.; Oh, I.-K., Defect-Engineered Three-Dimensional Graphene–Nanotube–Palladium Nanostructures with Ultrahigh Capacitance. *ACS Nano* **2012**, *6* (12), 10562-10570.
78. Chen, S.; Wu, Q.; Mishra, C.; Kang, J.; Zhang, H.; Cho, K.; Cai, W.; Balandin, A. A.; Ruoff, R. S., Thermal conductivity of isotopically modified graphene. *Nat Mater* **2012**, *11* (3), 203-207.

79. Bolotin, K. I.; Sikes, K. J.; Jiang, Z.; Klima, M.; Fudenberg, G.; Hone, J.; Kim, P.; Stormer, H. L., Ultrahigh electron mobility in suspended graphene. *Solid State Communications* **2008**, *146* (9–10), 351-355.
80. Kim, K. S.; Zhao, Y.; Jang, H.; Lee, S. Y.; Kim, J. M.; Kim, K. S.; Ahn, J.-H.; Kim, P.; Choi, J.-Y.; Hong, B. H., Large-scale pattern growth of graphene films for stretchable transparent electrodes. *Nature* **2009**, *457* (7230), 706-710.
81. Chen, J.; Bi, H.; Sun, S.; Tang, Y.; Zhao, W.; Lin, T.; Wan, D.; Huang, F.; Zhou, X.; Xie, X.; Jiang, M., Highly Conductive and Flexible Paper of 1D Silver-Nanowire-Doped Graphene. *ACS applied materials & interfaces* **2013**, *5* (4), 1408-1413.
82. Joshi, R. K.; Gomez, H.; Alvi, F.; Kumar, A., Graphene Films and Ribbons for Sensing of O₂, and 100 ppm of CO and NO₂ in Practical Conditions. *The Journal of Physical Chemistry C* **2010**, *114* (14), 6610-6613.
83. Agarwal, S.; Zhou, X. Z.; Ye, F.; He, Q. Y.; Chen, G. C. K.; Soo, J.; Boey, F.; Zhang, H.; Chen, P., Interfacing Live Cells with Nanocarbon Substrates. *Langmuir* **2010**, *26* (4), 2244-2247.
84. Wang, Q. H.; Kalantar-Zadeh, K.; Kis, A.; Coleman, J. N.; Strano, M. S., Electronics and optoelectronics of two-dimensional transition metal dichalcogenides. *Nature nanotechnology* **2012**, *7* (11), 699-712.
85. Bae, S.; Kim, H.; Lee, Y.; Xu, X. F.; Park, J. S.; Zheng, Y.; Balakrishnan, J.; Lei, T.; Kim, H. R.; Song, Y. I.; Kim, Y. J.; Kim, K. S.; Ozyilmaz, B.; Ahn, J. H.; Hong, B. H.; Iijima, S., Roll-to-roll production of 30-inch graphene films for transparent electrodes. *Nature nanotechnology* **2010**, *5* (8), 574-578.
86. Li, X. S.; Cai, W. W.; An, J. H.; Kim, S.; Nah, J.; Yang, D. X.; Piner, R.; Velamakanni, A.; Jung, I.; Tutuc, E.; Banerjee, S. K.; Colombo, L.; Ruoff, R. S., Large-Area Synthesis of High-Quality and Uniform Graphene Films on Copper Foils. *Science* **2009**, *324* (5932), 1312-1314.
87. Zhan, Y. J.; Liu, Z.; Najmaei, S.; Ajayan, P. M.; Lou, J., Large-Area Vapor-Phase Growth and Characterization of MoS₂ Atomic Layers on a SiO₂ Substrate. *Small (Weinheim an der Bergstrasse, Germany)* **2012**, *8* (7), 966-971.
88. Eda, G.; Yamaguchi, H.; Voiry, D.; Fujita, T.; Chen, M.; Chhowalla, M., Photoluminescence from chemically exfoliated MoS₂. *Nano Lett* **2011**, *11* (12), 5111-6.
89. Radisavljevic, B.; Radenovic, A.; Brivio, J.; Giacometti, V.; Kis, A., Single-layer MoS₂ transistors. *Nature nanotechnology* **2011**, *6* (3), 147-150.
90. Mak, K. F.; Lee, C.; Hone, J.; Shan, J.; Heinz, T. F., Atomically Thin MoS₂: A New Direct-Gap Semiconductor. *Phys Rev Lett* **2010**, *105* (13).
91. Lee, C.; Yan, H.; Brus, L. E.; Heinz, T. F.; Hone, J.; Ryu, S., Anomalous lattice vibrations of single- and few-layer MoS₂. *ACS Nano* **2010**, *4* (5), 2695-700.
92. Zhou, K. G.; Mao, N. N.; Wang, H. X.; Peng, Y.; Zhang, H. L., A mixed-solvent strategy for efficient exfoliation of inorganic graphene analogues. *Angewandte Chemie (International ed. in English)* **2011**, *50* (46), 10839-42.
93. Lee, Y.-H.; Zhang, X.-Q.; Zhang, W.; Chang, M.-T.; Lin, C.-T.; Chang, K.-D.; Yu, Y.-C.; Wang, J. T.-W.; Chang, C.-S.; Li, L.-J.; Lin, T.-W., Synthesis of Large-Area MoS₂ Atomic Layers with Chemical Vapor Deposition. *Advanced Materials* **2012**, *24* (17), 2320-2325.
94. Park, W.; Baik, J.; Kim, T. Y.; Cho, K.; Hong, W. K.; Shin, H. J.; Lee, T., Photoelectron spectroscopic imaging and device applications of large-area patternable single-layer MoS₂ synthesized by chemical vapor deposition. *ACS Nano* **2014**, *8* (5), 4961-8.
95. Lauritsen, J. V.; Kibsgaard, J.; Helveg, S.; Topsoe, H.; Clausen, B. S.; Laegsgaard, E.; Besenbacher, F., Size-dependent structure of MoS₂ nanocrystals. *Nature nanotechnology* **2007**, *2* (1), 53-8.
96. Wientges, J.; Putz, J.; Giege, R.; Florentz, C.; Schwienhorst, A., Selection of viral RNA-derived tRNA-like structures with improved valylation activities. *Biochemistry* **2000**, *39* (20), 6207-18.

97. Li, L.; Yu, Y.; Ye, G. J.; Ge, Q.; Ou, X.; Wu, H.; Feng, D.; Chen, X. H.; Zhang, Y., Black phosphorus field-effect transistors. *Nature nanotechnology* **2014**, *9*, 372.
98. Sandra, H. A.; Maruthi, N. Y.; Weinan, Z.; Joonseok, K.; Sushant, S. S.; Avinash, P. N.; Deji, A., Characterization and sonochemical synthesis of black phosphorus from red phosphorus. *2D Materials* **2016**, *3* (1), 014007.
99. Lukatskaya, M. R.; Mashtalir, O.; Ren, C. E.; Dall'Agnese, Y.; Rozier, P.; Taberna, P. L.; Naguib, M.; Simon, P.; Barsoum, M. W.; Gogotsi, Y., Cation Intercalation and High Volumetric Capacitance of Two-Dimensional Titanium Carbide. *Science* **2013**, *341* (6153), 1502-1505.
100. Dai, J.; Zeng, X. C., Bilayer Phosphorene: Effect of Stacking Order on Bandgap and Its Potential Applications in Thin-Film Solar Cells. *J Phys Chem Lett* **2014**, *5* (7), 1289-93.
101. Li, L.; Yu, Y.; Ye, G. J.; Ge, Q.; Ou, X.; Wu, H.; Feng, D.; Chen, X. H.; Zhang, Y., Black phosphorus field-effect transistors. *Nat Nano* **2014**, *9* (5), 372-377.
102. Cui, S.; Pu, H.; Wells, S. A.; Wen, Z.; Mao, S.; Chang, J.; Hersam, M. C.; Chen, J., Ultrahigh sensitivity and layer-dependent sensing performance of phosphorene-based gas sensors. *Nat Commun* **2015**, *6*.
103. Na, J.; Lee, Y. T.; Lim, J. A.; Hwang, D. K.; Kim, G.-T.; Choi, W. K.; Song, Y.-W., Few-Layer Black Phosphorus Field-Effect Transistors with Reduced Current Fluctuation. *ACS Nano* **2014**, *8* (11), 11753-11762.
104. Illarionov, Y. Y.; Walzl, M.; Rzepa, G.; Knobloch, T.; Kim, J. S.; Akinwande, D.; Grasser, T., Highly-stable black phosphorus field-effect transistors with low density of oxide traps. *npj 2D Materials and Applications* **2017**, *1* (1), 23.
105. Wood, J. D.; Wells, S. A.; Jariwala, D.; Chen, K.-S.; Cho, E.; Sangwan, V. K.; Liu, X.; Lauhon, L. J.; Marks, T. J.; Hersam, M. C., Effective Passivation of Exfoliated Black Phosphorus Transistors against Ambient Degradation. *Nano Letters* **2014**, *14* (12), 6964-6970.
106. Churchill, H. O.; Jariillo-Herrero, P., Two-dimensional crystals: phosphorus joins the family. *Nature nanotechnology* **2014**, *9* (5), 330-1.
107. Chen, K.; Lu, G.; Chang, J.; Mao, S.; Yu, K.; Cui, S.; Chen, J., Hg(II) Ion Detection Using Thermally Reduced Graphene Oxide Decorated with Functionalized Gold Nanoparticles. *Anal Chem* **2012**, *84* (9), 4057-4062.
108. Mao, S.; Pu, H.; Chang, J.; Sui, X.; Zhou, G.; Ren, R.; Chen, Y.; Chen, J., Ultrasensitive detection of orthophosphate ions with reduced graphene oxide/ferritin field-effect transistor sensors. *Environmental Science: Nano* **2017**, *4* (4), 856-863.
109. Wen, Y.; Li, F. Y.; Dong, X.; Zhang, J.; Xiong, Q.; Chen, P., The Electrical Detection of Lead Ions Using Gold-Nanoparticle- and DNAzyme-Functionalized Graphene Device. *Advanced Healthcare Materials* **2013**, *2* (2), 271-274.
110. Huang, Y.; Dong, X.; Liu, Y.; Li, L.-J.; Chen, P., Graphene-based biosensors for detection of bacteria and their metabolic activities. *Journal of Materials Chemistry* **2011**, *21* (33), 12358-12362.
111. Li, P.; Zhang, D.; Sun, Y. e.; Chang, H.; Liu, J.; Yin, N., Towards intrinsic MoS₂ devices for high performance arsenite sensing. *Applied Physics Letters* **2016**, *109* (6), 063110.
112. Sarkar, D.; Liu, W.; Xie, X.; Anselmo, A. C.; Mitragotri, S.; Banerjee, K., MoS₂ Field-Effect Transistor for Next-Generation Label-Free Biosensors. *ACS Nano* **2014**, *8* (4), 3992-4003.
113. Wang, L.; Wang, Y.; Wong, J. I.; Palacios, T.; Kong, J.; Yang, H. Y., Functionalized MoS₂ Nanosheet-Based Field-Effect Biosensor for Label-Free Sensitive Detection of Cancer Marker Proteins in Solution. *Small (Weinheim an der Bergstrasse, Germany)* **2014**, *10* (6), 1101-1105.
114. Naylor, C. H.; Kybert, N. J.; Schneier, C.; Xi, J.; Romero, G.; Saven, J. G.; Liu, R.; Johnson, A. T. C., Scalable Production of Molybdenum Disulfide Based Biosensors. *ACS Nano* **2016**, *10* (6), 6173-6179.

115. Lee, D.-W.; Lee, J.; Sohn, I. Y.; Kim, B.-Y.; Son, Y. M.; Bark, H.; Jung, J.; Choi, M.; Kim, T. H.; Lee, C.; Lee, N.-E., Field-effect transistor with a chemically synthesized MoS₂ sensing channel for label-free and highly sensitive electrical detection of DNA hybridization. *Nano Research* **2015**, *8* (7), 2340-2350.
116. Zhou, G.; Pu, H.; Chang, J.; Sui, X.; Mao, S.; Chen, J., Real-time electronic sensor based on black phosphorus/Au NPs/DTT hybrid structure: Application in arsenic detection. *Sensors and Actuators B: Chemical* **2018**, *257*, 214-219.
117. Chen, Y.; Ren, R.; Pu, H.; Chang, J.; Mao, S.; Chen, J., Field-effect transistor biosensors with two-dimensional black phosphorus nanosheets. *Biosensors and Bioelectronics* **2017**, *89* (Part 1), 505-510.
118. Li, P.; Zhang, D.; Liu, J.; Chang, H.; Sun, Y. e.; Yin, N., Air-Stable Black Phosphorus Devices for Ion Sensing. *ACS applied materials & interfaces* **2015**, *7* (44), 24396-24402.
119. Yasaei, P.; Behranginia, A.; Foroozan, T.; Asadi, M.; Kim, K.; Khalili-Araghi, F.; Salehi-Khojin, A., Stable and Selective Humidity Sensing Using Stacked Black Phosphorus Flakes. *ACS Nano* **2015**, *9* (10), 9898-9905.
120. El-Safty, S. A.; Shenashen, M. A.; Shahat, A., Tailor-made micro-object optical sensor based on mesoporous pellets for visual monitoring and removal of toxic metal ions from aqueous media. *Small (Weinheim an der Bergstrasse, Germany)* **2013**, *9* (13), 2288-96.
121. Kumeria, T.; Rahman, M. M.; Santos, A.; Ferre-Borrull, J.; Marsal, L. F.; Losic, D., Nanoporous anodic alumina rugate filters for sensing of ionic mercury: toward environmental point-of-analysis systems. *ACS applied materials & interfaces* **2014**, *6* (15), 12971-8.
122. Halim, C. E.; Scott, J. A.; Natawardaya, H.; Amal, R.; Beydoun, D.; Low, G., Comparison between Acetic Acid and Landfill Leachates for the Leaching of Pb(II), Cd(II), As(V), and Cr(VI) from Cementitious Wastes. *Environmental science & technology* **2004**, *38* (14), 3977-3983.
123. Yu, K. H.; Lu, G. H.; Mao, S.; Chen, K. H.; Kim, H.; Wen, Z. H.; Chen, J. H., Selective Deposition of CdSe Nanoparticles on Reduced Graphene Oxide to Understand Photoinduced Charge Transfer in Hybrid Nanostructures. *Acs Appl Mater Inter* **2011**, *3* (7), 2703-2709.
124. Marcano, D. C.; Kosynkin, D. V.; Berlin, J. M.; Sinitskii, A.; Sun, Z. Z.; Slesarev, A.; Alemany, L. B.; Lu, W.; Tour, J. M., Improved Synthesis of Graphene Oxide. *ACS Nano* **2010**, *4* (8), 4806-4814.
125. Stankovich, S.; Piner, R. D.; Chen, X. Q.; Wu, N. Q.; Nguyen, S. T.; Ruoff, R. S., Stable Aqueous Dispersions of Graphitic Nanoplatelets Via the Reduction of Exfoliated Graphite Oxide in the Presence of Poly(sodium 4-styrenesulfonate). *J Mater Chem* **2006**, *16* (2), 155-158.
126. Walsh, A.; Watson, G. W., The Origin of the Stereochemically Active Pb(II) Lone Pair: DFT Calculations on PbO and PbS. *J Solid State Chem* **2005**, *178* (5), 1422-1428.
127. Elliott, P. R. From the Science of Nanorod Growth to Low Temperature Metallic Attachment. University of Connecticut - Storrs, 2017.
128. Akhavan, O., The Effect of Heat Treatment on Formation of Graphene Thin Films from Graphene Oxide Nanosheets. *Carbon* **2010**, *48* (2), 509-519.
129. Ghosh, T.; Biswas, C.; Oh, J.; Arabale, G.; Hwang, T.; Luong, N. D.; Jin, M.; Lee, Y. H.; Nam, J. D., Solution-Processed Graphite Membrane from Reassembled Graphene Oxide. *Chem Mater* **2012**, *24* (3), 594-599.
130. Carro, P.; Torres, D.; Diaz, R.; Salvarezza, R. C.; Illas, F., Mechanisms of Defect Generation and Clustering in CH₃S Self-Assembled Monolayers on Au(111). *J Phys Chem Lett* **2012**, *3* (16), 2159-2163.
131. Fowler, J. D.; Virji, S.; Kaner, R. B.; Weiller, B. H., Hydrogen Detection by Polyaniline Nanofibers on Gold and Platinum Electrodes. *J Phys Chem C* **2009**, *113* (16), 6444-6449.
132. Gomez-Navarro, C.; Weitz, R. T.; Bittner, A. M.; Scolari, M.; Mews, A.; Burghard, M.; Kern, K., Electronic Transport Properties of Individual Chemically Reduced Graphene Oxide Sheets. *Nano Lett* **2007**, *7* (11), 3499-3503.

133. Huang, C. C.; Chang, H. T., Selective Gold-nanoparticle-based "turn-on" Fluorescent Sensors for Detection of Mercury(II) in Aqueous Solution. *Anal Chem* **2006**, *78* (24), 8332-8338.
134. Zeng, S. W.; Yong, K. T.; Roy, I.; Dinh, X. Q.; Yu, X.; Luan, F., A Review on Functionalized Gold Nanoparticles for Biosensing Applications. *Plasmonics* **2011**, *6* (3), 491-506.
135. Tehrani, Z. A.; Jamshidi, Z.; Javan, M. J.; Fattahi, A., Interactions of Glutathione Tripeptide with Gold Cluster: Influence of Intramolecular Hydrogen Bond on Complexation Behavior. *J Phys Chem A* **2012**, *116* (17), 4338-4347.
136. Beqa, L.; Singh, A. K.; Khan, S. A.; Senapati, D.; Arumugam, S. R.; Ray, P. C., Gold Nanoparticle-Based Simple Colorimetric and Ultrasensitive Dynamic Light Scattering Assay for the Selective Detection of Pb(II) from Paints, Plastics, and Water Samples. *Acs Appl Mater Inter* **2011**, *3* (3), 668-673.
137. Chai, F.; Wang, C. A.; Wang, T. T.; Li, L.; Su, Z. M., Colorimetric Detection of Pb²⁺ Using Glutathione Functionalized Gold Nanoparticles. *Acs Appl Mater Inter* **2010**, *2* (5), 1466-1470.
138. Mah, V.; Jalilehvand, F., Lead(II) Complex Formation with Glutathione. *Inorg Chem* **2012**, *51* (11), 6285-6298.
139. Kwon, K. C.; Choi, K. S.; Kim, B. J.; Lee, J. L.; Kim, S. Y., Work-Function Decrease of Graphene Sheet Using Alkali Metal Carbonates. *J Phys Chem C* **2012**, *116* (50), 26586-26591.
140. Fowler, J. D.; Allen, M. J.; Tung, V. C.; Yang, Y.; Kaner, R. B.; Weiller, B. H., Practical Chemical Sensors from Chemically Derived Graphene. *Acs Nano* **2009**, *3* (2), 301-306.
141. Ghosh, T.; Biswas, C.; Oh, J.; Arabale, G.; Hwang, T.; Luong, N. D.; Jin, M.; Lee, Y. H.; Nam, J.-D., Solution-Processed Graphite Membrane from Reassembled Graphene Oxide. *Chemistry of Materials* **2011**, *24* (3), 594-599.
142. Li, M.; Zhou, X.; Guo, S.; Wu, N., Detection of lead (II) with a "turn-on" fluorescent biosensor based on energy transfer from CdSe/ZnS quantum dots to graphene oxide. *Biosensors and Bioelectronics* **2013**, *43* (0), 69-74.
143. Li, M.; Zhou, X. J.; Guo, S. W.; Wu, N. Q., Detection of Lead (II) with a "turn-on" Fluorescent Biosensor Based on Energy Transfer from CdSe/ZnS Quantum Dots to Graphene Oxide. *Biosensors & bioelectronics* **2013**, *43*, 69-74.
144. Regulations - New Drinking Water Rules Announced. *Pollut Eng* **1999**, *31* (2), 14-15.
145. Yu, Y. J.; Zhao, Y.; Ryu, S.; Brus, L. E.; Kim, K. S.; Kim, P., Tuning the Graphene Work Function by Electric Field Effect. *Nano Lett* **2009**, *9* (10), 3430-3434.
146. Shahidi, F.; Chavan, U. D.; Naczki, M.; Amarowicz, R., Nutrient Distribution and Phenolic Antioxidants in Air-classified Fractions of Beach Pea (*Lathyrus maritimus* L.). *J Agr Food Chem* **2001**, *49* (2), 926-933.
147. Wang, B.; Liao, L. M.; Huang, Q. H.; Cheng, Y. X., Adsorption Behaviors of Benzoic Acid by Carboxyl Methyl Konjac Glucomannan Gel Microspheres Cross-Linked with Fe³⁺. *J Chem Eng Data* **2012**, *57* (1), 72-77.
148. Li, J.; Lu, Y., A Highly Sensitive and Selective Catalytic DNA Biosensor for Lead Ions. *J Am Chem Soc* **2000**, *122* (42), 10466-10467.
149. Gao, C.; Yu, X. Y.; Xu, R. X.; Liu, J. H.; Huang, X. J., AIOOH-Reduced Graphene Oxide Nanocomposites: One-Pot Hydrothermal Synthesis and Their Enhanced Electrochemical Activity for Heavy Metal Ions. *Acs Appl Mater Inter* **2012**, *4* (9), 4672-4682.
150. Georgakilas, V.; Otyepka, M.; Bourlinos, A. B.; Chandra, V.; Kim, N.; Kemp, K. C.; Hobza, P.; Zboril, R.; Kim, K. S., Functionalization of Graphene: Covalent and Non-Covalent Approaches, Derivatives and Applications. *Chemical reviews* **2012**, *112* (11), 6156-6214.
151. Sudibya, H. G.; He, Q. Y.; Zhang, H.; Chen, P., Electrical Detection of Metal Ions Using Field-Effect Transistors Based on Micropatterned Reduced Graphene Oxide Films. *ACS Nano* **2011**, *5* (3), 1990-1994.

152. Jayasena, S. D., Aptamers: An Emerging Class of Molecules that Rival Antibodies in Diagnostics. *Clin Chem* **1999**, *45* (9), 1628-1650.
153. Willemse, C. M.; Tlhomelang, K.; Jahed, N.; Baker, P. G.; Iwuoha, E. I., Metallo-graphene Nanocomposite Electrocatalytic Platform for the Determination of Toxic Metal Ions. *Sensors* **2011**, *11* (4), 3970-87.
154. Coleman, J. N.; Lotya, M.; O'Neill, A.; Bergin, S. D.; King, P. J.; Khan, U.; Young, K.; Gaucher, A.; De, S.; Smith, R. J.; Shvets, I. V.; Arora, S. K.; Stanton, G.; Kim, H. Y.; Lee, K.; Kim, G. T.; Duesberg, G. S.; Hallam, T.; Boland, J. J.; Wang, J. J.; Donegan, J. F.; Grunlan, J. C.; Moriarty, G.; Shmeliov, A.; Nicholls, R. J.; Perkins, J. M.; Grieveson, E. M.; Theuwissen, K.; McComb, D. W.; Nellist, P. D.; Nicolosi, V., Two-dimensional nanosheets produced by liquid exfoliation of layered materials. *Science* **2011**, *331* (6017), 568-71.
155. Huo, C.; Yan, Z.; Song, X.; Zeng, H., 2D materials via liquid exfoliation: a review on fabrication and applications. *Science Bulletin* **2015**, *60* (23), 1994-2008.
156. Nicolosi, V.; Chhowalla, M.; Kanatzidis, M. G.; Strano, M. S.; Coleman, J. N., Liquid Exfoliation of Layered Materials. *Science* **2013**, *340* (6139).
157. Yang, D.; Sandoval, S. J.; Divigalpitiya, W. M.; Irwin, J. C.; Frindt, R. F., Structure of single-molecular-layer MoS₂. *Physical review. B, Condensed matter* **1991**, *43* (14), 12053-12056.
158. Li, H.; Wu, J.; Yin, Z.; Zhang, H., Preparation and applications of mechanically exfoliated single-layer and multilayer MoS₂ and WSe₂ nanosheets. *Accounts of chemical research* **2014**, *47* (4), 1067-75.
159. Yin, Z.; Li, H.; Li, H.; Jiang, L.; Shi, Y.; Sun, Y.; Lu, G.; Zhang, Q.; Chen, X.; Zhang, H., Single-layer MoS₂ phototransistors. *ACS Nano* **2012**, *6* (1), 74-80.
160. Chang, J.; Zhou, G.; Christensen, E. R.; Heideman, R.; Chen, J., Graphene-based sensors for detection of heavy metals in water: a review. *Analytical and bioanalytical chemistry* **2014**, *406* (16), 3957-75.
161. Chen, K.; Lu, G.; Chang, J.; Mao, S.; Yu, K.; Cui, S.; Chen, J., Hg(II) Ion Detection Using Thermally Reduced Graphene Oxide Decorated with Functionalized Gold Nanoparticles. *Anal. Chem.* **2012**, *84* (9), 4057-4062.
162. Mao, S.; Lu, G.; Chen, J., Nanocarbon-based gas sensors: progress and challenges. *J. Mater. Chem. A* **2014**, *2* (16), 5573-5579.
163. Frey, G. L.; Reynolds, K. J.; Friend, R. H.; Cohen, H.; Feldman, Y., Solution-processed anodes from layer-structure materials for high-efficiency polymer light-emitting diodes. *J. Am. Chem. Soc.* **2003**, *125* (19), 5998-6007.
164. Tan, C.; Zhang, H., Two-dimensional transition metal dichalcogenide nanosheet-based composites. *Chem. Soc. Rev.* **2015**, *44* (9), 2713-2731.
165. Rusu, P. C.; Brocks, G., Surface Dipoles and Work Functions of Alkylthiolates and Fluorinated Alkylthiolates on Au(111). *J. Phys. Chem. B* **2006**, *110* (45), 22628-22634.
166. Huang, C. C.; Chang, H. T., Selective Gold-nanoparticle-based "turn-on" Fluorescent Sensors for Detection of Mercury(II) in Aqueous Solution. *Anal Chem* **2006**, *78* (24), 8332-8338.
167. Zhang, Y.; Pluchery, O.; Caillard, L.; Lamic-Humblot, A.-F.; Casale, S.; Chabal, Y. J.; Salmeron, M., Sensing the Charge State of Single Gold Nanoparticles via Work Function Measurements. *Nano Lett.* **2015**, *15* (1), 51-55.
168. Choi, S.; Shaolin, Z.; Yang, W., Layer-number-dependent work function of MoS₂ nanoflakes. *Journal of the Korean Physical Society* **2014**, *64* (10), 1550-1555.
169. Li, M.; Zhou, X.; Guo, S.; Wu, N., Detection of lead (II) with a "turn-on" fluorescent biosensor based on energy transfer from CdSe/ZnS quantum dots to graphene oxide. *Biosens. Bioelectron.* **2013**, *43* (0), 69-74.

170. Karunasagar, D.; Arunachalam, J.; Gangadharan, S., Development of a 'collect and punch' cold vapour inductively coupled plasma mass spectrometric method for the direct determination of mercury at nanograms per litre levels. *J. Anal. At. Spectrom.* **1998**, *13* (7), 679-682.
171. Gong, J.; Zhou, T.; Song, D.; Zhang, L., Monodispersed Au nanoparticles decorated graphene as an enhanced sensing platform for ultrasensitive stripping voltammetric detection of mercury(II). *Sens. Actuators, B: Chem.* **2010**, *150* (2), 491-497.
172. Jiang, S.; Cheng, R.; Ng, R.; Huang, Y.; Duan, X., Highly sensitive detection of mercury(II) ions with few-layer molybdenum disulfide. *Nano Res.* **2015**, *8* (1), 257-262.
173. Mahajan, R. K.; Kaur, I.; Lobana, T. S., A mercury(II) ion-selective electrode based on neutral salicylaldehyde thiosemicarbazone. *Talanta* **2003**, *59* (1), 101-105.
174. Evans, O.; Mckee, G. D., Determination of Mercury(Ii) and Organomercury Compounds by Reversed-Phase Liquid-Chromatography with Reductive Electrochemical Detection. *The Analyst* **1988**, *113* (2), 243-246.
175. Wei, Y.; Gao, C.; Meng, F.-L.; Li, H.-H.; Wang, L.; Liu, J.-H.; Huang, X.-J., SnO₂/Reduced Graphene Oxide Nanocomposite for the Simultaneous Electrochemical Detection of Cadmium(II), Lead(II), Copper(II), and Mercury(II): An Interesting Favorable Mutual Interference. *The Journal of Physical Chemistry C* **2011**, *116* (1), 1034-1041.
176. Tielens, F.; Santos, E., AuS and SH Bond Formation/Breaking during the Formation of Alkanethiol SAMs on Au(111): A Theoretical Study. *J. Phys. Chem. C* **2010**, *114* (20), 9444-9452.
177. Knox, R.; Kammin, W. R.; Thomson, D., Atomic Fluorescence Determination of Mercury in Fresh-Water Ecosystems. *J Autom Chem* **1995**, *17* (2), 65-71.
178. Smedley, P. L.; Kinniburgh, D. G., A review of the source, behaviour and distribution of arsenic in natural waters. *Applied Geochemistry* **2002**, *17* (5), 517-568.
179. Darbha, G. K.; Singh, A. K.; Rai, U. S.; Yu, E.; Yu, H.; Chandra Ray, P., Selective Detection of Mercury (II) Ion Using Nonlinear Optical Properties of Gold Nanoparticles. *Journal of the American Chemical Society* **2008**, *130* (25), 8038-8043.
180. Laaksonen, P.; Kivioja, J.; Paananen, A.; Kainlauri, M.; Kontturi, K.; Ahopelto, J.; Linder, M. B., Selective Nanopatterning Using Citrate-Stabilized Au Nanoparticles and Cystein-Modified Amphiphilic Protein. *Langmuir* **2009**, *25* (9), 5185-5192.
181. Ghosh, P. S.; Kim, C.-K.; Han, G.; Forbes, N. S.; Rotello, V. M., Efficient Gene Delivery Vectors by Tuning the Surface Charge Density of Amino Acid-Functionalized Gold Nanoparticles. *ACS Nano* **2008**, *2* (11), 2213-2218.
182. Esplandiú, M. J.; Hagenström, H.; Kolb, D. M., Functionalized Self-Assembled Alkanethiol Monolayers on Au(111) Electrodes: 1. Surface Structure and Electrochemistry. *Langmuir* **2001**, *17* (3), 828-838.
183. Leung, T. Y. B.; Gerstenberg, M. C.; Lavrich, D. J.; Scoles, G.; Schreiber, F.; Poirier, G. E., 1,6-Hexanedithiol Monolayers on Au(111): A Multitechnique Structural Study. *Langmuir* **2000**, *16* (2), 549-561.
184. Hung, D. Q.; Nekrassova, O.; Compton, R. G., Analytical methods for inorganic arsenic in water: a review. *Talanta* **2004**, *64* (2), 269-277.
185. Forzani, E. S.; Foley, K.; Westerhoff, P.; Tao, N., Detection of arsenic in groundwater using a surface plasmon resonance sensor. *Sensors and Actuators B: Chemical* **2007**, *123* (1), 82-88.
186. Rey, N. A.; Howarth, O. W.; Pereira-Maia, E. C., Equilibrium characterization of the As(III)-cysteine and the As(III)-glutathione systems in aqueous solution. *Journal of Inorganic Biochemistry* **2004**, *98* (6), 1151-1159.
187. Kalluri, J. R.; Arbnesi, T.; Afrin Khan, S.; Neely, A.; Candice, P.; Varisli, B.; Washington, M.; McAfee, S.; Robinson, B.; Banerjee, S.; Singh, A. K.; Senapati, D.; Ray, P. C., Use of Gold Nanoparticles in a Simple

Colorimetric and Ultrasensitive Dynamic Light Scattering Assay: Selective Detection of Arsenic in Groundwater. *Angewandte Chemie International Edition* **2009**, *48* (51), 9668-9671.

188. Huang, Y.; Qiao, J.; He, K.; Bliznakov, S.; Sutter, E.; Chen, X.; Luo, D.; Meng, F.; Su, D.; Decker, J.; Ji, W.; Ruoff, R. S.; Sutter, P., Interaction of Black Phosphorus with Oxygen and Water. *Chemistry of Materials* **2016**, *28* (22), 8330-8339.

189. Krężel, A.; Leśniak, W.; Jeżowska-Bojczuk, M.; Młynarz, P.; Brasuń, J.; Kozłowski, H.; Bal, W., Coordination of heavy metals by dithiothreitol, a commonly used thiol group protectant. *Journal of Inorganic Biochemistry* **2001**, *84* (1), 77-88.

190. Delnomdedieu, M.; Basti, M. M.; Otvos, J. D.; Thomas, D. J., Reduction and binding of arsenate and dimethylarsinate by glutathione: a magnetic resonance study. *Chemico-Biological Interactions* **1994**, *90* (2), 139-155.

191. Moghimi, N.; Mohapatra, M.; Leung, K. T., Bimetallic nanoparticles for arsenic detection. *Anal Chem* **2015**, *87* (11), 5546-52.

192. Dai, X.; Nekrassova, O.; Hyde, M. E.; Compton, R. G., Anodic stripping voltammetry of arsenic(III) using gold nanoparticle-modified electrodes. *Anal Chem* **2004**, *76* (19), 5924-9.

193. Mulvihill, M.; Tao, A.; Benjauthrit, K.; Arnold, J.; Yang, P., Surface-enhanced Raman spectroscopy for trace arsenic detection in contaminated water. *Angewandte Chemie (International ed. in English)* **2008**, *47* (34), 6456-60.

194. Cui, R. Y. P. L. G. J. L. W. T., AN ULTRASENSITIVE MICRO ION SELECTIVE ARRAYS FOR MULTIPLEX HEAVY METAL IONS DETECTION *19 th International Conference on Miniaturized Systems for Chemistry and Life Sciences* **2015**, 1740-1742.

195. Komorowicz, I.; Barańkiewicz, D., Arsenic and its speciation in water samples by high performance liquid chromatography inductively coupled plasma mass spectrometry—Last decade review. *Talanta* **2011**, *84* (2), 247-261.

196. Ryder, C. R.; Wood, J. D.; Wells, S. A.; Yang, Y.; Jariwala, D.; Marks, T. J.; Schatz, G. C.; Hersam, M. C., Covalent functionalization and passivation of exfoliated black phosphorus via aryl diazonium chemistry. *Nat Chem* **2016**, *8* (6), 597-602.

197. Tipler, P. A. a. L., Ralph A., Modern Physics, 3rd Ed., W.H. Freeman. **1999**

198. Edmonds, M. T.; Tadich, A.; Carvalho, A.; Ziletti, A.; O'Donnell, K. M.; Koenig, S. P.; Coker, D. F.; Özyilmaz, B.; Neto, A. H. C.; Fuhrer, M. S., Creating a Stable Oxide at the Surface of Black Phosphorus. *ACS applied materials & interfaces* **2015**, *7* (27), 14557-14562.

199. Yoshida, Y.; Furuta, S.; Niki, E., Effects of metal chelating agents on the oxidation of lipids induced by copper and iron. *Biochimica et biophysica acta* **1993**, *1210* (1), 81-8.

200. Oviedo; Claudia; Rodr^guez; Jaime, EDTA: the chelating agent under environmental scrutiny. *Qu^{imica Nova}* **2003**.

201. Gómez-Navarro, C.; Weitz, R. T.; Bittner, A. M.; Scolari, M.; Mews, A.; Burghard, M.; Kern, K., Electronic Transport Properties of Individual Chemically Reduced Graphene Oxide Sheets. *Nano Letters* **2007**, *7* (11), 3499-3503.

202. Bao, W.; Cai, X.; Kim, D.; Sridhara, K.; Fuhrer, M. S., High mobility ambipolar MoS₂ field-effect transistors: Substrate and dielectric effects. *Appl. Phys. Lett.* **2013**, *102* (4), 042104

203. Kobayashi, T.; Kimura, N.; Chi, J.; Hirata, S.; Hobara, D., Channel-Length-Dependent Field-Effect Mobility and Carrier Concentration of Reduced Graphene Oxide Thin-Film Transistors. *Small (Weinheim an der Bergstrasse, Germany)* **2010**, *6* (11), 1210-1215.

204. Henke, C.; Steinem, C.; Janshoff, A.; Steffan, G.; Luftmann, H.; Sieber, M.; Galla, H.-J., Self-Assembled Monolayers of Monofunctionalized Cyclodextrins onto Gold: A Mass Spectrometric Characterization and Impedance Analysis of Host–Guest Interaction. *Anal Chem* **1996**, *68* (18), 3158-3165.
205. Camillone, N., Diffusion-Limited Thiol Adsorption on the Gold(111) Surface. *Langmuir* **2004**, *20* (4), 1199-1206.
206. Rouhana, L. L.; Moussallem, M. D.; Schlenoff, J. B., Adsorption of Short-Chain Thiols and Disulfides onto Gold under Defined Mass Transport Conditions: Coverage, Kinetics, and Mechanism. *Journal of the American Chemical Society* **2011**, *133* (40), 16080-16091.
207. Xue, Y.; Li, X.; Li, H.; Zhang, W., Quantifying thiol–gold interactions towards the efficient strength control. **2014**, *5*, 4348.
208. Hung, S.-W.; Kikugawa, G.; Shiomi, J., Mechanism of Temperature Dependent Thermal Transport across the Interface between Self-Assembled Monolayer and Water. *The Journal of Physical Chemistry C* **2016**, *120* (47), 26678-26685.
209. Martincova, J.; Otyepka, M.; Lazar, P., Is Single Layer MoS₂ Stable in the Air? *Chemistry (Weinheim an der Bergstrasse, Germany)* **2017**, *23* (53), 13233-13239.
210. Zhao, B.; Shang, C.; Qi, N.; Chen, Z. Y.; Chen, Z. Q., Stability of defects in monolayer MoS₂ and their interaction with O₂ molecule: A first-principles study. *Applied Surface Science* **2017**, *412* (Supplement C), 385-393.
211. Yue, W.; Bingchao, Y.; Bensong, W.; Xuekui, X.; Zhongming, Z.; Enke, L.; Guangheng, W.; Zhongyuan, L.; Wenhong, W., Degradation of black phosphorus: a real-time ³¹P NMR study. *2D Materials* **2016**, *3* (3), 035025.
212. Kim, J.-S.; Liu, Y.; Zhu, W.; Kim, S.; Wu, D.; Tao, L.; Dodabalapur, A.; Lai, K.; Akinwande, D., Toward air-stable multilayer phosphorene thin-films and transistors. *Scientific Reports* **2015**, *5*, 8989.
213. Illarionov, Y. Y.; Walzl, M.; Rzepa, G.; Kim, J.-S.; Kim, S.; Dodabalapur, A.; Akinwande, D.; Grasser, T., Long-Term Stability and Reliability of Black Phosphorus Field-Effect Transistors. *ACS Nano* **2016**, *10* (10), 9543-9549.
214. Qi, Y.; Xia, T.; Li, Y.; Duan, L.; Chen, W., Colloidal stability of reduced graphene oxide materials prepared using different reducing agents. *Environmental Science: Nano* **2016**, *3* (5), 1062-1071.
215. Chowdhury, I.; Mansukhani, N. D.; Guiney, L. M.; Hersam, M. C.; Bouchard, D., Aggregation and Stability of Reduced Graphene Oxide: Complex Roles of Divalent Cations, pH, and Natural Organic Matter. *Environmental science & technology* **2015**, *49* (18), 10886-10893.
216. Levita, G.; Restuccia, P.; Righi, M. C., Graphene and MoS₂ interacting with water: A comparison by ab initio calculations. *Carbon* **2016**, *107* (Supplement C), 878-884.
217. Nurdiwijayanto, L.; Ma, R.; Sakai, N.; Sasaki, T., Stability and Nature of Chemically Exfoliated MoS₂ in Aqueous Suspensions. *Inorganic Chemistry* **2017**, *56* (14), 7620-7623.
218. Linic, S.; Christopher, P.; Ingram, D. B., Plasmonic-metal nanostructures for efficient conversion of solar to chemical energy. *Nature Materials* **2011**, *10*, 911.
219. Cotton, F. A. W., Geoffrey *Advanced Inorganic Chemistry (5th ed.)*, New York: Wiley-Interscience: 1988; p 461.
220. https://en.wikipedia.org/wiki/Advanced_oxidation_process.
221. Zhang, H., Ultrathin Two-Dimensional Nanomaterials. *ACS Nano* **2015**, *9* (10), 9451-9469.
222. Sorgenfrei, S.; Chiu, C.-y.; Johnston, M.; Nuckolls, C.; Shepard, K. L., Debye Screening in Single-Molecule Carbon Nanotube Field-Effect Sensors. *Nano Letters* **2011**, *11* (9), 3739-3743.

223. Palazzo, G.; De Tullio, D.; Magliulo, M.; Mallardi, A.; Intranuovo, F.; Mulla, M. Y.; Favia, P.; Vikholm-Lundin, I.; Torsi, L., Detection Beyond Debye's Length with an Electrolyte-Gated Organic Field-Effect Transistor. *Advanced Materials* **2015**, *27* (5), 911-916.

CURRICULUM VITAE

Guihua Zhou

Place of birth: China

Education:

B.S., Xiangtan University, July 2012

Major: Engineering Mechanics

Ph.D., University of Wisconsin-Milwaukee (UWM), December 2017

Dissertation title: Real-time, Selective Detection of Heavy Metal Ions in Water Using 2D Nanomaterials-based Field-effect Transistors.

Research Experience:

- 2014-2017, “NSF PFI: AIR-RA: Enabling Low-cost, Real-time Monitoring of Heavy Metal Ions in Drinking Water”
- Summer 2015, NSF Innovation Corps Program

Presentations:

1. Poster presentation in 2015, MRS Fall Meeting & Exhibit, Boston, MA, USA
2. Oral presentation in 2016, Next Generation Water Technology, Milwaukee, WI, USA
3. Oral presentation in 2017, ACS Spring Meeting & Exhibit, San Francisco, CA, USA
4. Oral presentation in 2017, Navigating the Future of Water Conference, Milwaukee, WI, USA

Publications:

1. **Zhou, G.**; Pu, H.; Chang, J.; Sui, X.; Mao, S.; Chen, J., *Sensors and Actuators B Chemical* 2017, accepted.
2. Maity, A.; Sui, X.; Tarman, C.R. Pu, H.; Chang, J.; **Zhou, G.**; Ren, R.; Mao, S.; Chen, J., *ACS Sensors* 2017, accepted.
3. Chen, Y.; Ren, R.; Pu, H.; Guo, X.; Chang, J.; **Zhou, G.**; Chen, J., *Scientific Reports* 2017, 7(1), 10974.
4. Mao, S.; Pu, H.; Chang, J.; Sui, X.; **Zhou, G.**; Chen, J., *Environmental Science: Nano* 2017,4, 856-863.
5. **Zhou, G.**; Chang, J.; Pu, H.; Shi, K.; Mao, S.; Sui, X.; Ren, R.; Cui, S.; Chen, J., *ACS Sensors* 2016, 1 (3), pp 295–302
6. Mao, S.; Huang, X.; Chang, J.; Cui, S.; **Zhou, G.**; Chen, J., *NPG Asia Materials* 2015, 7, e224.

7. Mao, S.; Chang, J.; **Zhou, G.**; Chen, J., *Small* 2015, 11 (40), 5336-5359.
8. Cui, S.; Guo, X.; Ren, R.; **Zhou, G.**; Chen, J., *Journal of Physics D: Applied Physics* 2015, 48 (31), 314008.
9. Chang, J.; **Zhou, G.** (co- first author); Gao, X.; Mao, S.; Cui, S.; Ocola, L. E.; Yuan, C.; Chen, J., *Sensing and Bio-Sensing Research* 2015, 5, 97-104
10. Chang, J.; Huang, X.; **Zhou, G.**; Cui, S.; Mao, S.; Chen, J., *Nano Energy* 2015, 15, 679-687.
11. Huang, T.; Mao, S.; **Zhou, G.**; Zhang, Z.; Wen, Z.; Huang, X.; Ci, S.; Chen, J., *Nanoscale* 2015, 7 (4), 1301-1307.
12. Chang, J.; **Zhou, G.** (co- first author); Christensen, E. R.; Heideman, R.; Chen, J., *Analytical and Bioanalytical Chemistry* 2014, 406 (16), 3957-3975.
13. **Zhou, G.**; Chang, J.; Cui, S.; Pu, H.; Wen, Z.; Chen, J., *ACS Applied Materials & Interfaces* 2014, 6 (21), 19235-19241.
14. Huang, T.; Mao, S.; **Zhou, G.**; Wen, Z.; Huang, X.; Ci, S.; Chen, J., *Nanoscale* 2014, 6 (16), 9608-9613.
15. Hernandez, L. V.; Triadafilopoulos, G.; Chang, J.; **Zhou, G.**; Ganz, R. a.; Chen, J., *Gastrointestinal Endoscopy* 2014, 79 (5), AB513.
16. Chang, J.; Huang, X.; **Zhou, G.**; Cui, S.; Hallac, P. B.; Jiang, J.; Hurley, P. T.; Chen, J., *Advanced Materials* 2014, 26 (5), 665-665.
17. Chang, J.; Mao, S.; Zhang, Y.; Cui, S.; **Zhou, G.**; Wu, X.; Yang, C. H.; Chen, J., *Nanoscale* 2013, 5 (9), 3620-6.

Honors and Awards:

2016-2017, Distinguished Graduate Student Dissertation Fellowship, UWM

2012- 2017, Chancellor's Graduate Student Award/CEAS Dean's Scholarship (4 times)

2014, Graduate Student Award in Research Poster Competition of CEAS, UWM